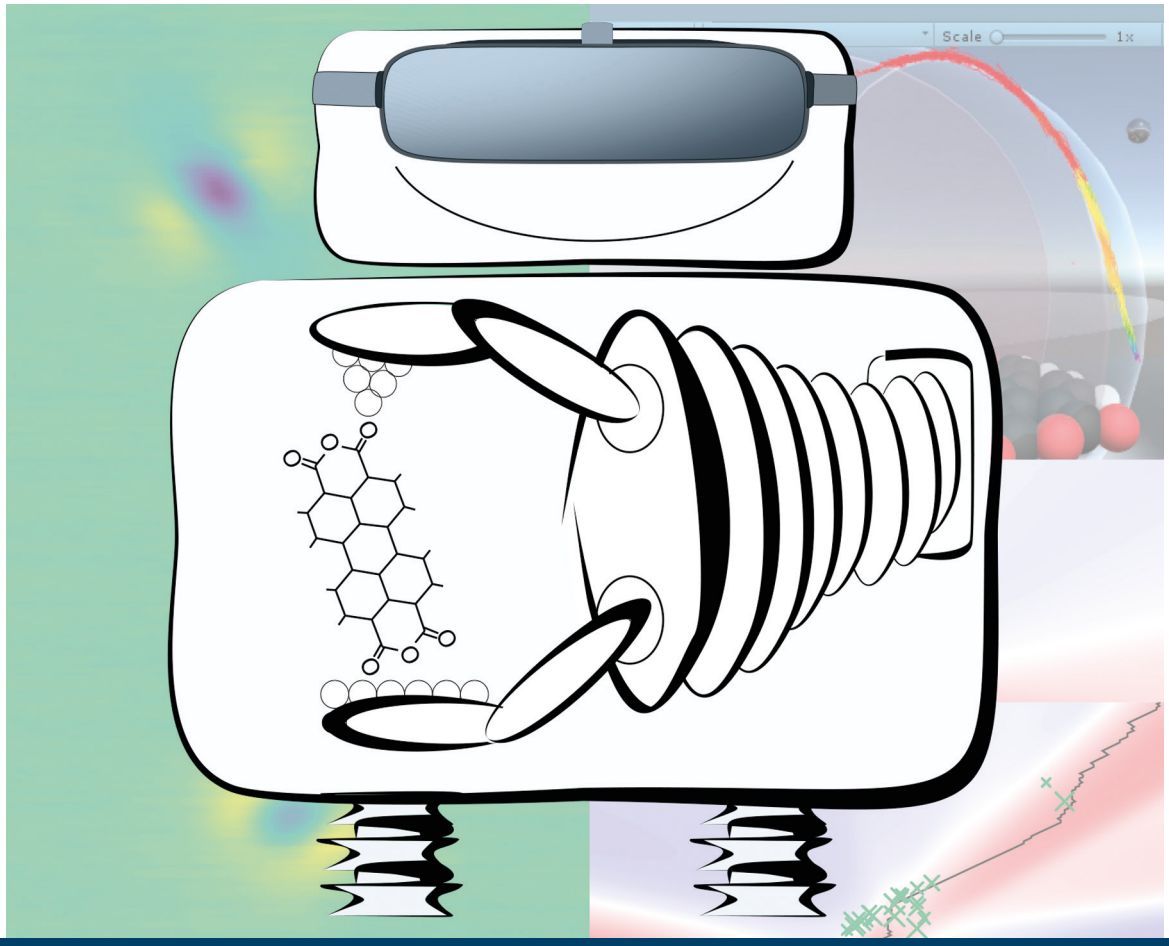

Controlled single-molecule manipulation

Philipp Kopp (geb. Leinen)

Information
Band / Volume 122
ISBN 978-3-95806-887-2

Mitglied der Helmholtz-Gemeinschaft

JÜLICH
Forschungszentrum

Schriften des Forschungszentrums Jülich
Reihe Information / Information Band / Volume 122

Forschungszentrum Jülich GmbH
Peter Grünberg Institut (PGI)
Quantum Nanoscience (PGI-3)

Controlled single-molecule manipulation

Philipp Kopp (geb. Leinen)

Schriften des Forschungszentrums Jülich
Reihe Information / Information Band / Volume 122

ISSN 1866-1777 ISBN 978-3-95806-887-2

Bibliografische Information der Deutschen Nationalbibliothek.
Die Deutsche Nationalbibliothek verzeichnet diese Publikation in der
Deutschen Nationalbibliografie; detaillierte Bibliografische Daten
sind im Internet über http://dnb.d-nb.de abrufbar.

Herausgeber und Vertrieb:	Forschungszentrum Jülich GmbH Zentralbibliothek, Verlag 52425 Jülich Tel.: +49 2461 61-5368 Fax: +49 2461 61-6103 zb-publikation@fz-juelich.de www.fz-juelich.de/zb
Umschlaggestaltung:	Grafische Medien, Forschungszentrum Jülich GmbH
Druck:	Grafische Medien, Forschungszentrum Jülich GmbH
Copyright:	Forschungszentrum Jülich 2026

Schriften des Forschungszentrums Jülich
Reihe Information / Information, Band / Volume 122

ISSN 1866-1777
ISBN 978-3-95806-887-2

Vollständig frei verfügbar über das Publikationsportal des Forschungszentrums Jülich (JuSER)
unter www.fz-juelich.de/zb/openaccess.

What I cannot create, I do not understand.
– Richard P. Feynman

This work is dedicated to my family.

Acknowledgement

Such a great project cannot be done by a one person alone - Thank you everyone who was involved or supported me in any way! My special thanks to

- **Prof. Dr. Frank Stefan Tautz** for the giving me the opportunity to perform my research at the PGI-3. It was inspiring to see his accumulated experience especially during paper discussions. I am also glad that I had the opportunity to get to know him in a more private environment at the IPAM conference compared to the normal work environment at the institute.
- **Prof. Dr. Ruslan Temirov** and **Dr. Christian Wagner** for introducing me to scientific work as my group leaders. They had the perfect synergy: Ruslan with his passion for clear experiments with clear results and Christian for his drive to dive deep into data analysis. I would especially like to thank Ruslan for his support already during my master thesis and for allowing me to work with your "old" baby (SPM), Christian for his tireless support during the writing phase of this thesis, and both of them for the long and fruitful discussions.
- **Dr. Matthew Green** and **Dr. Taner Esat** for teaching me the ins and outs of the SPM and for their companionship. Sometimes operating the SPM you feel like a better trained monkey. Having two or more monkeys in the lab makes it is directly much more pleasant. I enjoyed our fruitful scientific and non-scientific discussions or just hitting the ball around - including some wild rounds with potential damage to office equipment. I hope Taner keeps the anti-stress ball in honour.
- **Alexander Diener** for all his efforts on the CV (computational vision) program, which made the angle detection of the dropped molecules much easier. If there were any programming challenges to be solved he was the person to go to.
- **Aizhan Sabitova** for our collaboration in transferring the molecule lifting capabilities of the combined STM/AFM to an STM and for sharing her spectroscopy data around a molecular vacancy.
- **Rustem Bolat** for our joint efforts in the construction of single atom chains.
- Our collaborators who contributed significantly to the success of this thesis: **Prof. Dr. Klaus-Robert Müller**, **Dr. Kristof Schütt** and **Malte Esders** from the TU Berlin; **Prof. Dr. Rolf Findeisen** and **Dr. Michael Maiworm** from the OVGU Magdeburg.
- **Markus Franke**, **Dr. Sonja Schröder**, **Jana Wolters** and **Miriam Raths** for the cheerful atmosphere in the office and the "social gap" with Markus between our monitors.
- All the members of the PGI-3 for always being open to discussions on all subjects and to spend time at the "Workkaffee". It is thanks to all of you that I will have fond an vivid memories of my time at the institute.

- My family for the great support you have given me, not only during the time of my PhD, but throughout my life!
- Last but most important, my partner in life for her love, support and motivation.

Contents

CHAPTER 1

Introduction

Buzzwords like Industry 4.0, the Internet of things (IoT), augmented and virtual reality (AR and VR), cloud computing and artificial intelligence (AI) surround us every day. They are driven by our exponentially increasing ability to process vast amounts of digital data using integrated circuits (ICs). The transformative impact of these technologies on society is the result of low-cost mass production through miniaturisation. Miniaturisation makes it possible to produce smaller devices and reduce costs by fitting more ICs onto the same silicon wafer, thus making more efficient use of resources.

According to Moore's law [1, 2], the density of functional structures on a chip doubles every generation. As the functional structures on a chip get closer together, heat dissipation becomes an issue, putting additional focus on reducing power consumption. So today's ICs are fast, small, low cost and low power. Low power data processing opens up the application to mobile devices. The availability of low-cost processing power is enabling a horizontal disruption in technology in addition to the vertical evolution. With the arrival of smartphones in the consumer market sensors have also become cheap. In turn, the combination of low-cost sensors and local processing is economically interesting for other applications, especially robotics and automation. This demonstrates the critical importance of miniaturisation and mass production as technology drivers.

What is the ultimate scaling limit for building devices? What would be the applications if we could build functional structures from the bottom up with atomic precision, limited only by our imagination and physics (rather than technical limitations)? With current technology, this goal is still a long way off. However, we now have the unique opportunity to routinely probe and manipulate individual molecules and atoms, allowing us to characterise the properties of these fundamental building blocks. Our thirst to understand and predict their properties will lead to the discovery of new fundamental physical phenomena and improved theoretical and experimental methods.

The visionary concept of electronic circuits consisting of active components on the molecular scale was introduced by Aviram and Ratner in 1974. Their theoretical prediction that a single, polar molecule could act as a rectifier provided the basis for current work on molecular diodes [3]. However, experimental realisation of a single-molecule junction did not begin until the 1990s [4]. Reliable fabrication techniques on the scale of a few nanometres still

had to be developed. A prerequisite for any transport (e.g. charge, spin, thermoelectric) study is the interfacing of the target molecule with electrical contacts. The junction structure consists of three intertwined components: the electrodes, the contact interfaces, and the molecular backbone or functional centre [5]. Two important developments to electrically contact single molecules were: the mechanically controlled break junctions (MCBJ) and the scanning tunnelling microscope (STM). The STM was the first scanning probe microscope (SPM) and allowed the imaging *and* manipulation down to single atoms, the two key ingredients for studying molecular properties. The ability to see the fundamental building blocks of nature for the first time was the starting signal the nanoscience community had been waiting for. Experiments using STM or MCBJ were the first to report electronic charge transport through single molecules [4, 6].

Since then, the field of molecular electronics has matured. Many molecular equivalents of solid state devices have been discovered [7, 8], for example: molecular wires, molecular diodes, molecular capacitors, and molecular transistors. These impressive results demonstrated the feasibility of replacing solid-state functional structures with molecular structures in principle, bringing the dream of molecular-scale electronics closer. The real potential of molecular devices is, however, not in mimicking the properties of current solid-state technology. Excitingly, some of the intrinsic transport features found in molecular devices today are similar to concepts proposed for the next generation of solid-state technology to overcome the fundamental power dissipation limit of field-effect transistors. One such concept would be logic circuits based on electron spin. To this end, the first technological applications of molecules in ICs may be reported from molecular *spintronics*.

Despite all achievements in the field of molecular electronics, all measurements reported so far have been performed under laboratory conditions [5]. Practical applications are much more complex and subject to various sources of interference, such as ambient conditions and interface effects. Integrating single-molecule electronics into current solid-state technology remains a formidable challenge. Two major challenges to the mass production and the application of molecular junctions are device stability and device-to-device uniformity. Reliably connecting molecules to electrical contacts remains difficult; doing so reproducibly even more. In addition, theoretical models are needed that can fully explain the charge transport of molecular devices at a quantitative level. Bridging the gap between the continuous Fermi levels of the electrodes and the discrete energy levels of the molecules, as well as fully describing the vdW dispersion interactions, remain challenging. Faced with these challenges, basic research will play a crucial role in moving molecular electronics from nanoscience to nanotechnology. Further, quantitative characterisation experiments will provide important benchmarks for theoretical models.

In principle, bottom-up manufacturing allows control down to the single atom. There are two methods: either self-assembly or the active arrangement of molecular building blocks into a functional structure, building block by building block. Integrating self-assembly into conventional top-down manufacturing of solid-state technology is the most likely route to mass production of molecular devices. On the other hand, active assembly of functional molecular structures is more suitable for basic research and rapid prototyping. Furthermore, active assembly (also in combination with self-assembly) allows the fabrication of metastable

molecular structures that are not accessible by self-assembly or chemical synthesis alone. This adds a new set of tools for device fabrication. The development of a molecular manipulation platform that allows the routine automated construction of single-molecule compounds and the assembly of supramolecular structures would rapidly accelerate the characterisation of the vast space of molecular structures. At best, this search is guided by theory, as the estimated number of small organic molecular species is around 10^{60} [9].

The dream of a fully automated molecule manipulation laboratory (MoMaLab), from chemical synthesis of the molecule to fabrication and characterisation of the final device, can only be realised in steps. Before molecule manipulation can be fully automated, it is important to develop intuition for it, as well as an understanding of the underlying physics. Therefore, a first step towards a fully automated MoMaLab would be a platform that supports manual or semi-automated device construction for rapid prototyping by the experimenter with augmented feedback (e.g. visual or haptic). This thesis focuses on the development of such manipulation methods using the tip of an SPM as the end effector of a robotic nanomanipulator.

Robotic manufacturing has proven to be a successful solution in industrial automation. The introduction of robotic concepts for manual or (semi-)automated manipulation at the nanometre scale seems worth exploring. Robots interact with their environment via sensors and actuators, while offering more flexibility than single-purpose machines. The use of robotic manipulation in nanofabrication requires the application of the three robotic primitives, Sense, Plan, and Act, to the nanometre scale. The robot must be able to see/locate (Sense) the manipulation target in the working environment (e.g. the target molecule), and clearly identify successful establishment of a manipulation contact and achievement of the desired target state (e.g. the assembled nanostructure). Planning involves combining sensor information with the robot's "world knowledge" to identify actions that lead from the current state to the target (or terminal) state. The tasks are then translated into motor commands and sent to the actuators for physical implementation (Act).

There are a number of challenges in applying robotics at the nanoscale. In the macroscopic world, *simultaneous* monitoring of the manipulation progress while manipulating an object is easily solved by using cameras and image recognition techniques. Actions to achieve the target state can be calculated in a physically correct simulation of the environment or can be taught by a human teacher, for example by grabbing the end effector and moving it to the target position by hand. However, transferring these approaches directly to the nanoscale is impossible. The challenges involved are discussed below: To achieve the same visual control over the manipulation process on the molecular scale, atomically precise, time-resolved imaging *during* the manipulation process would be required. An SPM allows atomic resolution, but imaging and manipulation can only be executed *sequentially*. The tip apex of an SPM is atomically sharp. An image is created by scanning line by line over the substrate surface using the tip as a sensor, e.g. recording a height profile. During manipulation on the other hand, the tip has to move from one specific position to the next (for details see section 2.3). The manipulation-relevant physical properties of the end effector, the SPM tip, are also not fully known. While the apex atom can be characterised to some extent [10], the atomic structure in its vicinity, although relevant to the manipulation properties, cannot be

controlled. Furthermore, the SPM tip is essentially a rigid rod that lacks the fine mechanical capabilities of a macroscopic gripper. Quantitative quantum mechanical (QM) simulations are possible in principle, but their computational cost makes it impossible to use them as a controller for live manipulation. Human teaching of robots is also flawed because our intuition is based on the dominance of gravity, inertia, and friction, which only play a minor role at the molecular scale. The basic requirements for controlled robotic nanomanipulation via an SPM are: localisation of the target molecule, gripping - establishing of a mechanical connection, non-destructive movement of the molecule on the surface and (or) detachment from the surface, and non-destructive release of the molecule.

SPM combining both non-contact atomic force microscopy and tunnelling microscopy (nc-AFM/STM) is a particularly useful tool for robotic nanomanipulation because it simultaneously probes the forces and the charge transport currents during the manipulation [11]. It has been successfully used to study individual contributions to the molecule-surface binding energy [12, 13], the surface corrugation experienced by an isolated molecule [14], or the interaction between two isolated molecules [15].

For this thesis, the experiments were performed with the organic molecule PTCDA (perylene-3,4,9,10-tetracarboxylic dianhydride) on the Ag(111) surface at 5 K, using a nc-AFM/STM. PTCDA on Ag(111) meets the requirements for controlled robotic nanomanipulation and is therefore suitable for the development and analysis of new molecular manipulation protocols.

A distinct tip-molecule bond can be formed for PTCDA on Ag(111), by approaching one (of the four) carboxylic oxygen (O_{carb}) atoms of PTCDA with a Ag-terminated tip. The undercoordinated tip apex is more reactive than the closed Ag(111) surface. Therefore, the approached O_{carb} switches its bond to the surface to the tip, if the tip is close enough [16]. After tip-molecule bond formation, the molecule has bonds to both the tip and the substrate and thus is ready for two-contact manipulation (see section 3.2 for more details). Two-contact manipulation is used for all experiments presented in this thesis.

The prospects of basic, predefined manipulation trajectories are discussed in chapter 4 and utilized in a new characterisation method for the tip-molecule interactions. In section 4.2 vertical two-contact manipulation is used to study the contact formation of the SPM tip with the system, represented by a PTCDA/Ag(111) monolayer, and to probe the intermolecular interactions within the layer. In section 4.3 the tip-molecule bond is characterised by vertical two-contact manipulation of a PTCDA molecule attached to an artificial tip apex on the sample surface. Chapter 5 presents free manual molecular manipulation on complex three dimensional (3D) trajectories supported by immersive VR feedback for rapid prototyping and efficient establishment of new manipulation protocols. The focus will be on further refinement of the hand-controlled manipulation (HCM) method and its application to achieve controlled and reproducible charge transport measurements using the example of a Ag+PTCDA complex. Chapter 6 explores an alternative approach, realising *autonomous* manipulation on complex 3D trajectories by applying reinforcement learning (RL) to the mechanical control of the SPM tip. In chapter 7, robotic nanofabrication is applied to the construction of a molecular sensor and used to characterise the electrical potential of molecular vacancies in a closed PTCDA monolayer on Ag(111).

CHAPTER 2

Experimental methods

2.1 Scanning tunnelling microscopy and spectroscopy

The scanning tunnelling microscope (STM) was developed by Binning and Rohrer in 1981 [17, 18]. As well as imaging nanostructures with subangstrom precision, it can also manipulate single atoms [19, 20] and molecules [21] in a controlled manner. This versatility makes the STM the tool of choice for the construction and characterisation of novel nanostructures on a sample surface.

The key to its high resolution lies in the exponential dependence of the tunnelling current on the size of the gap between the atomically sharp metallic STM tip and a conducting sample. For each Å the tip approaches the surface, the tunnelling current increases by a factor 10.

The one-dimensional (1D) barrier model provides an intuitive understanding of the tunnelling process through a metal-vacuum-metal junction (Fig. 2.1). Quantum systems can be described by the Schrödinger equation and its time-independent version is

$$H\Psi = E\Psi, \tag{2.1}$$

where Ψ is the wave function of the quantum system, $H = -\frac{\hbar^2}{2m}\nabla^2_{\mathbf{r}} + V(\mathbf{r})$ is the Hamiltonian operator and E is the energy of the system. For the 1D barrier model the corresponding time-independent Schrödinger equation is

$$-\frac{\hbar^2}{2m}\frac{\partial^2}{\partial z^2}\Psi(z) + V(z)\Psi(z) = E\Psi(z). \tag{2.2}$$

The wave function $\Psi(z)$ can be split into solutions for region I, II, and III.

$$\begin{aligned} \text{region I}: &\quad \Psi_{\mathrm{I}} = Ae^{ikz} + Be^{-ikz} \\ \text{region II}: &\quad \Psi_{\mathrm{II}} = Ce^{\kappa z} + De^{-\kappa z} \\ \text{region III}: &\quad \Psi_{\mathrm{III}} = Fe^{ikz}, \end{aligned} \tag{2.3}$$

where $k = \sqrt{\frac{2m}{\hbar^2}E}$ and $\kappa = \sqrt{\frac{2m}{\hbar^2}(\Phi - E)}$ and Φ is the height of the barrier.

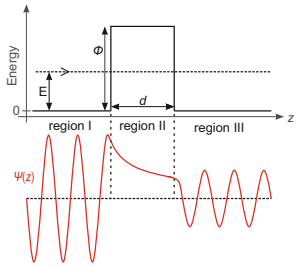

Figure 2.1: Tunnelling through a 1D barrier. The upper part shows a right travelling particle with energy E and the lower part shows its corresponding wave function. The wave function decreases exponentially with the effective barrier height $\Phi_{\text{eff}} = \Phi - E$ in the classical forbidden region.

The solutions for regions I and III show the form of oscillating waves for a free electron. The terms proportional to the coefficients A and F can be interpreted as right travelling waves, while the term proportional to B can be interpreted as reflections due to the barrier. The terms proportional to C and D describe evanescent waves. The amplitude A of the incoming wave belongs to a free electron, thus $A = 1$. The other coefficients can be determined by exploiting the continuous wave function and its derivative at the borders of the barrier.

The transmission coefficient T for long and heigh barriers, $\kappa d \gg 1$, is

$$T = |F^2| = \frac{16k^2\kappa^2}{(k^2+\kappa^2)^2} e^{-2\kappa d} \text{ [22]}. \tag{2.4}$$

Therefore, the transmission probability of an electron decreases exponentially with the width d and the square root of the effective height $\Phi_{\text{eff}} = \Phi - E$ of the tunnelling barrier. For metals in vacuum, Φ corresponds to the work function. The effective (rectangular) barrier height can be approximated by $\Phi_{\text{eff}} = \frac{\Phi_{tip}+\Phi_{sample}+eV_{\text{bias}}}{2} - E$ for two metals in close proximity and an applied bias voltage V_{bias}.

The measured tunnelling current by an STM is dependent on the rate of the electrons tunnelling through the vacuum gap between the tip and the sample. The tunnelling process depends on the time. Thus, it requires the time-dependent Schrödinger equation for its description

$$H\Psi(\mathbf{r},t) = i\hbar\nabla_t\Psi(\mathbf{r},t), \tag{2.5}$$

where $H = H_{\text{tip}} + H_{\text{sample}} + H_{\text{transfer}}$ is the full Hamiltonian of the system and $\Psi(\mathbf{r},t) = \Psi(\mathbf{r})\exp\left(\frac{-iEt}{\hbar}\right)$. H_{tip} and H_{sample} describe the separate parts of the tip and the sample respectively. H_{transfer} describes the coupling between the two parts and allows electrons to tunnel from the tip to the sample.

Fermi's golden rule gives the probability P for elastic tunnelling of an electron from the initial tip state $|\Psi_\mu\rangle$ to the final sample state $|\Psi_\nu\rangle$

$$T \sim P = \frac{2\pi}{\hbar}\sum_\nu |M|^2\,\delta(E_\nu - E_\mu), \tag{2.6}$$

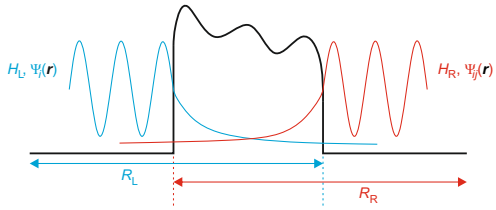

Figure 2.2: Separation of the tunnelling junction into the left $\mathbf{R_L}$ and right part $\mathbf{R_R}$, according to Bardeen.

with the matrix element $M = \langle \Psi_\nu | H' | \Psi_\mu \rangle$ and $H' = H_{\text{sample}} + H_{\text{transfer}} = H - H_{\text{tip}}$. Unfortunately, H' is unknown because neither H_{transfer} nor the full H are known.

Therefore, Bardeen [23] split the metal-vacuum-metal junction into two independent subsystems: $R_{\text{L}} = R_{\text{tip}} + R_{\text{barrier}}$ and $R_{\text{R}} = R_{\text{sample}} + R_{\text{barrier}}$ (Fig. 2.2). Ψ_μ (Ψ_ν) is basically zero to the right (left) side of the barrier. Thus, Ψ_μ (Ψ_ν) is a good solution for the region of the tip (sample) and the barrier, while it is a bad solution for the sample (tip) region. The linear combination of Ψ_μ and all final states Ψ_ν is a solution for the time-dependent Schrödinger equation

$$\Psi(\mathbf{r}, t) = a(t)\Psi_\mu(\mathbf{r}) \exp\left(-\frac{iE_\mu t}{\hbar}\right) + \sum_\nu b_\nu(t)\Psi_\nu(\mathbf{r}) \exp\left(-\frac{iE_\nu t}{\hbar}\right) \tag{2.7}$$

and H can be approximated by the model Hamiltonian H_{M}

$$H \sim H_{\text{M}} = \begin{cases} H_{\text{L}}, & \mathbf{r} \in R_{\text{L}} \\ H_{\text{R}}, & \mathbf{r} \in R_{\text{R}} \end{cases}. \tag{2.8}$$

H_{M} allows to greatly simplify $M = \langle \Psi_\nu | H' | \Psi_\mu \rangle$ of Fermi's golden rule. $H' = H - H_{\text{tip}}$ can be modified to $H' = H_{\text{M}} - H_{\text{L}}$. Thus, M becomes

$$M = \int_{-\infty}^{\infty} d\mathbf{r}\ \Psi_\nu^*(H_{\text{M}} - H_{\text{L}})\Psi_\mu = \int_{R_{\text{R}}} d\mathbf{r}\ \Psi_\nu^*(H_{\text{M}} - H_{\text{L}})\Psi_\mu. \tag{2.9}$$

The integration is reduced to R_{R}, because $H_{\text{M}} - H_{\text{L}} = H_{\text{L}} - H_{\text{L}} = 0$ in R_{L}. Similarly, $H_{\text{M}} - H_{\text{R}}$ evaluates to $H_{\text{R}} - H_{\text{R}} = 0$ in R_{R}. This can be used to symmetrize M, with

$$M = \int_{R_{\text{R}}} d\mathbf{r}\, (\ \Psi_\nu^*(H_{\text{M}} - H_{\text{L}})\Psi_\mu - \Psi_\mu(H_{\text{M}} - H_{\text{R}})\Psi_\nu^*)\,. \tag{2.10}$$

For elastic tunnelling, $E_\mu = E_\nu$, and by using $H_{\text{R}} = -\frac{\hbar^2}{2m}\nabla^2 + V_{\text{R}}(\mathbf{r})$ and Green's Theorem while integrating over an arbitrary surface S_{LR} inside the barrier region, M can be further simplified to Bardeen's matrix element

$$M_{\text{Bardeen}} = \frac{\hbar^2}{2m} \int_{S_{\text{LR}}} dS\ \ (\Psi_\mu \nabla \Psi_\nu^* - \Psi_\nu^* \nabla \Psi_\mu)\,. \tag{2.11}$$

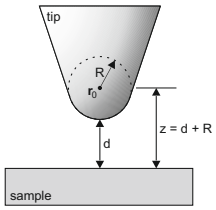

Figure 2.3: Schematic of the STM junction according to Tersoff and Hamann. The part of the tip closest to the surface is modelled as a spherical potential with it's origin at $\boldsymbol{r}_0$ and a curvature of R. is d is the smallest distance between the tip and the surface. Adapted from [24].

Then, in the limit of zero temperature and low V_{bias} the tunnelling current is given by

$$I = \frac{2\pi e}{\hbar} e V_{\text{bias}} \sum_{\mu,\nu} |M_{\mu\nu}|^2 \delta(E_\mu - E_{\text{F}}) \delta(E_\nu - E_{\text{F}}) \tag{2.12}$$

At zero temperature all states below the Fermi energy E_{F} are occupied while the states above E_{F} are unoccupied. E_μ and E_ν are the energies corresponding to Ψ_μ and Ψ_ν. The Dirac delta functions ensure that only states with the same energy (elastic tunnelling) contribute to the tunnelling current.

Explicit wave functions for the tip and surface must be inserted into eq. (2.11) to calculate Bardeen's matrix element. Therefore, Tersoff and Hamann [24] chose a plane wave Fourier expansion to describe the surface. A description for the tip is more difficult, because it's atomic structure is generally unknown. Starting with the simplest approximation for the tip, Tersoff and Hamann assumed the tip as a single point located at $\boldsymbol{r}_0$. They showed that the expression for the tunnelling current at low V_{bias} can then be simplified to

$$I \propto \frac{2\pi e}{\hbar} e V_{\text{bias}} \sum_{\nu} \left|\Psi_\nu(E_{\text{F}}, \boldsymbol{r}_0)\right|^2 \delta(E_\nu - E_{\text{F}}). \tag{2.13}$$

$|\Psi_\nu(\boldsymbol{r}_0)|^2$ is the probability of finding a surface state electron at the position of the tip. The sum corresponds to the local density of states (LDOS) of the sample at E_{F} and at $\boldsymbol{r}_0$, $\rho_{\text{sample}}(E_{\text{F}}, \boldsymbol{r}_0) = \sum_\nu \left|\Psi_\nu(E_{\text{F}}, \boldsymbol{r}_0)\right|^2 \delta(E_\nu - E_{\text{F}})$. The exponential dependence of I with distance can be recovered by considering the exponential decay of the surface state $\Psi_\nu \propto e^{-\kappa d}$ into the vacuum, where $\kappa = \sqrt{2m\Phi}/\hbar$. Thus, the LDOS of the sample becomes $\rho_{\text{sample}}(E_{\text{F}}, \boldsymbol{r}_0) \propto \rho_{\text{sample}}(E_{\text{F}}) e^{-2\kappa d}$. Summarising, the constant current STM images show the isosurface of the LDOS of the sample. They can be interpreted as topographic images if the LDOS is the same for structures on the surface, e.g. step edges on a single Ag crystal.

For a more realistic model of the STM tip Tersoff and Hamann considered a spherical tip as shown in Fig. 2.3. They showed that eq. (2.13) remains valid as long as the tip can be approximated by an s-like wave function. $\boldsymbol{r}_0$ becomes the origin of the s-wave and is therefore at the centre of the effective curvature R of the tip. This means that the LDOS is measured at $z = R + d$ above the surface and not at the minimal distance d between the tip and the surface.

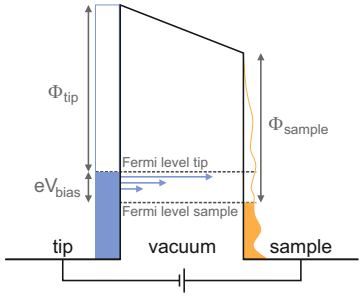

Figure 2.4: Energy diagram of the tunnelling process with a positive bias voltage V_{bias} applied to the sample. Electrons tunnel from occupied states of the tip to unoccupied states of the sample, as indicated by the blue arrows.

At finite V_{bias}, all tip states between the Fermi levels of the tip and the sample contribute to the tunnelling current to the sample (Fig. 2.4). A close inspection of the energy dependence in eq. (2.4) reveals that the effective barrier height is smaller for electrons closer to E_F. Thus, the tunnelling probability for electrons decreases exponentially with their energy difference to E_F. Therefore, the tunnelling current is still sensitive to the LDOS at finite V_{bias} and can be measured by scanning tunnelling spectroscopy (STS). This is done by sweeping V_{bias} and recording the differential conductance $dI/dV \propto \rho_{\text{sample}}(E_F, r_{\text{tip}})$.

2.2 Atomic force microscopy

The atomic force microscope (AFM) is a sibling of the STM [25]. It measures the forces between the probe (tip) and the sample surface instead of a tunnelling current. As no current measurement is required, AFM can also be applied to a wider range of samples, e.g. insulating or liquid-covered surfaces.

The most common method to achieve atomic resolution is frequency-modulated AFM (FM-AFM) [26]. It is a non-contact AFM (nc-AFM) method in which the tip is attached to a resonator. The resonator is actively driven at its resonance frequency f_0 while maintaining a constant vibration amplitude. Forces between the sample and the tip shift the resonance frequency. The measured frequency shift $\Delta f = f_0' - f_0$ between the current resonance frequency f_0' and f_0 is the FM-AFM signal. It can be used to regulate the distance of the tip to the sample.

The experiments in this thesis are performed with a qPlus sensor [27]. The first generation of qPlus sensors was build similarly to a quartz tuning fork found in wristwatches, except that one prong was passivated by firmly attaching it to a heavy mass. The tip was attached to the other, active prong. The high stiffness of the qPlus sensor allows for subangstrom oscillation amplitudes, and it prevents snapping into contact when performing AFM mea-

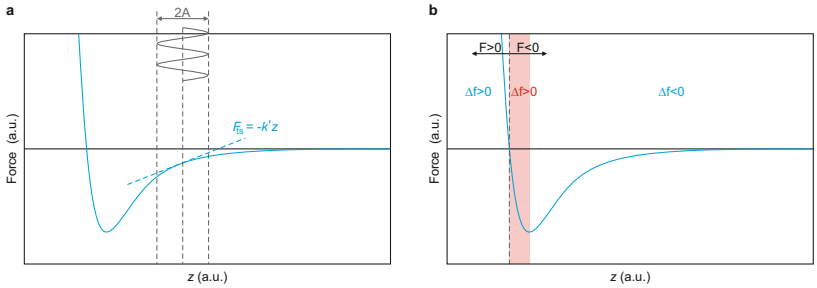

Figure 2.5: Lennard-Jones like force as an example for the tip-sample force. **a**, For small amplitudes, the tip-sample force is approximated to be proportional to k' in the range of the oscillation. Here, the slope is positive and thus $k' < 0$. **b**, The signs of force and frequency shift are the same for most parts of the z range. In these parts, a positive frequency shift corresponds to a repulsive force and a negative one to an attractive force. Only in the area highlighted in red have they opposite signs.

surements in close proximity to the sample surface. The small oscillation amplitude enables the simultaneous measurement of an STM and AFM signal.

To better understand the Δf signal, let us look at the model of an actively driven harmonic oscillator with damping [22]. Its equation of motion is

$$m\ddot{z} = m\gamma\dot{z} - k(z - z_{\text{drive}}). \tag{2.14}$$

With the resonance frequency $\omega_0 = \sqrt{\frac{k}{m}}$ and the quality factor $Q = \frac{\omega_0}{\gamma}$ this equation reads as

$$\ddot{z} + \omega_0 \frac{1}{Q}\dot{z} + \omega_0^2(z - z_{\text{drive}}) = 0 \tag{2.15}$$

In the limit of a small oscillation amplitude A, it is assumed that a time-independent tip-sample force F_{ts} varies only slowly in the range of oscillation. Thus F_{ts} can be approximated as linear in z and its interaction with the tip can be modelled as a spring with spring constant $k' = -\frac{\partial F_{\text{ts}}}{\partial z}$ (Fig. 2.5a). Both springs can be combined into one effective spring constant $k_{\text{eff}} = k + k'$

The resonance frequency ω_0 will shift to ω_0' in the presence of tip-sample forces.

$$\omega_0' = \sqrt{\frac{k_{\text{eff}}}{m}} = \omega_0\sqrt{1 + \frac{k'}{k}} \approx \omega_0\left(1 + \frac{k'}{2k}\right), \tag{2.16}$$

with k being replaced by the effective spring constant k_{eff} to include the tip-sample force. The approximation assumes $\left|k' \ll k\right|$, and $\sqrt{1+x} \approx 1 + \frac{1}{2}x$ for small x.

The experimentally observed frequency shift Δf becomes

$$\Delta f = \frac{\omega_0' - \omega_0}{2\pi} = f_0\frac{k'}{2k} = -\frac{f_0}{2k}\frac{\partial F_{ts}}{\partial z}. \tag{2.17}$$

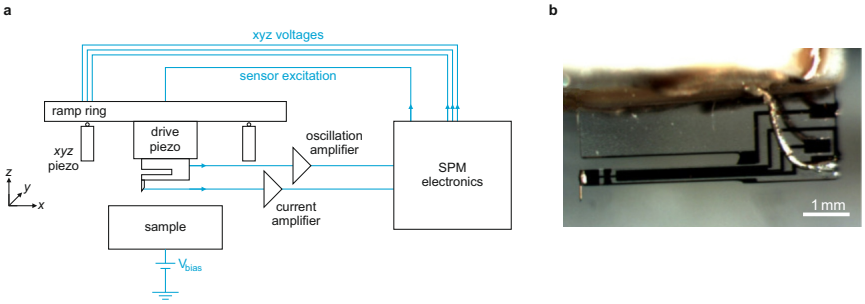

Figure 2.6: Schematic of the SPM setup and picture of a qPlus sensor. **a**, Schematic. The qPlus sensor is attached to a ramp ring. The ramp ring rest on three piezo tubes (two are shown). The piezos bend in the x, y direction and stretch in the z direction if the corresponding voltages are applied. A drive piezo allows the excitation of the qPlus sensor. **b**, Picture of a qPlus sensor with attached tip, available from Createc™.

In the limit of small amplitudes, the frequency shift is proportional to the negative force gradient. This assumption is reasonable for the subangstrom oscillation amplitude of a qPlus sensor.

With $F_{\mathrm{ts}} = -k^{'}z$, the slope is positive if F_{ts} becomes more attractive (Fig. 2.5a). Thus $-k^{'} < 0$ and the measured frequency shift is negative. Therefore, a negative (positive) frequency shift indicates that F_{ts} becomes more attractive (repulsive) on further approach towards the surface.

In case of a Lennard-Jones like force, one can simplify the interpretation for positive / negative frequency shift. For most parts of the z range, a negative frequency shift corresponds to an attractive force and a positive frequency shift to a repulsive force. Only in a small z range, marked in red in Fig. 2.5b, is this interpretation wrong. The above interpretation is oversimplified for more complex forces, e.g. the $\Delta f(z)$ during molecule manipulation!

2.3 Experimental setup

The SPM is a commercial, beetle-type nc-AFM/STM equipped with a third generation qPlus sensor [27] from Createc™. Fig. 2.6a shows a schematic of the setup. The qPlus sensor (Fig. 2.6b) has a stiffness of 1800 N/m, a resonance frequency of 31 078 Hz and a quality factor between 50 k - 70 k at operational conditions (around 5 K and 10^{-10} mbar). The amplitude of the qPlus oscillation used in the experiments was 0.2 Å. The small oscillation amplitude makes it possible to record the STM and AFM signals simultaneously. Small amplitudes are also important when characterising the mechanical properties of molecules with controlled manipulations. The experiments were performed at 5 K and at a base pressure of $5 \cdot 10^{-11}$ mbar.

Principles of SPM operation

Scan mode: feedback on

The height of the SPM tip above the surface is regulated by a control loop using either the tunnelling current or the frequency shift as a feedback signal. The controller increases or decreases the height to keep the feedback signal at a constant value. These variations in height are the recorded data. A line scan across a single crystal in this mode corresponds to a height profile of the crystal surface. A topography image of an area is generated by scanning multiple lines in succession.

Only the tunnelling current was used for height control in this thesis and the recordings are referred to as STM topography images.

Scan mode: feedback off

In this mode, the height control is switched off (also called: feedback off). The varying current and frequency shift, due to changes in the surface topography, are recorded during a scan. Without feedback, there is a high risk to crash the SPM tip while scanning. Therefore, this mode is mainly used on atomically flat surfaces.

Lateral manipulation

The SPM software provides simple forms of manipulation protocols. Lateral manipulation (LM) allows for example to push adatoms around on the substrate surfaces. The operator selects a line in a previously recorded image to serve as the tip trajectory for LM. The software positions the tip with feedback on at the start point, approaches closer to the surface (a different setpoint for the feedback loop) and moves the tip in a line to the end point, where the original setpoint is restored.

Vertical manipulation and spectroscopy

The other simple manipulation protocol provided by the software is vertical manipulation (VM). The SPM tip is moved perpendicular to the surface along the z axis during VM. The operator selects a point in a previously recorded image to execute a VM. The software positions the tip with feedback on at the specified point, turns the feedback off and the executes the predefined VM. The z ramp and V_{bias} ramp of the VM can be specified among other parameters (Fig. 2.7). The software turns the feedback on again after the VM and moves the tip back to its original position. The VM provided by the software can also be used to record spectroscopy data (e.g. V_{bias} ramp at constant height).

Extended setup

Unfortunately, the SPM software does not provide a reliable solution to record spectra or scans at different z heights over a long period of time. Therefore, the SPM setup is extended by a remote controlled voltage source (RVS) with additional rotary knobs on each channel for the manual adjustment of the output voltage.

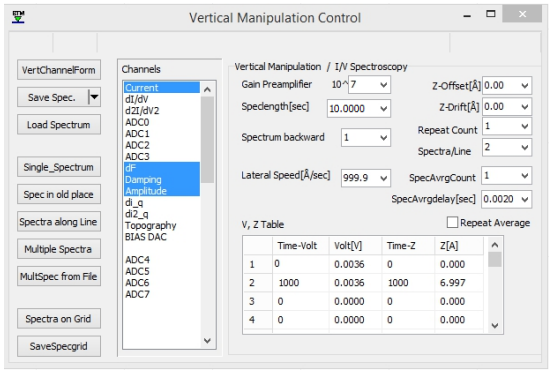

Figure 2.7: Screenshot of the VM control window of the SPM software (Createc™). The specified parameters are typical for testing the contacting behaviour of the tip with a molecule within a PTCDA monolayer on Ag(111), while recording the STM and AFM signals. The specified bias voltage is $V_{\text{bias}} \approx 1\,\text{mV}$, after accounting for the offset. The analogue digital converter inputs ADC0 to ADC7 can be used to record signals from additional hardware like the $\frac{dI}{dV}$ signal from a lock-in amplifier.

The RVS voltages (x', y', z') are added to the x, y, z voltages by connecting the RVS channels to the corresponding modulation inputs of the SPM electronics (Fig. 2.8). On the one hand, this allows to position the tip as usual with the SPM software. On the other hand, the tip position can be offset by the RVS voltages.

The operator can now manually adjust the tip position in the z direction by turning the corresponding knob, after the feedback has been switched off. Images and spectra can then be recorded as usual.

The rotary knobs can also be used to perform basic manual molecule manipulations. Complex manipulations are performed using a custom script via the remote interface of the RVS. The experimental signals are digitalised by a ADC unit to record them during a molecule manipulation. Fig. 2.8 shows a schematic of the complete SPM setup.

Tip and sample preparation

The SPM tip is a 25 µm thin PtIr wire sharpened with diagonal cuts of a focused ion beam. An atomically sharp Ag-terminated tip was obtained by repeated cycles of dipping the tip into the clean Ag(111) sample surface and checking the tip quality. The latter was controlled by imaging and spectroscopy of PTCDA/Ag(111).

The Ag(111) single crystal was prepared by repeated cleaning cycles of Ar^+ sputtering (0.8 keV, 15 min) and annealing (530 °C, 15 min). A coverage of $\sim 10\,\%$ of a monolayer of PTCDA was deposited from a custom-built Knudsen-cell onto the crystal, which was kept at room temperature. The evaporation temperature for PTCDA was 300 °C. After the deposition, the surface was briefly annealed to 200 °C.

Some experiments required the presence of additional Ag adatoms on the sample surface. The custom Ag evaporator consisted of two main components: (1) a thick W wire for direct

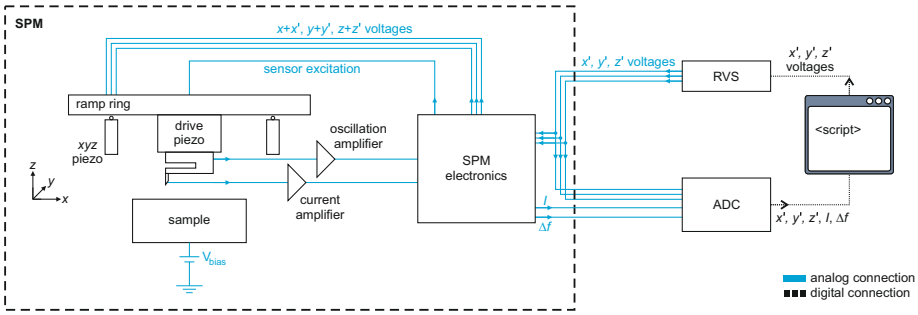

Figure 2.8: Schematic of the extended SPM setup.

heating with an electric current, (2) a thin Ag wire that was repeatedly wrapped around the W wire. The thermal conductivity was sufficient to evaporate Ag atoms without the need to melt the Ag wire into a drop. The Ag evaporator allowed the in situ deposition of Ag adatoms onto the sample surface. A coverage of a 1 % - 2 % percent of adatoms was reached within a few seconds of deposition.

CHAPTER 3

Manipulation methods

3.1 Conventional manipulation

3.1.1 Introduction

One of the most interesting applications of the SPM is the manipulation of single atoms and molecules. Due to the compact nature of atoms and small molecules (e.g. CO), the centre of mass becomes their only relevant descriptor. They can be manipulated by a combination of pulling, pushing, or a pickup-transfer-drop sequence. These manipulations are abrupt and stochastic in nature.

Moving the adsorbates over the sample surface often involves the direct force interactions between the adsorbate and the SPM tip, as well as the electric field in the tunnelling gap. The adsorbate-substrate interaction plays an important role for the success rate of the manipulation process. Therefore, low-index metal surfaces are well suited for building nanostructures by lateral manipulation (LM).

3.1.2 Manipulation protocol: Moving Ag adatoms on Ag(111) via lateral manipulation

Ag adatoms are deposited on PTCDA/Ag(111) according to section 2.3. They sit in hollow sites on the Ag(111) surface. At LHe temperature, the adatoms will not move between hollow sites, unless triggered by an external force - such as the SPM tip. To move a Ag adatom on Ag(111), the tip is equilibrated over the clean surface (setpoint: 0.1 V, 2000 nA) and moved in a line over the target atom with active feedback. The end of the line should be the desired location (or in its vicinity).

The adatoms can be arranged in clusters or moved closer to an isolated PTCDA molecule to from a Ag+PTCDA complex. Section 4.3 reports the characterization of such a complex.

3.2 Two-contact manipulation

3.2.1 Introduction

The SPM tip has to first form a contact with a molecule adsorbed on the surface in order to manipulate it. The undercoordination of the tip apex atom makes it more reactive than the bulk atoms of the same metal and facilitates the formation of a chemical tip-molecule bond. Note that the reactivity of the apex atom depends on the structure of the apex. Any change in the structure can therefore affect the strength of the tip-molecule bond.

Larger molecules with reactive groups as specific binding sites (a chemical 'handle' or an 'anchor') offer the possibility of binding to the SPM tip and the substrate surface simultaneously and at well-known locations. By using both the SPM tip and the substrate surface as 'robotic fingers', two-contact manipulation allows a high degree of control up to internal degrees of freedom of the manipulated molecules [28].

The control of the two-contact manipulation benefits the assembly of molecular structures and the characterisation of charge transport. Therefore, it will be used throughout this thesis, unless otherwise stated.

In *basic* two-contact manipulation, the SPM tip pulls the molecule along a 1D trajectory through the tip-molecule bond. Vertical two-contact manipulation is discussed below as an example.

To characterise the charge transport in a similar way to MCBJ experiments, an isolated molecule on the surface is lifted by VM until the molecule has only a single bond remaining to the surface and is vertically aligned in the junction. However, unlike a MCBJ, this junction structure can be precisely controlled: First, the area for the experiment can be inspected by imaging. Second, the interfaces between the molecule and the electrodes (tip and surface) are defined by single bonds to functional groups of the molecule. Third, the vertical alignment can be tuned by controlling the junction according to the mechanical response of the molecule in the Δf signal. Additionally, the entire controlled cleavage process of the molecule from the surface is available to study the interplay between the mechanical and charge transport properties of the molecule. Fourth, the effect of the environment (e.g. of surrounding atoms or molecules) around the surface-molecule bond on charge transport can also be studied.

The full potential of two-contact manipulation unfolds with free 3D tip movement. Moving the tip along *complex* trajectories relative to the surface anchor allows access to intramolecular degrees of freedom and, in principle, the selection of specific configurations. This could be applied to characterise charge transport of specific configurations, to realise a specific functionality, or to reach metastable states not accessible by self-assembly (e.g. for device fabrication). Assembled metastable configurations are discussed in section 3.2.4.

However, manipulation on free 3D trajectories comes with its own set of difficulties. There are two main challenges to overcome: The first is control. How can the experimenter intuitively execute 3D tip movements? The second is our lack of intuition for the mechanics on the scale of a few nanometres. A solution to these challenges will be discussed in section 3.3.

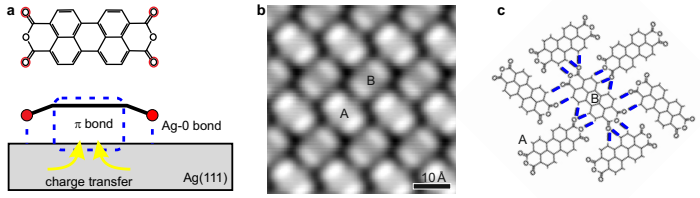

Figure 3.1: Interactions and structural properties of PTCDA/Ag(111). **a**, Structural formula and sketch of PTCDA bonding to Ag(111); adapted from [29]. **b**, Former LUMO contrast topography image of PTCDA/Ag(111), setpoint: $-0.35\,\mathrm{V}, 0.2\,\mathrm{nA}$. **c**, Sketch of the H-bonds between PTCDA molecules. The orientation of the molecules in b and c is the same.

3.2.2 Prerequisites

A molecule suitable for two-contact manipulation must meet the following requirements: First, the interactions between the target molecule and the substrate surface must be strong enough to immobilise an isolated molecule on the surface that it can be imaged by an SPM. Second, the molecule needs a 'handle' that allows it to form a reversible mechanical bond with the SPM tip, for example through a functional group. Third, the interactions between the molecule and the substrate surface must not be too strong, otherwise manipulation will be impossible.

The organic semiconductor PTCDA, with a reactive carbonyl group at its four corners, fulfils the above requirements for two-contact manipulation on a gold or silver substrate. This thesis focuses on two-contact manipulation of PTCDA on Ag(111), and its main structural and electronic properties are briefly presented here.

Fig. 3.1a,b shows the chemical structure of the molecule with a reactive carbonyl group at its four corners (marked in red) and an STM topography image of PTCDA/Ag(111). The size of the molecule is $11.4\,\text{Å} \times 6.8\,\text{Å}$ (distance along O-O on the long side and H-H on the short side) [30]. PTCDA forms a commensurate herringbone superstructure on Ag(111). The unit cell ($b_1 = 18.96\,\text{Å}$, $b_2 = 12.61\,\text{Å}$, $\gamma = 89°$ [31]) contains two inequivalent molecules, which will be referred to as aligned (A) and misaligned (B) with respect to the underlying Ag(111) lattice [30].

The structural and electronic properties of the PTCDA/Ag(111) interface are determined by a complex interplay of intermolecular and molecule-surface interactions.

A single PTCDA binds to Ag(111) via a complex chemisorptive interaction (Fig. 3.1a). First, this involves local bonds between carboxylic oxygen (O_{carb}) atoms and the silver surface, and second, a hybridization of its π-orbitals with metal states leading to charge transfer into the former lowest unoccupied molecular orbital (LUMO) of PTCDA [32]. The presence of two distinct bonding functions in the PTCDA/Ag(111) bond is manifested in the clearly observable distortion of the molecular structure, with its four O_{carb} atoms bent down towards the surface [33]. This distortion appears as the molecule balances out the repulsion of its π-conjugated core by the attraction of the four Ag-O bonds.

For molecules inside a closed monolayer, the intermolecular interactions between PTCDA molecules, governed by H-bonds (Fig. 3.1c), reduce the charge transfer, increase adsorption height, and reduce the distortion of PTCDA [34]. This can be investigated by molecular manipulation (see section 4.2).

Type A molecules appear brighter than type B molecules in Fig. 3.1b. Their different electronic structure is a result of their unequal adsorption sites. The former LUMO of type B molecules is shifted 160 mV lower than for type A. The centre between the two broad LUMO resonances lies around ≈ -0.3 eV with both resonances crossing the Fermi level [35].

3.2.3 Basic implementation of two-contact manipulation

This section gives a brief overview of two basic manipulation methods for two-contact manipulation and then introduces some manipulation protocols.

Vertical manipulation (VM) of single molecules is the simplest form of two-contact manipulation. The molecule to be manipulated can be isolated on the sample surface or be part of a molecular layer. The SPM tip is positioned over a reactive group of the molecule. Then the tip descends on a vertical trajectory towards the surface to contact the molecule and retracts again on a vertical trajectory for manipulation. VM is used to characterise the electrical and mechanical properties of single molecules and to construct an SQDM sensor (see section 3.2.4 for the latter).

Fig. 3.2 shows the typical experimental signals during a VM of PTCDA on Ag(111). A sudden increase (decrease) in I or a kink in Δf are the characteristic features of a chemical Ag-O bond formation (rupture). Fig. 3.2a shows contact formation and rupture of the tip-molecule bond. This is typical for a VM of a molecule inside a monolayer of PTCDA. If the molecule is isolated on the sample surface, it can be fully detached by a VM (Fig. 3.2b). The molecule has been successfully detached from the surface and remains vertical on the tip, if the characteristic peak-dip feature with a smooth transition to zero tip-surface interaction is observed in the Δf signal (Fig. 3.2b).

A VM can be executed by using the SPM software. However, the position of the tip after the VM will be fixed to the position at the start of the VM. This is not always desirable.

Using three rotary knobs for xyz positioning of the SPM tip gives more control during manipulations. The z knob can be used for VM. In addition, less complex 3D manipulations can be performed efficiently using the knobs. Before the voltages from the SPM electronics are applied to the tip's piezo actuators, the xyz output voltages from the RVS are added to their respective channels (see section 2.3). The RVS allows direct control of its output voltages, and thus the tip position, via rotary knobs. The remote control of the RVS is used for HCM (see sections 3.3 and 5.2) or autonomous manipulation (see chapter 6).

Two-contact manipulation protocols for PTCDA on Ag(111) with rotary knobs are presented below. Prior to manipulation, the location and orientation of the molecule to be manipulated are determined by recording an STM topography image of the respective area. The SPM tip is then positioned over one of the O_{carb} atoms of the molecule. The feedback is turned off and all subsequent manipulations are performed using the rotary knobs.

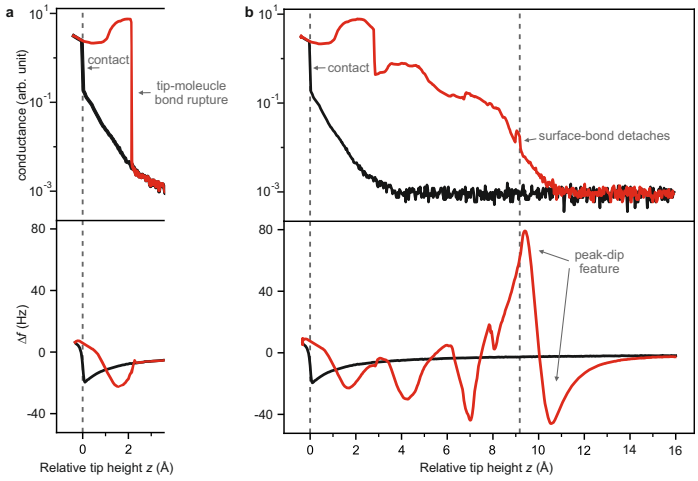

Figure 3.2: Vertical manipulation of PTCDA on Ag(111) - experimental signals. The tip approaches the surface (black curves) and retraces from the surface (red curves) on a vertical trajectory. The dashed lines indicate the height of contact formation and the height, where the last O_{carb} of PTCDA detaches from the surface. **a**, Manipulation signals for a molecule inside a molecular layer. **b**, Manipulation signals for an isolated molecule on Ag(111).

Isolating a single PTCDA molecule

After the sample preparation (see section 2.3), the PTCDA molecules are found in closed islands on the Ag(111) surface. To characterise a single molecule, or to use it as a building block for a metastable structure, a single molecule has to be separated from the island.

To obtain a single, isolated PTCDA, it is easier to separate a molecule from the edge of an island than to lift it from a closed layer. At the edge, the target molecule for manipulation has fewer surrounding molecules and therefore intermolecular interactions are weaker compared to the layer.

To begin the manipulation, the SPM tip is positioned over a O_{carb} of a PTCDA on the edge of the island, with its O_{carb} facing the clean Ag(111) surface (and not other molecules). To contact the molecule, the tip is approached towards the surface, while monitoring I and Δf on the oscilloscope, until the tip-molecule bond formation is observed.

To separate the molecule from the island, a peeling motion is initiated similar to the averaged reference trajectory for the molecule within a layer (e.g. Fig. 3.4). Here, the forces acting on the tip-molecule bond are weaker and a simplified version is sufficient (by alternating control between xz and yz channels). Often it is sufficient to stop peeling after observing sharp discontinuities in the I or Δf signal, indicating H-bond ruptures. Then, the tip is moved laterally (only xy) away from the island (e.g. 10 Å), while monitoring on the oscilloscope that the molecule is indeed being dragged along.

Once the molecule is isolated on the Ag(111) surface, the tip is retracted from the surface

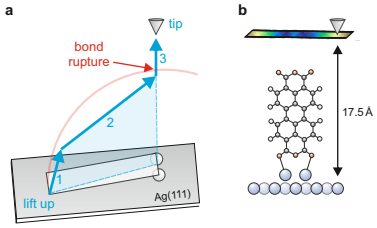

Figure 3.3: Manipulation protocol for erecting a 2Ag+PTCDA complex and its final structure. **a**, Schematic of the manipulation protocol. The three blue arrows indicate the manipulation trajectory for erecting PTCDA on two adsorbed Ag adatoms. The trajectory begins above one of the two unpaired O_{carb} (point of bond formation) and ends above the centre between the two Ag adatoms (after bond rupture). **b**, Schematic side view of a standing PTCDA molecule. The bar shows a recorded Δf-image at 17.5 Å above the Ag(111) surface, colour code from blue (negative) to brown (positive); adapted from [36]. For more information see text.

to detach the molecule from the substrate. When the peak-dip feature is observed, the molecule is hanging from the tip and can be reversibly deposited at any location on the clean Ag(111) surface. If the tip-molecule bond ruptures prematurely or the molecule flips to the tip, start again with a clean tip.

For the deposition, the Δf signal is monitored as the tip descends onto a clean Ag(111) surface area. The approach is stopped around $\Delta f = 0\,\text{Hz}$ after observing the dip from the peak-dip feature. This is where the attraction between the molecule and the surface is strongest. Now the bias voltage is increased up to 0.5 V - 0.6 V. If this is not enough to break the tip-molecule bond, the tip is moved gently closer to or further away from the surface (1 Å - 2 Å should be sufficient).

This method allows a hanging PTCDA to be reversibly deposited back onto the Ag(111) surface. Often, the molecule and the tip apex are intact after deposition.

Erecting a 2Ag+PTCDA complex on Ag(111)

The assembly of 2Ag+PTCDA is detailed in section 4.3.2, which describes the process of dragging a PTCDA molecule across two Ag adatoms.

Erecting an assembled 2Ag+PTCDA on Ag(111) into a standing configuration (so called s-PTCDA) is surprisingly simple. In principle, a circular manipulation trajectory would be ideal and HCM can be used to achieve this [36]. Due to the flexibility of PTCDA molecules (especially the O_{carb} bonds), it is sufficient to approximate a circular trajectory with a few straight lines. These can be executed with the rotary knobs of the RVS.

To begin the manipulation, the tip is positioned over one (of the two) unpaired O_{carb} of the complex. The tip then descends towards the surface to contact the complex. After contact formation, the PTCDA molecule is erected by moving the tip along a path similar to the trajectory sketched in Fig. 3.3a. The trajectory is divided into three straight lines (blue arrows): The first two lines follow a simplified sphere like shape (with a radius equal to the length of the long axis of 2Ag+PTCDA) and end above the centre between the two

Ag adatoms of the complex. Following the third line, the tip is retracted vertically from the surface to break the tip-molecule bond, leaving the 2Ag+PTCDA complex in a free standing, vertical configuration. The standing configuration is confirmed by recording a constant height Δf-image similar to Fig. 3.3b.

3.2.4 Metastable configurations achievable by two-contact manipulation

s-PTCDA on the surface - A free-standing molecule

A remarkable example of a metastable configuration is the free-standing PTCDA molecule, a so called s-PTCDA, supported by two Ag adatoms and its long axis standing vertical to the Ag(111) surface. It can be used as a single electron field emitter [36]. While PTCDA only adsorbs flat on metal surfaces, it can be manipulated into an upright (standing) configuration with an SPM tip (see section 3.2.3). Its minimum stabilization potential has been measured to be around 26 meV [37].

T. Esat et al. were unable to topple s-PTCDA by tip manipulation [36], as attractive forces between the tip and the molecule stabilise the standing configuration. The molecule tilts on its pedestal when pulled laterally. After a force threshold is exceeded, the attached Ag adatoms will jump to neighbouring hollow sites of the Ag(111) surface while the molecule remains in a standing configuration.

s-PTCDA on the tip as SQDM sensor

Scanning quantum dot microscopy (SQDM) uses a quantum dot (QD) at the tip as a probe for the local electric field [38]. The principle of operation is to detect the difference in electron charge of the QD, which is gated by local charges on the surface. A mechanical connection is required between the tip and the QD, which at the same time decouples them electrically. From two-contact manipulation experiments it is known that a carbonyl group, as found in PTCDA, fulfils the requirement for a rigid connection. Additionally, the peak-dip feature (see section 3.2.3) in the Δf signal is reproducible for lifting and approaching PTCDA on a vertical trajectory on Ag(111), indicating that the molecule remains standing (s-PTCDA configuration) on the SPM tip after its detachment from the surface [11, 13]. Due to the s-PTCDA configuration, the π-orbital of its perylene backbone does not overlap with the metal states of the tip. Indeed, the tunnelling of single electrons on and off a PTCDA QD is observed, and thus, PTCDA can be used as an SQDM sensor [38].

To equip a Ag-terminated tip with s-PTCDA for SQDM, an isolated molecule is contacted at one O_{carb} and retracted vertically until the molecule is completely detached from the surface. The full observation of the peak-dip feature in the Δf signal and a smooth transition to zero afterwards during the retraction indicate that the molecule remains in a vertical configuration on the tip even after detaching it from the surface. This is tested by reapproaching the surface and observing the onset of the peak-dip feature at the same tip height as during lifting. If this is not observed, then the molecule has either fallen back to the surface or has flipped up and adsorbed flat on the tip.

A single Ag-O contact is formed between the tip and PTCDA for lifting, while the

molecule is adsorbed flat on the surface. Therefore, it has been assumed that the molecule is still only connected by this single bond to the tip in the vertical configuration after detachment from the surface. Recent theoretical studies suggest that there are two Ag-O bonds to the tip [37, 39]. Thus, the second O_{carb} attaches itself at some point during the lifting process. This conclusion is also evidenced by the results of section 4.3.

3.3 Hand-controlled two-contact manipulation: A state-of-the-art overview

3.3.1 Introduction

As discussed in section 3.2, two-contact manipulation would greatly benefit from intuitive 3D tip control. However, it can be already challenging to manipulate nanometre-size objects along simple (1D) SPM tip trajectories. Extending their manipulation to arbitrary 3D trajectories adds a new dimension of complexity. Controlling 3D tip motion is very difficult and calls for intuitive access to the xyz tip coordinates and augmented feedback to assist the experimenter during the manipulation.

Hand-controlled manipulation (HCM) provides intuitive 3D molecule manipulation by equipping an SPM with a motion capture system (MCS) and fully immersive virtual reality (VR) goggles. The MCS uses infrared cameras to track the position of a handheld object. Its movements are coupled to the SPM tip using an appropriate scaling factor. The cameras are equipped with a ring array of LEDs, that shine infrared light on the tracked object. The tracked object in turn is equipped with infrared reflectors as well as infrared LEDs. The use of infrared light reduces the effect of the environment on the tracking. The VR goggles display the current tip position and the executed HCM trajectories in 3D. The junction response is provided by colour coding the executed trajectory at its current position according to the I or Δf signal. The spatial movement of the goggles is also tracked. This allows the experimenter to intuitively change the viewing angle on the trajectories in the VR environment by changing the head position, thus simplifying reproducible execution of previous trajectories.

In summary, the experimenter's hand movement controls the positioning of the SPM tip while the VR goggles provide a real-time visualisation of the tip trajectories and SPM junction response in 3D. HCM can be activated or deactivated at any point during the SPM operation, allowing free switching between "standard" SPM operation and HCM.

This section discusses HCM as presented in [21, 40, 41]. The video tutorial in [41] shows the experimental execution of HCM in the laboratory. Section 5.2 presents a further development, reimplementing and extending the previous functionality using the game engine Unity™, and section 5.3 discusses its application for reproducible charge transport studies of an isolated molecule.

3.3.2 Experiments

HCM was first introduced by Green et al. [21] in 2014. They demonstrated the controlled patterning of a PTCDA/Ag(111) monolayer by extracting 48 molecules one at a time to write

a predefined structure into the layer (see section 2.3 for the sample preparation). Fig. 3.4a,b show the written structure and the successful manipulation trajectories which allowed to fully detach the molecules from the layer.

While the covalent Ag-O bond between tip and molecule is sufficient to detach a single adsorbed PTCDA molecule from the Ag(111) surface, the H-bonds between the molecules prevent successful lifting of a layer molecule on a vertical trajectory. Fig. 3.1 shows a sketch of the H-bonds. The molecule has to be manipulated along a specific 3D trajectory that allows sequential breaking of the H-bonds while keeping the retaining molecule-surface and intermolecular forces below the breaking threshold of the tip-molecule bond.

The experimenter uses HCM to find this specific 3D trajectory by trial and error. First, the experimenter uses the SPM software to position the SPM tip over a O_{carb} of the target PTCDA molecule. The control is then switched to the HCM equipment and the experimenter begins with a vertical manipulation to set up the VR environment for further manipulation of the target molecule. The O_{carb} is approached by locking the lateral xy directions of the tip and moving the hand downwards. When observing the Ag-O bond formation, the hand is moved upwards until the Ag-O bond ruptures. This is indicated by a sharp drop in the tunnelling current, which tends towards zero. Now the movement restrictions of the SPM tip are removed and this vertical manipulation serves as a visual guide in the VR environment, allowing fast re-establishing of the Ag-O bond after a preliminary bond rupture during future exploration. A preliminary bond rupture refers to the loss of contact with the molecule before the desired target configuration is achieved After the loss of contact, the molecule typically returns to its original site, guided by surface-molecule and intermolecular forces. The cycle of manipulating the molecule on an arbitrary tip trajectory, preliminary bond rupture, and re-establishing of the Ag-O bond is repeated until the molecule is successfully detached from the substrate surface. The characteristic signals indicating tip-molecule bond formation and successful detaching of a molecule from the surface are discussed in section 3.2.3.

An early version of HCM was used for the work described above, without the additional help of VR feedback. Providing the experimenter with a 3D real-time visualisation via fully immersive VR goggles not only allows for skill transfer between different operators (by displaying a reference trajectory as a visual guide during the manipulation), but also allows for intuitive and fast refinement of the manipulation trajectory as well as controlled repeated manipulation [40, 41].

The Ag-O bond strength between tip and molecule is determined by the atomic structure of the tip apex. Due to the stochastic nature of the apex formation during tip preparation, a successful trajectory is only valid for the specific tip [42]. Deposition of the lifted molecule back onto the surface and also, though rarely, rupture of the tip-molecule bond can cause a change in the tip apex. Therefore, an average reference curve can only be used as a guide.

The strength of the VR environment is that it allows systematic refinement of the manipulation trajectory to adjust for the current tip geometry. In the search for a successful lifting trajectory, the experimenter can follow previous promising trajectories and make distinctive variations. A successful trajectory can be found in a few trials even if it differs significantly form the reference curve, as in Fig. 3.4c. Furthermore, a manipulation trajectory for a specific tip can be executed repeatedly using HCM, showing remarkable consistency in the

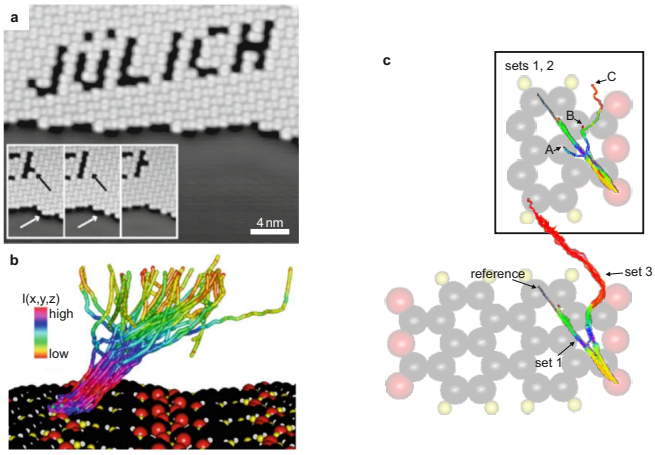

Figure 3.4: Results from hand-controlled manipulation for lifting individual molecules from a monolayer of PTCDA/Ag(111). **a**, STM topography image (setpoint: −0.35 V, 0.1 nA). The word "Jülich" was written by removing 48 PTCDA molecules with HCM. The insets show the successful correction of a writing error. **b**, The individual lifting trajectories of the molecules removed in **a**. **c**, Demonstration of the control during HCM, allowing highly reproducible $I(x, y, z)$ and $\Delta f(x, y, z)$ along the executed trajectories (Δf not shown). The trajectories in set 1 follow the reference curve (the average trajectory from **b**), which did not allow lifting of the molecule for the specific tip. A successful trajectory (set 3) was found after only three attempts (set 2: A, B, C), as shown in the inset.

experimental signals of I (x, y, z) and Δf (x, y, z), as shown in set 3 of Fig. 3.4c.

3.3.3 Program features

This HCM version consists of the following programs written in either the programming language C# or C++: MCS interface (motion capture system; C#; written by: M. Green, T. Esat), FFSim (force field simulation; C++; written by C. Wagner), VR interface (C++). Fig. 3.5a shows a screenshot of the VR interface (the VR environment) and Fig. 3.5b shows a sketch of the digital connections between the scripts (see section 2.3 for analogue connections). The MCS interface receives the detected position of the tracked object from the MCS, converts it to voltages, and sends it to the RVS (remote voltage supply). It also forwards the position to FFSim. The FFSim either just forwards the tip coordinates to VR interface or additionally calculates the mechanical response of a PTCDA molecule to the tip movement on Ag(111) and sends the current coordinates of its atoms. The VR interface renders the VR environment and interacts with the ADC (analogue digital converter) for data acquisition.

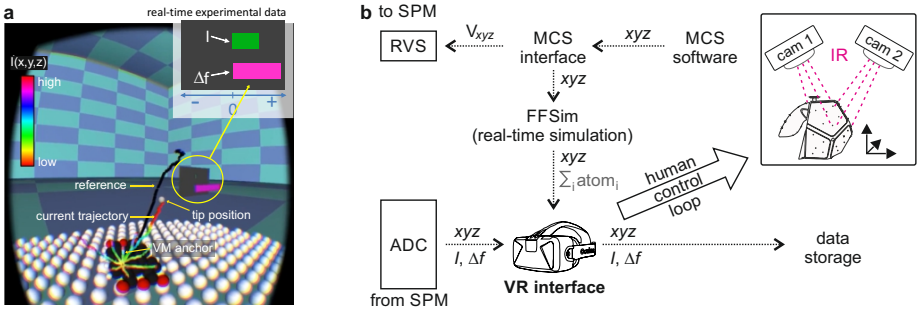

Figure 3.5: HCM software version written in C++. **a**, Screenshot of HCM (VR interface) during the task of removing a molecule from a PTCDA on Ag(111) layer. **b**, Schematic of digital data flow for the C++ version of VR interface (analogue connections are not shown).

SPM tip control

The Vicon™ system allows the tracking of a special object (e.g. Vicon Apex™) which is moved by the experimenter's hand. This movement is converted into the movement of the SPM tip (with a conversion of 1 Å/5 cm). It would also be possible to turn three rotary knobs to control the 3D tip movement, which is indeed a useful alternative for less complex 3D trajectories (see section 3.2.3). However, for complex trajectories where all xyz coordinates need to be manipulated at the same time, intuitive control becomes important. Tracking the operator's hand movements provides an ergonomic method of entering a 3D trajectory into a computer. In addition, repeating a previously executed hand movement is highly intuitive, even with eyes closed, and can be exploited for fast and reproducible execution of manipulation trajectories.

It should be noted that in the current version of the program the experimenter has to be in front of a keyboard and press the appropriate key to start, stop, or pause a trajectory recording.

Augmentation

Using previously executed trajectories as a guide is only possible with a true 3D visualisation of the manipulation during the execution of the experiment. This would be very difficult if the experimenter had to watch a 3D rendered scene projected on a 2D screen, due to perspective. Therefore, 3D visualisation is essential for precise HCM. Using an Oculus Rift DK2™ as fully immersive VR goggles allows not only 3D viewing, but also adjustment of the viewport by moving and rotating the experimenter's head.

As Fig. 3.5a shows, the VR environment supports the experimenter with visual aids during the manipulation experiment. The executed manipulation trajectories are colour-coded with either the I or Δf signal. Their real-time values are displayed as a bar graph next to the current tip position, marked by a white sphere. Since distances in a VR environment are in principle arbitrary, it is important to provide the experimenter with an intuitive

ruler. In this case, it is a PTCDA molecule that can be freely rotated to match the target molecule of the experiment. The black reference trajectory was extracted by averaging the trajectories from Fig. 3.4c, each of which resulted in the successful removal of one molecule from the PTCDA/Ag(111) monolayer.

Note that currently there exists no menu for selecting functions during program execution. They must be set in the source code (requiring recompilation of the application needed) or activated by pressing the corresponding key on a keyboard during program execution.

Data storage

The recording of a manipulation trajectory is started and stopped manually. In addition to displaying all recorded manipulation trajectories in VR interface, each trajectory is automatically saved to a separate file containing: the xyz trace, I, and Δf.

CHAPTER 4

Application of vertical manipulation

4.1 Overview

The conventional method of lateral on-surface manipulation is the translation of the SPM tip in a straight line. The equivalent of this for two-contact manipulation is the lifting of molecules with a vertical tip trajectory.

While lateral manipulation is used to move nanoscale objects on the surface, by pulling or pushing, vertical manipulation is able to detach objects from the surface for a pick-and-place construction task. Additionally, vertical two-contact manipulation allows the characterisation of charge transport and the mechanical properties of molecules in different junction configurations (see section 3.2).

Automated vertical two-contact manipulation on a grid is used to systematically characterise the contact formation of the tip with a PTCDA/Ag(111) monolayer and to probe the intermolecular interactions within the layer in section 4.2. The tip-molecule bond is investigated in section 4.3 by vertical two-contact manipulation of a PTCDA molecule attached to an artificial tip apex on the surface.

4.2 Probing intermolecular interactions by molecular manipulation

4.2.1 Introduction

The adsorption of large organic molecules is often influenced by their functional groups, which can interact simultaneously with the surface and with neighbouring molecules [33, 34, 43]. Together with the structural flexibility, this leads to a multidimensional, highly structured but at the same time rather shallow interaction potential landscape, which can hardly be investigated by any means other than theoretical simulations. Under these circumstances, experimental data serve as an important benchmarking against which to compare theory. Unfortunately, most of the experiments provide only equilibrium structure data as a reference (e.g. adsorption height and energy, lattice constants, molecular distortions, level alignment, etc.) [44, 45, 46] although characterisation of larger regimes of the high-dimensional potential energy surface (PES) is much more desirable, as the latter facilitate a more stringent comparison to the theory.

Controlled manipulation of single molecules with the tip of an SPM can be used to probe lattice regions of the molecular PES by moving the manipulated molecule along specific trajectories of its conformation space [12, 21, 40, 15]. This can be done by using two-contact manipulation, where the SPM tip contacts the molecule at a single well-defined point, while the environment (surface and/or neighbouring molecules) provides a second contact relative to which the molecule can be manipulated (see section 3.2).

Here, an SPM is used to probe the interactions in the archetypal model monolayer system of PTCDA/Ag(111). This system is of particular interest due to the strong influence of the interplay between the intermolecular interactions and the adsorption state on the electronic properties.

A single PTCDA molecule chemisorbs on Ag(111) via two binding mechanisms: First, its π-orbitals hybridise with metal states, resulting in a charge transfer into its former LUMO. Second, the four O_{carb} atoms at the corners of PTCDA bond locally to the surface. This involves a significant distortion of the molecule, with the O_{carb} bending towards the surface.

The intermolecular interactions within the layer reduce the distortion of the molecule, increase the adsorption height, and thus, reduce the charge transfer [34]. This was explained with a schematic model where the carboxylic oxygen O_{carb} atoms of PTCDA, acting as "surface anchors", are also attracted by the H atoms of the neighbouring molecules (Fig. 4.1a-c). The H atoms are believed to be further away from the surface than the O_{carb} atoms. Therefore, it was proposed that their H-bond-like attraction competes with the Ag-O bonds, thus increasing the adsorption height of the whole molecule and reducing the overlap of its π-orbitals with the Ag(111) surface [34, 47]. The Ag-O bonds could be further weakened by a charge transfer associated with the O-H interaction, as this charge is no longer available for the Ag-O bond [34, 47].

The characterisation the O-H interaction is central to a detailed understanding of the properties of organic monolayers on metal surfaces, not only in case of PTCDA, but for any molecular species with polar functional groups.

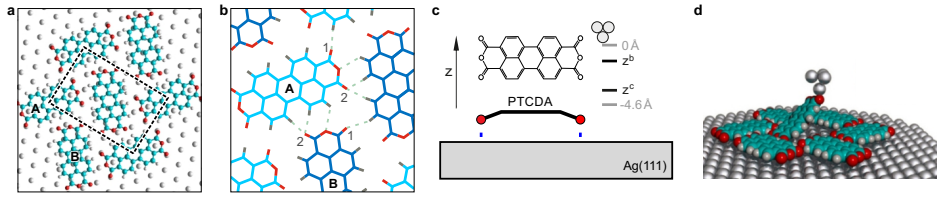

Figure 4.1: Structural properties and interactions of PTCDA/Ag(111). **a**, The nearly rectangular unit cell of PTCDA on Ag(111) (black, 18.96×12.61 Å^2, tilted by 1°) contains two molecules with distinct adsorption sites. Molecule A is aligned with the underling Ag(111) lattice, while molecule B is misaligned. **b**, The O_{carb} are either in the vicinity of one hydrogen (type 1) or two hydrogens (type 2). **c**, Structural formula and schematic side view of PTCDA bonding to Ag(111). The important heights during a manipulation are sketched on the right side. **d**, Rendered scene of a PTCDA molecule being partial lifted from the layer with a Ag-terminated tip.

4.2.2 Experiment

A coverage of 10 % of a monolayer of PTCDA was deposited on Ag(111) as described in section 2.3. PTCDA on Ag(111) grows in a commensurate lattice with two inequivalent molecules in the unit cell. They are typically referred to as aligned (A) and misaligned (B) with respect to the underlying Ag(111) lattice (Fig. 4.1a). Fig. 4.1c shows a sketch of the distorted adsorption geometry of PTCDA/Ag(111) with its four O_{carb} atoms bending towards the surface and forming Ag-O bonds, due to the molecule-surface interaction (see section 3.2.2).

The PTCDA/Ag(111) was manipulated by approaching and retracting the tip vertically at different lateral positions on the surface. The amplitude of the qPlus oscillation used in the experiment was 0.2 Å (see section 2.3). The response of PTCDA/Ag(111) was analysed by inspection of the recorded current $I(x, y, z)$, frequency shift $\Delta f(x, y, z)$ and dissipation $\delta(x, y, z)$ signals.

In case a bond between the tip and PTCDA is formed as the tip approaches, the contacted PTCDA molecule may follow the tip as it retracts away from the surface (Fig. 4.1d). When the strength of the intermolecular and surface interactions exceeds the strength of the tip-molecule bond, the tip-molecule bond breaks and the molecule "drops" back to its original adsorption site. In this manner the system is "reset" into its original state after *each and every* manipulation cycle. This was helpful to perform a large number of single molecule manipulation cycles, systematically varying the lateral position of the tip approach. The data obtained is highly reproducible and clearly shows the dependence of the response of PTCDA/Ag(111) on the contact position. This dependence provides an insight into the interactions present in the contacted monolayer.

Each individual manipulation cycle proceeds as follows: the tip approaches the surface for 4.6 Å and retracts back vertically to the starting position defined as $z = 0$ (Fig. 4.1c, Fig. 4.2a). During a manipulation, a bias voltage of −1 mV was applied while $I(z)$, $\Delta f(z)$ and $\delta(z)$ were simultaneously recorded. In rare cases, the tip-molecule contact remained intact until the point of maximum tip retraction. A voltage pulse of V =−200 mV was

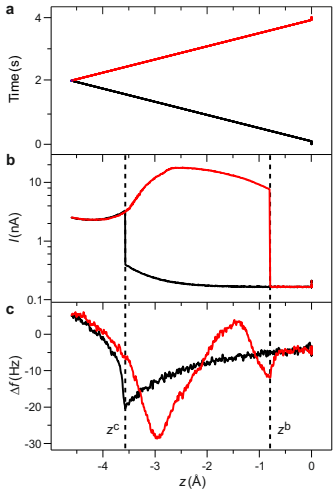

Figure 4.2: Manipulation parameters and data recorded of a VM of PTCDA/Ag(111) in the vicinity of B_2. The approach is coloured in black and the retraction in red. **a**, Manipulation z ramp. First the tip approaches 4.6 Å towards the surface, then retracts back to the starting position ($V = -1$ mV). Between manipulations, a voltage pulse is applied. **b**, $I(z)$ spectrum and **c**, $\Delta f(z)$ spectrum. The heights z^{c} and z^{b} are extracted from **b**.

applied at $z = 0$ to ensure its cleavage and return of the molecule to its original position within the monolayer.

Two values are extracted from the recorded data: the height $z^{\mathrm{c}}(x, y)$ of contact formation and the height $z^{\mathrm{b}}(x, y)$ at which the Ag-O bond to the tip breaks. Fig. 4.2b,c shows how the values $z^{\mathrm{c}}(x, y)$ and $z^{\mathrm{b}}(x, y)$ are determined. z^{c} and z^{b} are extracted from $I(z)$ curves. Sharp changes in the I signal indicate the formation and breaking of the tip-molecule bond (Fig. 4.2b). The $\Delta f(z)$ curves show a similar response. However, due to a the higher bandwidth of the I measurement, the $I(z)$ curves proved to be a better option for extracting z^{c} and z^{b}.

The manipulation was performed over an area of $30{\times}30\,\text{Å}^2$ at each position of a 64x64 pixel grid, resulting in three "data cubes" (I, Δf and δ) spanning an (x, y, z) volume of $30{\times}30{\times}4.6\,\text{Å}^3$ each. Fig. 4.3 shows slices of the I cube taken at four different values of z. The respective plots show that the manipulation is fully reversible and affects neither the atomic structure of the tip apex nor the structure of the PTCDA monolayer.

4.2.3 Results and discussion

The tip pulls PTCDA away from its equilibrium adsorption geometry during manipulation. If it were possible to displace each and every atom of the molecule independently, then the complete area of the PES in the vicinity of the equilibrium adsorption geometry would be

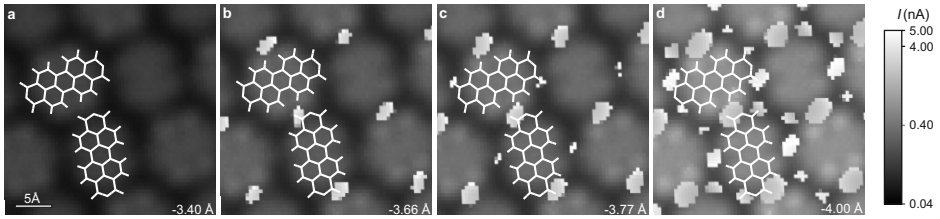

Figure 4.3: Height slices through $I(x, y, z)$ data of 3D dataset for the tip approaching PTCDA on Ag(111), measured with qPlus oscillation and $V_{\text{bias}} = -1\,\text{mV}$. The height given in each slice corresponds to the distance the tip approached towards the surface from the set point. Areas of high current indicate the presence of a tip-molecule bond. **b-d**, Bond formation around positions of O_{carb}. **d**, Additional observation of contact over the perylene core of molecule A.

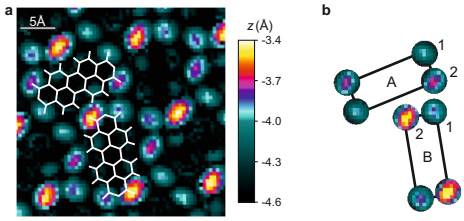

Figure 4.4: Contact heights extracted from approach spectra, of the grid in Fig. 4.3. **a**, $z^{\text{c}}(x, y)$ map overlayed with the herringbone structure of PTCDA on Ag(111). Colour code: black for no contact, all other colours mark contact formation between tip and molecule at different heights. **b**, The four species of O_{carb} in the order they jump towards the tip, starting furthest away from the surface: B_2, A_2, B_1, A_1.

characterised. In reality, pulling the molecule with the tip displaces many atoms at once, thus creating complicated trajectories around the equilibrium position in the multidimensional configuration space of the molecule.

Nevertheless, one may assume that only one oxygen atom of the PTCDA flips up towards the tip at z^{c}, while all the other atoms remain more or less in their initial positions [16]. Thus, the tip-molecule contact event mostly probes the interactions of the displaced oxygen atom with its environment. On the contrary, breaking of the tip-molecule bond occurring at z^{b} probes interactions of the entire molecule, because large parts of the molecule are (about to be) displaced and deformed during the lifting.

Tip-molecule contact formation

Flipping of the oxygen towards the tip occurs due to the deformation of the PES of the oxygen atom by the presence of the tip that attracts it. This deformation increases as the tip approaches until the jump-to-contact occurs, when the PES minimum around the oxygen atom becomes a saddle point [16]. This happens when the original PES gradient matches

the (negative) gradient of the tip-oxygen potential or, put simply, when the force pulling the oxygen atom towards the tip exceeds the retaining force originating from the molecular PES. Since the tip does not change during the experiment, variations in z^{c} between different $\mathrm{O_{carb}}$ atoms reflect the differences in the PES seen by the various $\mathrm{O_{carb}}$ atoms of PTCDA. The lateral variations of z^{c} above one and the same oxygen atoms, on the other hand, directly reflect the dependence of the tip-oxygen interaction on the tip-oxygen distance.

It is found that z^{c} varies substantially as the contact point shifts along the surface (Fig. 4.4). First, as expected, the contact forms only over the carboxylic oxygen atoms of PTCDA. Second, z^{c} varies significantly between the non-equivalent oxygen atoms of the PTCDA/Ag(111) unit cell. Due to the structure of the unit cell, each of the two molecules (A and B) has two pairs of inequivalent $\mathrm{O_{carb}}$ atoms. Each pair differs in the position of the $\mathrm{O_{carb}}$ atoms relative to the underlying Ag(111) lattice (for B only) and relative to the neighbouring PTCDA molecules (Fig. 4.1a,b). These $\mathrm{O_{carb}}$ atoms will be abbreviated as: $\mathrm{A_1}$, $\mathrm{A_2}$, $\mathrm{B_1}$, and $\mathrm{B_2}$. The numbers correspond to the number of H-bonds of the respective $\mathrm{O_{carb}}$ (Fig. 4.1b). Therefore, $\mathrm{O_{carb}}$ with one (two) H-bond(s) will also be referred to as type 1 (type 2) oxygen. The observed variations in z^{c} show that these oxygen atoms experience rather different PES landscapes. Note that, in agreement with the previously published data, an attraction of the tip towards four sites over the C-H bonds of PTCDA is also observed [48, 49].

The z^{c} map shown in Fig. 4.4 yields the following average values: $z^{\mathrm{c}}_{\mathrm{B_2}} = (-3.44 \pm 0.02)$ Å, $z^{\mathrm{c}}_{\mathrm{A_2}} = (-3.69 \pm 0.02)$ Å, $z^{\mathrm{c}}_{\mathrm{B_1}} = (-3.81 \pm 0.02)$ Å and $z^{\mathrm{c}}_{\mathrm{A_1}} = (-3.90 \pm 0.02)$ Å. It is insightful to find out what forces cause the observed variations of z^{c}.

Forces on carboxylic oxygen atoms

The background forces, due to the tip-surface interaction and the interaction of the tip with the PTCDA monolayer, need to be subtracted from the force data to estimate the forces required to flip the $\mathrm{O_{carb}}$ atoms to the tip. To do so, the force measured at a position *between* the molecules of a PTCDA monolayer is subtracted from the force obtained *at the centre* of a molecule (black and yellow dashed curves in Fig. 4.5a). The only difference between the two lateral positions is that some (carbon) atoms just below the tip are present in one case and absent in the other, while the background forces are practically identical. This allows the background to be completely removed by subtraction. The resulting force curve will be referred to as $F_z(z)$ in the following.

What does the background corrected $F_z(z)$ actually correspond to? The unit cell of a PTCDA monolayer has an area density of $0.37\,\text{Å}^{-2}$ for carbon atoms and an "empty" space of about $6 - 8\text{Å}^2$ between the molecules. It follows that $F_z(z)$ corresponds to the interaction of the tip with 2-3 C atoms.

Taking into account the lower van der Waals (vdW) C_6 coefficient of oxygen compared to carbon (about 0.67) [13], the tip-oxygen force can be estimated to be smaller, by a factor of 0.28 ± 0.06. In conclusion, $F_z^{0.28}(z) = 0.28\,F_z(z)$ can be used to estimate the force required for a $\mathrm{O_{carb}}$ to flip to the tip. Note that the interaction of the tip with the oxygen atoms for the tip position above the "empty" space was neglected in the determination of $F_z(z)$.

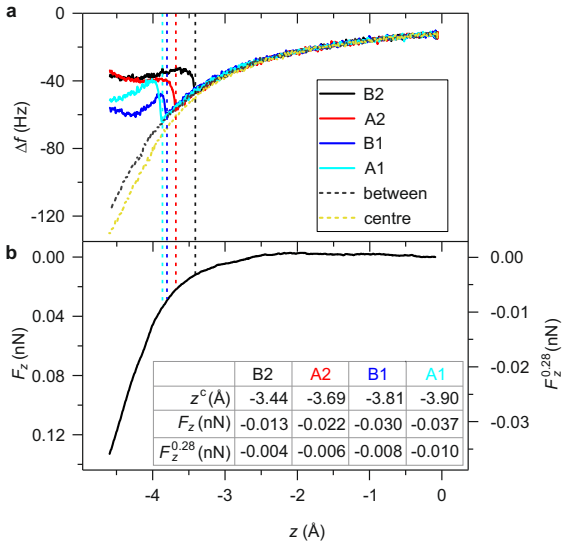

Figure 4.5: AFM spectra of approaching PTCDA/Ag(111) and extracted forces. **a**, $\Delta f(z)$ spectra at different lateral positions for the approach. **b**, The background corrected local force acting on the tip. Local $F_z(z)$ is calculated by subtracting the spectrum taken between the molecules from the spectrum taken in the centre of the molecule. $F_z^{0.28}(z)$ gives the local force scaled with a factor of 0.28 and is used to extract the relative forces over the O_{carb} atoms. For further information see text.

Therefore, $F_z^{0.28}(z)$ servers as a lower estimate of the forces acting on the O_{carb} atoms during the tip approach.

Fig. 4.5b shows how the local tip-oxygen force increases with decreasing tip-sample distance. One obtains the pulling forces that flip the respective oxygen atoms up to the tip by evaluating the force at the corresponding z^c values. Unlike the absolute force values, the *relative* variations in the required tip-oxygen force can be determined rather accurately due to cancellation of the uncertainties related to the above-introduced scaling factor. From Fig. 4.5b one finds that the force required to flip A_1 to the tip is about 2.8 times stronger than the force for B_2. It is this increase that is responsible for the variations in z^c: If a stronger force is required to flip the oxygen atom to the tip, the contact will form at a smaller tip-surface distance.

Summarizing, a strong variation in the force that flips up the oxygen atoms of PTCDA in the layer was found. As these O_{carb} atoms are chemically identical, the variations in their PES must be the result of different surroundings of these atoms in the layer. Three effects could contribute: (1) A variation in the *native* adsorption height of the oxygen atoms above the Ag(111) surface. (2) The influence of the different positions relative to the underlying Ag lattice. (3) The influence of the neighbouring molecules.

(1) Variations in the *native* oxygen heights of a magnitude similar to the z^c variations are

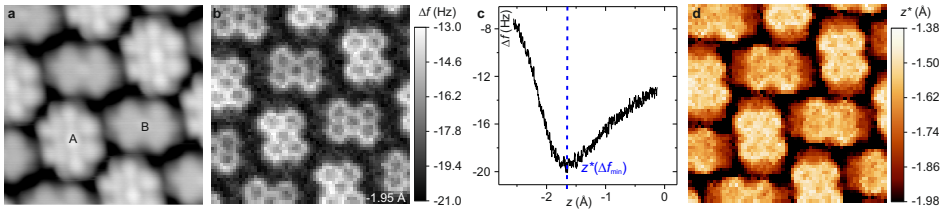

Figure 4.6: Height variation of PTCDA/Ag(111) measured with a CO-terminated tip. The perylene backbone of molecule A is (0.05 ± 0.01) Å further away from the surface than for molecule B. **a**, STM topography image with a CO-terminated tip (3x3 nm^2, $I = 0.05$ nA, $V = 16$ mV). **b**, Height slice through $\Delta f(z)$ spectra of a 3D dataset showing the perylene backbone of the PTCDA molecules. **c**, Example $\Delta f(z)$ approach spectrum labelled with the position of $z^*(\Delta f_{min})$. **d**, Map of $z^*(\Delta f_{min})$ for the tip approaching the surface, revealing the adsorption geometry of PTCDA on Ag(111). Bright colours correspond to distances further away from the surface than dark colours.

clearly incompatible with the near-incidence X-ray standing wave (NIXSW) measurement performed on PTCDA/Ag(111) [47, 43]. However, small variations in these heights between A and B molecules are imaginable. To determine the *relative* adsorption heights of A and B molecules, the procedure published by Schuler et al. [50] was followed, in which the heights $z^*(x, y)$ corresponding to the minimum $\Delta f(x, y, z)$ measured with a carbon monoxide (CO-)modified tip were extracted.

The $z^*(x, y)$ map obtained in Fig. 4.6d shows that the perylene core has no distortion, but the oxygen atoms are tilted towards the surface in agreement with NIXSW data [47]. Determined from Fig. 4.6d, the perylene core of A is (0.05 ± 0.01) Å further away from the surface than that of B. This is in remarkable agreement with a theoretical prediction of 0.06 Å obtained using density functional theory (DFT) calculations in the local-density approximation (LDA) [51]. Since A is found to have a larger adsorption height, while z^{c} is lower for these molecules, one can rule out the possibility that the z^{c} variations are explainable by effect (1).

(2) Molecule A is aligned with respect to the Ag lattice (Fig. 4.1a), hence all of its $\mathrm{O_{carb}}$ atoms have the same (lateral) position over the underlying Ag atom and therefore their interaction with the surface is the same. Nevertheless, a difference $\Delta z_c^{\mathrm{A}_{1,2}} = 0.21$ Å is found between $\mathrm{A_1}$ and $\mathrm{A_2}$ (Fig. 4.4). One can conclude that the alignment with respect to the Ag lattice and hence the interaction of $\mathrm{O_{carb}}$ atoms with the surface cannot explain the observed variations of z^{c}. A similar argument can be applied to molecule B, where $\mathrm{B_1}$ and $\mathrm{B_2}$ are offset by almost the same (lateral) distance from their nearest underlying Ag atoms, while $\Delta z_c^{\mathrm{B}_{1,2}} = 0.37$ Å.

(3) After discussing effects (1) and (2), it turns out that z^{c} variations of the observed magnitude can only arise from a varying strength of intermolecular interactions. These interactions are dominated by weak hydrogen bonds [52] which form between hydrogen atoms and the $\mathrm{O_{carb}}$ atoms of adjacent molecules. According to the monolayer unit cell structure, type 1 oxygen atoms engage in one hydrogen bond, while type 2 oxygen atoms engage in two of such bonds (Fig. 4.1b).

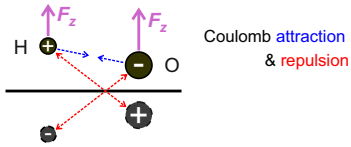

Figure 4.7: Schematic of the O-H coulomb interactions including image charges due to the metal substrate.

Naively, one might therefore assume that type 2 oxygen atoms are more strongly held inside the layer and that more force is required to pull them upwards to the tip. This is however opposed by the experimental findings.

In [34, 47], it was stated that for the O_{carb} atoms the intermolecular upwards O-H attraction competes with the downwards surface-molecule Ag-O attraction. Additionally, the Ag-O bonds could be weakened by a charge transfer related to the O-H interaction, which would reduce the charge available for the Ag-O bonds. Both effects would be expected to be stronger for type 2 oxygen atoms.

Image charges could also play a role in the different behaviour of type 1 and 2 oxygen atoms. To explain this, we will take a closer look at the nature of electrostatic intermolecular interactions in the presence of a metal surface.

Electrostatic interaction in the adsorbate layer

To analyse the electrostatic intermolecular and surface-molecule interactions one may model the charge distribution within molecules and the surface by placing partial charges on individual atoms of the molecule and assume a screening of these charges by respective image charges in the metal [38]. The Coulomb energy of two such atoms with charges Q_1 and Q_2 at heights z_1 and z_2 above the surface (i.e. the electrostatic image plane) and laterally separated by a distance x is given by

$$E = \frac{1}{4\pi\epsilon_0}\left(\frac{Q_1Q_2}{\sqrt{x^2+(z_1-z_2)^2}} - \frac{Q_1Q_2}{\sqrt{x^2+(z_1+z_2)^2}} - \frac{Q_1^2}{2z_1} - \frac{Q_2^2}{2z_2}\right) \tag{4.1}$$

At large separations $x \gg z_{1,2}$ only the last two terms contribute significantly, which simply describe the interaction of each atom with its own image charge. This interaction can be understood as a part of the total atom-surface interaction (together with e.g. the vdW interactions) which determines the equilibrium adsorption heights z_1 and z_2 for the separated atoms.

With decreasing separation x the other two terms in eq. (4.1) become also relevant. Fig. 4.7 shows a sketch of the coulomb interaction.

In a hypothetical *absence* of the surface there would only be the first term, the direct interaction between the charges. For example, in the case of an O-H interaction with respective partial charges δ^- and δ^+, this contribution is negative, resulting in a mutually attractive force.

However, in the *presence* of the metal surface there is also the second term which describes the interaction of each charged atom with the image charge of the other atom. In case of the O-H interaction, this term increases E, implying a repulsive force between the charge and the opposite image charge. The direction of this force is *unequal* to the direction of the direct force in the first term. In particular, there is a rather strong component that pushes both atoms *away* from the surface (in case of opposite charges).

The force on atom 1 in z-direction is

$$F_{z1} = \frac{Q_1 Q_2}{4\pi\epsilon_0} \left(\frac{z_1 - z_2}{[(z_1 - z_2)^2 + x^2]^{3/2}} - \frac{z_1 + z_2}{[(z_1 + z_2)^2 + x^2]^{3/2}} \right) \tag{4.2}$$

The first term of this expression results from the direct interaction between the charges and yields zero for $z_1 = z_2$, while the second term yields a positive force for oppositely charged atoms. From the experimental results it can be concluded that, due to their interaction with *two* positively charged adjacent H atoms, type 2 oxygen atoms experience a stronger repulsion from the surface than type 1.

Summarizing the arguments that explain why type 2 oxygen atoms are more weakly bound than type 1: First, a O_{carb} is closer to the surface than the H atoms of the neighbouring PTCDA molecule. Thus, the O-H attraction competes with the Ag-O bond [47]. The O-H attraction is stronger for type 2 oxygen atoms. Second, the charge transfer due to the O-H interaction reduces the charge on the O_{carb} atom available for the Ag-O bond to the surface, directly weakening this bonds [47]. This charge transfer is stronger for type 2 oxygen atoms [53]. Third, while the attraction of the O_{carb} to its image charge is similar for type 1 and 2, the latter experiences the repulsion of two H-image charges.

Tip-molecule bond breaking

As was shown above, contacting of the oxygen atoms of PTCDA with the tip probes the PES of these atoms. Lifting PTCDA by retracting the tip probes, on the other hand, the PES of several atoms of the molecule. Contacting and lifting the molecule at different lateral positions leads to distinctly different trajectories in its conformation space. This allows the characterisation of different parts of its PES, ideally by recording the forces acting on the tip during the manipulation.

Unfortunately, in the disruptive events of bond formation and bond breaking, the force on the tip changes by an unknown amount. This renders the standard approach of obtaining forces by integration of $\frac{\delta F_z}{\delta z}(z)$ data inapplicable. Therefore, a simple geometric analysis is performed by considering the dependence of z^{b} (the height at which the tip-molecule contact breaks) on the lateral position of the contact point. This is based on the fact that the bond must break when an unknown but well-defined force between tip and molecule is reached.

Fig. 4.8a shows a map of $z^{\mathrm{b}}(x, y)$ extracted from the same manipulation dataset that was analysed above. As can be seen from Fig. 4.8a, z^{b} *increases* when the contacting point is moved from the centre of the O_{carb} atom of PTCDA further towards the *centre of the molecule*. In order to analyse the observed behaviour of the four non-equivalent O_{carb} atoms in more detail, a common coordinate system is required. Fig. 4.8b shows z^{c} and z^{b} line

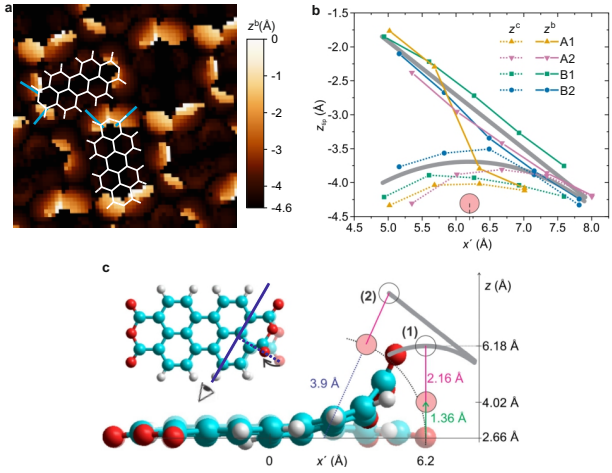

Figure 4.8: Analysis of tip-molecule bond breaking. **a**, $z^b(x, y)$ map at which the tip-molecule bond breaks. The gradient of $z^b(x, y)$ is indicated by the light blue lines. The origin of the asymmetry between oxygen atoms of the same type of the same PTCDA molecule lies most likely in a slightly asymmetric tip apex. **b**, z^c (dotted) and z^b (solid) line profiles along the white light blue lines in **a**. The O_{carb} position is indicated by a pink circle. The origin of the x axis is the centre of the respective molecule. The generic behaviour of the $z^c(x')$ and $z^b(x')$ curves is captured by the grey lines. **c** Analysis of the lifting process during the experiment based on the generic curves in **b**. The absolute z values are determined from theory [16] (see text). On tip approach to position (1), the O_{carb} jumps up 1.36 Å (green arrow) and forms a tip-molecule bond with a bond length of 2.16 Å (pink line). The bending radius obtained from an analysis of the $z^b(x')$ curve is approximately 3.9 Å. A model molecule computed with a force-filed approach [12] illustrates the lifting process. The bending axis, which is perpendicular to the drawing plane of the model, is shown as a blue line in the inset (top view of molecule).

profiles across A_1, A_2, B_1, and B_2 along the light blue lines in Fig. 4.8a (approximately the direction of the C-O_{carb} bond). x' is the lateral distance from the centre of the molecule. A tip-O_{carb} bond only forms for tip approaches in the range of 5 Å $< x' <$ 8 Å. z^c shows a spherical shape with the highest point above the O_{carb} at $x' = 6.2$ Å, as discussed earlier. z^b, on the other hand, increases practically linear towards the centre of the molecule. The fact that the lifting of the O_{carb} atom is limited to about 2 Å indicates that large parts of the molecule remain bound to their initial positions and that mainly the contacted corner of the molecule is lifted. Any lateral movement of the molecule also appears to be sufficiently constrained by the H-bond network (Fig. 4.1b), as indicated by hardly any lifting for $x' > 7$ Å.

To analyse the lifting behaviour further, a generic $z^c(x')$ and $z^b(x')$ curve is derived from the corresponding line profiles (grey curves in Fig. 4.8b). In Fig. 4.8c, the generic curves are plotted with respect to the whole molecule. Their correct z height is estimated from previous theory calculations performed for the jump-to-contact of an isolated PTCDA molecule on Ag(111) [16]. The calculation predicted, that the O_{carb} jumps up by 1.36 Å to form a tip-O_{carb} bond with a bond length of 2.16 Å. Together with the adsorption height of the O_{carb}

atoms of 2.66 Å from NIXSW, the absolute height of the z^{c} curve can be estimated to be $z \approx 6.2$ Å above the O_{carb} atom (empty circle (1) in Fig. 4.8c). This also defines the structure at the maximum z^{b} position (empty circle (2) in Fig. 4.8c). Combining these two fix points, one can estimate a bending radius of 3.9 Å for the initial phase of the lifting process. This estimate is significantly smaller than the length of the molecule and confirms the previous notion that a peeling motion is required to lift PTCDA out of the layer [21, 13, 40]. The contacted corner of the PTCDA molecule does indeed bend inwards towards the centre of the molecule. The bending axis is assumed to be along the solid blue line and therefore the maximum bending gradient is assumed to be along the dashed blue line (top view inset of PTCDA molecule in Fig. 4.8c). This hypothesis is supported by the molecular mechanics simulations [12, 54] used to generate the model geometries in Fig. 4.8c. They predict that all C atoms along the bending axis are at similar heights as seen in the (lifted) molecular model. The model geometries are orientated so that the bending axis points into the drawing plane, as indicated by the eye in the inset.

Summarizing, the data shows that a peeling motion in which the contacted corner of the PTCDA molecule is bent towards the molecule's centre is particularly suitable for the removal of PTCDA from a closed layer. This indicates that a molecule in a PTCDA/Ag(111) monolayer can neither slide laterally nor be stretched considerably without breaking the tip-O bond. The positions and heights at which the bond breaks indicate a considerable bending of the molecule during lifting and thus a progressive detachment from the surface and from the surrounding molecules.

Dissipation

Finally, the recorded dissipation data will be analysed to gain further insights into the junction dynamics. Dissipation is expected to be observed whenever a structural hysteresis occurs, due to establishing and breaking of the PTCDA-tip bond within the same oscillation cycle of the qPlus sensor. Consequently, one only expects to detect dissipation for tip positions x, y, z that satisfy the following condition: $z^{\mathrm{c}*}(x,y) - z^{\mathrm{b}*}(x,y) < 2A$, where A is the oscillation amplitude and where $z^{\mathrm{c}*}$ and $z^{\mathrm{b}*}$ are the hypothetical positions of z^{c} and z^{b} measured without oscillation of the tuning fork. Taking into account that z^{c} and z^{b} are measured with an oscillating tuning fork, the condition changes to

$$\Delta z = z^{\mathrm{c}}(x,y) - z^{\mathrm{b}}(x,y) = 0. \tag{4.3}$$

For a constant oscillating amplitude, z^{c} is measured at $z^{\mathrm{c}*} + A$, while z^{b} is measured at $z^{\mathrm{b}*} - A$.

Fig. 4.9a shows a histogram of the Δz values. z^{c} and z^{b} are extracted from the I signal. There is a large peak around $\Delta z = 0$, as is expected in the presence of dissipation (Fig. 4.9b,c). Interestingly, the peak is not centred around $\Delta z = 0$ but is slightly shifted to positive values. This suggests that there is an additional effect besides the random error in the extraction of z^{c} and z^{b}.

It is likely that the shift is related to a relatively slow amplitude control compared to the manipulation speed and high occurrence of tip-molecule bond rupture events. The total

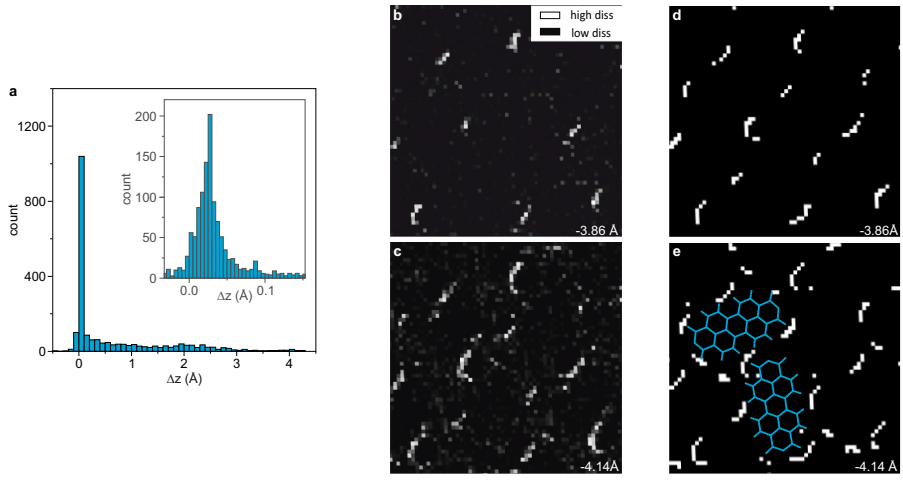

Figure 4.9: Measured vs predicted dissipation. The data shown is from the grid in Fig. 4.3. **a**, Histogram of $\Delta z = z^{\mathrm{c}} - z^{\mathrm{b}}$ for all spectra which show contact formation. **b**, **c**, Height slices through the qPlus dissipation signal during tip approach. **d**, **e**, Corresponding simulated dissipation defined by the conditions for z^{c} and z^{b} described in the text.

energy E_{tot} stored in the tip oscillation is of the order of a few meV ($A = 0.2\,\text{Å}$), while partially lifting a molecule could easily require tens or hundreds of meV. The energy E_{hyst} transferred to the potential energy of the molecule is however lost on every tip-molecule bond rupture, as the falling molecule transfers E_{hyst} to the surface. With $E_{\mathrm{hyst}} > E_{\mathrm{tot}}$ it follows that $E_{\mathrm{hyst}} \gg E_{\mathrm{damp}}$, where the latter is the energy lost during every oscillation cycle $E_{\mathrm{damp}} = -2\pi E_{\mathrm{tot}}/Q$ and $Q = 56,000$. It is clear that the controller will have difficulties to keep the amplitude constant when the hysteresis condition (eq. (4.3)) is reached.

If the controller is slow in comparison to the manipulation speed, there are scenarios where z^{c} and z^{b} are measured at unequal conditions. Here is one example scenario where the rest position of the tip is at $z^{\mathrm{c}*}$ and $z^{\mathrm{b}*} = z^{\mathrm{c}*} - 0.2\,\text{Å}$: If the z position is not changed, the oscillation would follow a cycle of reaching $z^{\mathrm{b}*}$, reduction of A to almost zero due to dissipation, restoring of A by the controller, and reaching $z^{\mathrm{b}*}$ again. Contact is re-established in the same cycle as the tip-molecule bond rupture, because the tip is at $z^{\mathrm{c}*}$. If the controller is slow, e.g. it takes 300 cycles to restore A, $z^{\mathrm{b}*}$ could be reached during retraction before A is fully restored and z^{b} would be measured later than compared to the full amplitude. This would shift the hysteresis condition within a possible range of $0 < \Delta z < A$. Note that since the typical time per z spectrum is around 1 s (each second increases the time required per experiment by 1 h), there are around 300 oscillation cycles per 0.1 Å ($f_0 = 31\,078\,\text{Hz}$, manipulation speed $\approx 10\,\text{Å/s}$).

The assumptions about the dissipation mechanism discussed above can be further validated by simulating dissipation maps during tip approach. For the simulated maps in Fig. 4.9d,e it is assumed that dissipation occurs for all x, y, z if $z < z^{\mathrm{c}}$ and $\Delta z(x, y) < 0.08\,\text{Å}$.

The latter was determined from the histogram in Fig. 4.9a. The good agreement between the simulated and actual dissipation maps confirms that small Δz values are almost always associated with a structural hysteresis. Closer inspection of the dissipation maps reveals that dissipation occurs in sickle-shaped semi-circles around O_{carb} atoms. This becomes clear when one considers that lateral tip positions closer towards the centre of the molecule lead to higher lifting of the molecule (Fig. 4.8a). Here the oscillation amplitude is too small to reach z^{b} after the formation of a tip-molecule bond at z^{c}, and thus no measurable dissipation is expected.

4.2.4 Summary and outlook

Here, a novel SPM based method was presented that allows probing of interaction potentials within a closed molecular layer by mechanical manipulation of individual molecules. This method suggests the presence of repulsive intermolecular H-O interactions and confirms a peeling-like manipulation protocol for molecule lifting. The high reproducibility and clarity of the data, and the magnitude of the observed effects regarding bond formation and breaking, makes it a valuable reference to test ab-initio simulations. It also reveals possible binding sites for adatoms which match the tip termination. A major upcoming challenge is the analysis of the entire $\Delta f(x, y, z)$ 3D dataset recorded during the manipulation of the molecule. This method relies only on the presence of a particularly reactive atom in the molecule and that the interactions are able to break an established tip-molecule bond along one specific trajectory (which could be tuned by adjusting the termination of the tip apex), thus it can be used to study a wide range of molecules.

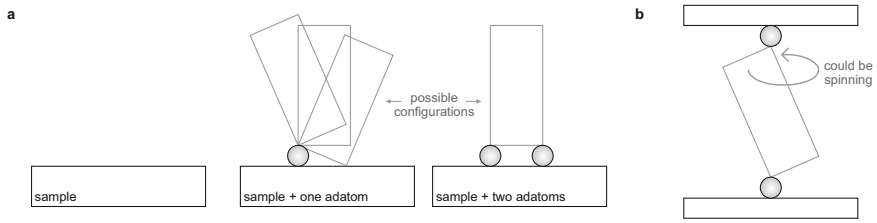

Figure 4.10: Schematics of artificial tips and junction structure a, Schematic of three artificial tips on the surface representing: flat tip, flat tip with a single atom protrusion, flat tip with two single atom protrusions. **b**, Schematic of a symmetric junction. The molecule could be spinning in it. More precisely, it could perform a random walk between fixed angles of rotation.

4.3 Studying the tip-molecule bond by manipulation of molecules attached to artificial tip apexes on the sample surface

4.3.1 Introduction

SPM tips are often decorated with single atoms or molecules to improve their imaging capabilities [55, 56, 57, 58, 38, 53]. The tip-molecule contact for larger molecules is of special interest, because the latter can be used as building blocks for supramolecular structures. In particular, molecules in a vertical configuration (Fig. 4.10a) on the tip facilitate such construction tasks. In this configuration, the bonding to the tip is weaker than a flat adsorption geometry on the tip because it minimises the van der Waals interaction of the molecule with the tip and reduces the overlap of their electronic states. Therefore, breaking of the tip-molecule contact requires less force and increases the chance to leave both, tip and molecule, intact. Further, large parts of the molecule remain free to interact with other building blocks. A clear understanding of the tip-molecule contact, which allows a vertical configuration, is key for engineering supramolecular structures.

Studying the properties of the tip-molecule contact is difficult. The primary tool for investigation, the tip, cannot move independently from the molecule under investigation when the molecule is attached to the tip. However, when a molecule is attached to an artificial tip on the sample surface, studying its properties becomes easier. The attached molecule can be manipulated by the SPM tip and the result can then be investigated afterwards in a conventional SPM imaging experiment. This requires the cleavage of the tip-molecule contact at the end of the manipulation. Fig. 4.10a shows the three simplest artificial tip apexes that can be constructed on the surface.

This section focuses on the characterisation of PTCDA 'standing' vertically on a Ag-terminated tip, a so called s-PTCDA. PTCDA often remains in a vertical configuration on the tip after its detachment from the Ag(111) surface (see section 3.2.3). Reversible contact formation and cleavage of this configuration was successfully demonstrated in a subtractive manufacturing task [21]. s-PTCDA can also be used as a QD for the SQDM method [38].

For the investigations in this section, PTCDA is attached to a Ag adatom mimicking the

tip apex, forming a Ag+PTCDA complex. The properties of the adatom-molecule bond are probed by contacting the molecule on the short side opposite to the attached adatom and retracting the tip along a vertical trajectory. The investigation has two goals:

(1) The first goal is to gain further insight into the mechanical properties of the vertical configuration of s-PTCDA, more precisely, its stabilisation mechanism and the characterisation of the Ag-O bond(s) between the molecule and the tip. In case of bare Ag(111), s-PTCDA cannot be constructed by mechanical manipulation. The tip-molecule contact is stronger than the contact to the surface. Therefore, a gentle cleavage of the tip-molecule bond is not possible. s-PTCDA was successfully constructed on a pedestal of two Ag adatoms on the sample surface (see section 3.2.4). The question arises as to whether one adatom could be sufficient.

(2) Using a single adatom as the surface contact allows the construction of symmetric junctions with VM (Fig. 4.10b). The second goal is to study the dynamics of such junctions. This is interesting, because the PTCDA molecule in the junction is free to rotate around its diagonal axis. The molecule could even be spinning if the junction is perfectly symmetric.

4.3.2 Experiment

After the PTCDA/Ag(111) sample preparation a low coverage of Ag adatoms was additionally deposited in-situ (see section 2.3). To assemble a Ag+PTCDA complex, a single PTCDA molecule was lifted from an island edge and positioned on a clean Ag(111) surface area (see section 3.2.3) in the vicinity of a Ag adatom. Then, the Ag adatom was moved via LM (see section 3.1.2) towards one O_{carb} of the single PTCDA molecule, until the formation of a chemical Ag-O bond between molecule and adatom occurred (Fig. 4.11a).

A second assembly method involved dragging of the molecule across a Ag adatom: The Ag adatom was positioned lower in the slow scan direction than the PTCDA molecule via LM. The PTCDA molecule was lifted into a (nearly) standing configuration and then dragged over the adatom by recording a constant height STM image. The formation of the complex was indicated by an abrupt change in the I signal. If the complex remained in contact with the tip after the recording, the tip was retracted from the surface until the tip-molecule contact ruptured and the molecule fell back towards the surface. (Note that the same assembly method can be used to assemble 2Ag+PTCDA, by using two adatoms instead of one.)

Both methods described above were used to construct Ag+PTCDA.

After recording a 50 Å by 50 Å topography reference image of the Ag+PTCDA complex centred on the Ag adatom, the SPM tip was positioned over a O_{carb} at either position 1 (diagonal) or position 2 (opposite, towards the Ag adatom) and a preprogrammed VM (see section 3.2.3) was executed. The tip was approached towards the surface for 3.7 Å - 4.0 Å and retracted for 20 Å from the setpoint (0.2 nA, 0.35 V). The manipulation is sketched in Fig. 4.11c. During tip retraction, the complex was lifted until the PTCDA molecule stood (nearly) vertical on the Ag adatom. On further tip retraction, the tip-molecule contact ruptured and the complex dropped back towards the surface, potentially in a different orientation than before the manipulation.

While repeating the cycle of recording a reference image and VM, the Ag+PTCDA complex performed a random walk across the Ag(111) surface. The complex was always

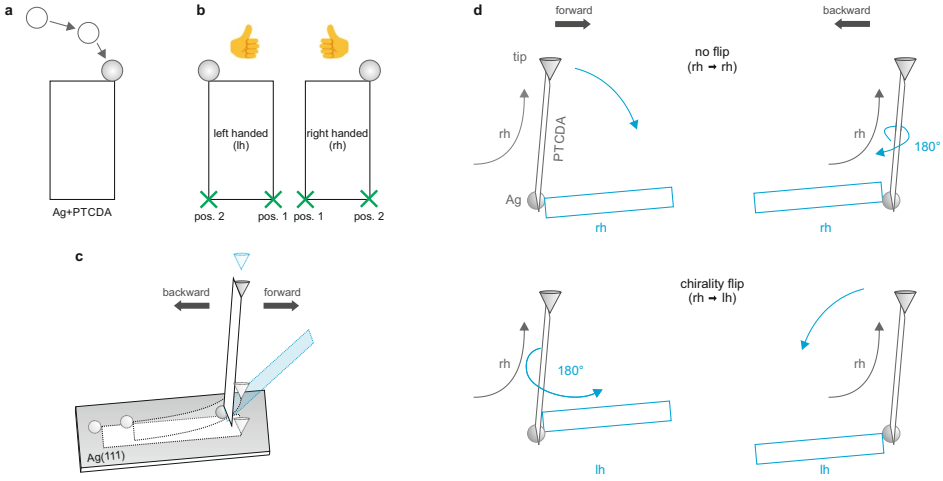

Figure 4.11: Structural properties of Ag+PTCDA on Ag(111) and illustration of the manipulation. **a**, Schematic of the construction of Ag+PTCDA via LM of a Ag adatom. **b**, Chirality and the two contact positions: diagonally opposite (pos. 1) and opposite (pos. 2) to the adatom. **c**, Definition of the molecule falling back to the surface in forward or backward direction. **d**, Schematic of the scenarios whether a chirality flip occurs. The blue parts indicate configurations after the tip-molecule contact rupture in **c** and **d**.

contacted on the O_{carb}-terminated PTCDA side with no attached adatom, leading to the complex moving one PTCDA length towards the tip when lifted (Fig. 4.11c).

The mirror symmetry of a single PTCDA molecule on Ag(111) is broken by the attachment of a Ag adatom. Consequently, the Ag+PTCDA complex has a chirality. Its left- or right-handedness is defined in Fig. 4.11b.

The different drop behaviours of the Ag+PTCDA complex upon tip-molecule contact rupture are sketched in Fig. 4.11d. Two drop behaviours could change the chirality of the complex after the VM: First, the chirality changes when the molecule drops backwards (Fig. 4.11d, lower right). The forward and backward directions are defined in Fig. 4.11c. Second, when the molecule drops forwards but rotates 180°, in the upright position around its long axis, before falling down (Fig. 4.11d, lower left).

4.3.3 Results and discussion

Inspecting the Ag+PTCDA complex after vertical manipulation

An interesting finding from 253 experiments is that the tip-molecule contact ruptured in over 99 % during VM. In only two cases did the PTCDA molecule remain on the tip, leaving the adatom on the surface.

There are two possible explanations for this behaviour: On the one hand, two O_{carb} atoms could remain in contact with the surface while only one O_{carb} is in contact with the

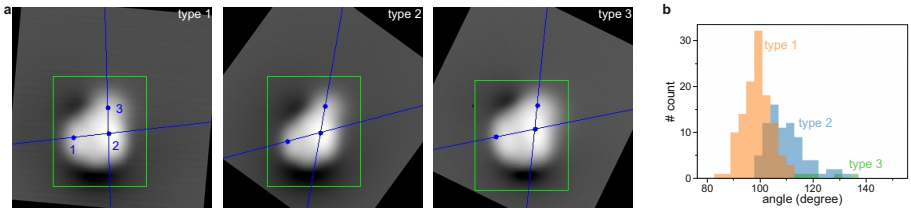

Figure 4.12: Adatom binding geometries for Ag+PTCDA on Ag(111). **a**, STM topography images of geometry types for right-handed complexes. The two blue lines are defined by the three blue dots: (1) centre of left LUMO lobe, (2) brightest spot on right lobe, (3) centre of adatom. **b**, Statistics of adatom binding angles as determined by the angle between the blue lines in **a**.

tip. On the other hand, if only one O_{carb} remains in contact on both sides, then the tip apex must be less undercoordinated than an adatom on the surface. The hand-controlled lifting experiments in section 5.3 reveal that indeed only one O_{carb} remains in contact on both sides. In conclusion, the Ag-O bond between the PTCDA and the Ag adatom is generally stronger than the tip-molecule bond, because the tip apex is apparently less undercoordinated than an adatom on the surface.

The construction of s-PTCDA on a single Ag adatom was unsuccessful. Over 250 attempts via VM were made, but the molecule did either drop back towards the surface or remained on the tip, as discussed above.

Fig. 4.12a shows the three binding geometries for the Ag adatom of the complex found in the experiment. The blue dots were used to characterise the three geometries. The points are defined as follows: (1) centre of left LUMO lobe, (2) brightest spot on right lobe, (3) centre of adatom. The angle measured between the two lines, connecting dot (1) and (2) as well as dot (2) and (3), characterises the angle of the Ag adatom (Fig. 4.12b). The corresponding adsorption types where assigned by visual inspection of the STM image.

A custom program script was written by A. Diener to assist with the analysis of the large dataset. It was written in C++ and the open source library openCV[1] was used to detect the complex in the STM topography images. A graphical user interface allowed the operator to manually correct any errors in the detection: the placement of the three blue dots, the detected geometry type, and the detected angle of the complex orientation on the surface. The green boxes in Fig. 4.12a and Fig. 4.13a indicate the detection of a complex.

Fig. 4.13a,b show the detection and definition of the angle α of the complex orientation. The angle α corresponds to the orientation of the long axis of the molecule. Each STM topography image was processed as shown in the bottom image of Fig. 4.13a. Height thresholds defined the parts where the processed image was filled with: white, black, and grey. To find the angle of a recorded complex, its processed image was rotated anticlockwise until it matched the reference image. A right-handed complex was used as a reference. The reference image was mirrored to determine the orientation of a left-handed complex.

Fig. 4.13c shows the distribution of the recorded orientation angles α of all VM experi-

[1]Link: https://opencv.org/ (retrieved on 29th May 2023)

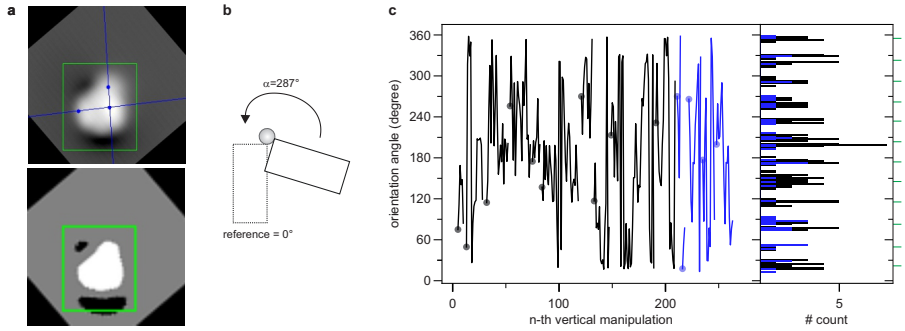

Figure 4.13: Detection and evaluation of the complex orientation. **a**, STM topography image of the Ag+PTCDA complex (top) and the processed version of the image (bottom) for the automated detection of the complex orientation. **b**, The angle α is defined by the number of degrees a recorded orientation has to be rotated in anticlockwise direction to match the reference orientation. **c**, Graph (left) and histogram (right) of the recorded orientations of all VM experiments. The orientations in sequence are connected by a line in the graph. The start of each sequence is marked by a dot. The colour indicates the contact position used for VM: black (position 1), blue (position 2). The centres of the twelve orientation groups in the histogram are marked by green ticks.

ments.

The graph on the left shows the recorded orientations in the order of VM executions. Angles connected by a line belong to one experimental series - the next VM was executed directly after the molecule dropped down. Series which where contacted at position 1 (2) are coloured in black (blue). A series ends when the orientation of the complex is altered by anything other than a VM, or the manipulation experiment cannot be continued. If the Ag+PTCDA complex comes too close to an adsorbate on the surface (because it performs a random walk), the complex is dragged to a free Ag(111) surface area and a new series is started. If the complex is damaged, a new one has to be built to continue the experiment. Interestingly, successive orientations seem to have a bias towards similar orientation angles. This can be seen even more clearly in Fig. 4.14, which shows the distribution of the difference between successive orientation angles $\Delta\alpha$. The trend towards smaller $\Delta\alpha$ ($< 90\,\mathrm{deg}$) will be analysed later to gain further insight into the dynamics of the junction.

The right side of Fig. 4.13c shows a histogram of the number of complexes recorded at specific angles. A similar distribution of angles is found for both contact positions. Interestingly, the angles cluster in twelve groups that are around 30° apart. This clearly indicates the presence of two distinct adsorption sites for the complex, taking the 6-fold symmetry of the Ag(111) surface into account. The two orientations of the complexes with respect to the underlying Ag(111) lattice are similar to the case of isolated PTCDA molecules, which are oriented along the $[1\bar{1}0]$ and $[2\bar{1}1]$ directions [34].

Summarising, the molecule was found to be able to rotate freely around its adatom, as expected. Interestingly, the Ag+PTCDA bond to the surface was found to be stronger than to the SPM tip. The attached Ag adatom adds a chirality to the Ag+PTCDA complex and

was found in three binding geometries to the O_{carb} atom. Two adsorption orientations could be identified for the PTCDA molecule of the complex.

Junction dynamics

As mentioned earlier, the recorded orientations of the Ag+PTCDA complex after successive VM experiments show a bias towards similar orientation angles. Therefore, the difference between two successive orientation angles $\Delta\alpha = \alpha^{after} - \alpha^{before}$ should contain a lot of information about the dynamics of the junction during the manipulation and will be analysed regarding:

1. What is the structure of the junction before the rupture of the tip-molecule contact? Did the junction (adatom, molecule, tip) self-align into a symmetric structure (Fig. 4.10b)?
2. Does the binding site of the adatom jump between the two O_{carb} atoms at the bottom of PTCDA during VM?

The analysis of the junction dynamics focuses mainly on the later part of the VM, where the molecule is (nearly) standing in the junction and the unpaired O_{carb} at the bottom of PTCDA is detached from the Ag(111) surface. Only then can the molecule freely rotate around the axis connecting its Ag adatom and the tip apex (Fig. 4.10b). Note that in the standing configuration, only the initial adsorption orientation of the complex remains relevant, as the latter defined the contact position of the SPM tip. Any influence of the initial binding geometry of the adatom (type 1, 2, 3; Fig. 4.12) is expected to be minor at this point of the manipulation, as the adatom has been dragged through several hollow sites on the Ag(111) lattice, and will be neglected in the following.

Fig. 4.14 shows the distribution of all $\Delta\alpha$ angles. Fig. 4.14a shows a histogram of $\Delta\alpha$ projected to $\pm 180°$. $\Delta\alpha^{\pm 180}$ is defined such that a positive (negative) value corresponds to a clockwise (anticlockwise) rotation of the complex after VM.

$$\Delta\alpha^{\pm 180} = \begin{cases} \Delta\alpha & \text{if } -180° \leq \Delta\alpha \leq +180° \\ \Delta\alpha - 360° & \text{if } \Delta\alpha > +180° \\ \Delta\alpha + 360° & \text{if } \Delta\alpha < -180° \end{cases}$$

The histogram confirms the bias towards smaller rotation angles. The $\Delta\alpha$ angles are also distributed into twelve groups, as expected from the distribution of orientation angles α for the Ag+PTCDA complex.

The bias towards smaller $\Delta\alpha$ provides some clues to the junction structure: First, the PTCDA molecule does *not* spin in the junction. Otherwise, one would expect an even distribution of α and $\Delta\alpha$ across all angles. This also suggests that the adatom and tip apex are not perfectly aligned perpendicular to the surface. Thus, the junction does *not* self-align into a perfectly symmetric structure. Second, the molecule does however rotate in the junction during the VM. Third, the strong bias towards smaller rotation angles means that the molecule tends to drop forward after VM (Fig. 4.11c). This suggests that the rotation axis of the molecule (the axis connecting the adatom and tip apex) would not be

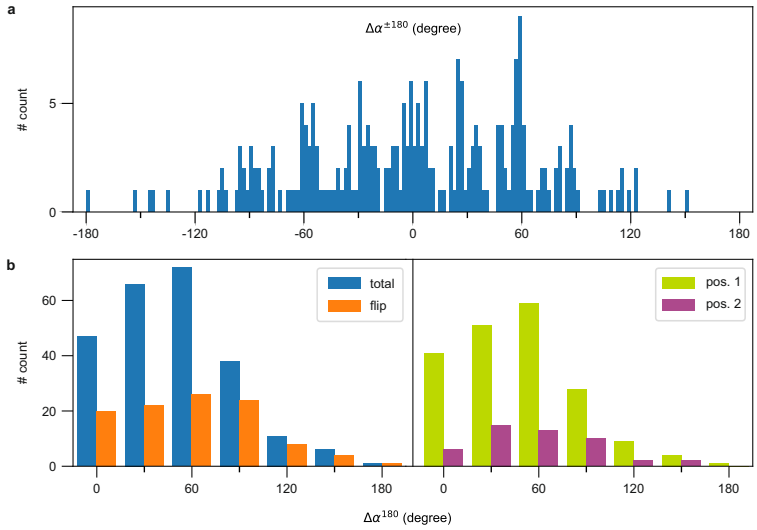

Figure 4.14: Distribution of delta angles before and after the manipulation of the complex. **a**, Histogram of all recorded $\Delta\alpha^{\pm 180}$. The bin width is 2°. **b**, Histograms of the absolute values of the data in **a**. The left histogram compares the total number of lifting experiments to the number of experiments which show a chirality flip. The right histogram compares the experiments contacted diagonal opposite (pos. 1) with the ones contacted opposite (pos. 2) to the Ag adatom. The bin width is 30°.

perpendicular to the surface, but tilted forward towards the tip. Fourth, the unpaired O_{carb} next to the adatom is attracted as close to the surface as possible. If the rotation axis of the molecule is tilted, this is realised at a specific angle, which will be adapted by the molecule.

Fig. 4.15a shows a 3D render of the proposed junction structure for a right-handed molecule contacted at position 1 (diagonally to the adatom). The transparent complex indicates its position before VM, the opaque one during the manipulation. The short axis of the molecule is expected to be oriented forward, in a vertical plane aligned with the adatom and the tip. This allows the smallest distance between the bottom unpaired O_{carb} and the surface (Fig. 4.15b). When the adatom is dragged across the surface along the diagonal of the molecule during VM, the molecule is expected to rotate approximately 69° in anticlockwise direction. Taking the surface corrugation into account, it is likely that the adatom ends up in the closest hollow site along the diagonal to the contacted O_{carb}. Then, the expected rotation is 60° Fig. 4.15c. The rotation would be in clockwise direction for a left-handed complex.

Inspection of the histograms in Fig. 4.14b further confirms the junction model proposed above. The histograms show the distribution of $\Delta\alpha^{180}$ for: the total number of recorded $\Delta\alpha$ (left), chirality-flips (left), and contact position 1 and 2 (right). For clearer binning, $\Delta\alpha$ was projected to 180° and a bin width of 30° was used. As predicted by the model, the orientation of most complexes changes by 60° after VM. Note, that the majority of complexes

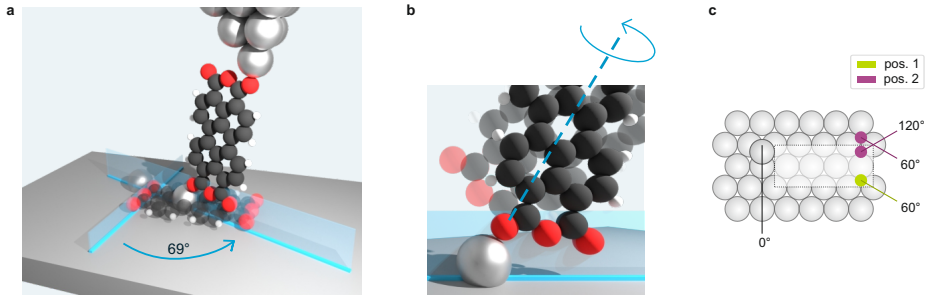

Figure 4.15: Model of the junction during vertical manipulation. **a**, Sketch of the anticlockwise rotation of PTCDA during lifting for a right-handed complex. The molecule is expected to rotate around 69°, if the Ag adatom moves along the diagonal of PTCDA during lifting in the absence of surface corrugation. The blue walls indicate the orientation of the oxygen atoms before and during the VM. **b**, Sketch of the closest (opaque molecule) and furthest (transparent molecule) distance between the unpaired O_{carb} at the bottom of PTCDA and the surface. The dashed line indicates the rotation axis along the diagonal of PTCDA. The opaque molecule has the same orientation as in **a**. **c**, Sketch of predicted $\Delta\alpha$ if the adatom ends up in the closest hollow site to the tip during VM. The expected adatom position and orientation of the short axis of the molecule are indicated in green (purple) for contact position 1 (2). Two adatom sites are indicated for contact position 2, because the distribution of $\Delta\alpha$ shows a bias to $\Delta\alpha < 90°$.

were contacted at position 1.

No chirality flip is expected for a forward falling molecule and a chirality flip for a backward falling molecule, because a rotation around 180° during the fall is unlikely due to the tilted rotation axis (Fig. 4.11d). The general trend is in line with this expectation, showing a smaller fraction of chirality-flips for $\Delta\alpha^{180} < 90°$ and a larger fraction for $\Delta\alpha^{180} > 90°$. However, the presence (absence) of chirality flips in some cases for $\Delta\alpha^{180} < 90°$ ($> 90°$) indicates that there is at least one additional mechanism that changes the chirality of the complex and will be discussed later.

For contact position 2, the junction model described above would predict a rotation of the molecule of around 90° if the surface corrugation is neglected. If the adatom were to end up in the closest hollow site to the contacted O_{carb}, the model would predict a rotation of around 120°. However, the distribution of $\Delta\alpha^{180}$ is similar when contacting the complex at position 1 or 2 (Fig. 4.14b, right histogram). For position 1, most molecules rotate around 60°, as expected. For position 2, the bins for 30° and 60° are similar in height, with the former being slightly higher. For contact position 2, the adatom and the tip are on the same side (along the long axis) of the molecule. This could lead to the unpaired O_{carb} at the bottom of PTCDA to be closer to the surface compared to the case of contacting at position 1. Therefore, the unpaired O_{carb} could still be influenced by the surface corrugation at the tip-molecule contact rupture, which would hinder the rotation and lead to a smaller $\Delta\alpha$.

Indeed, when comparing the median curves extracted from the VM curves of the complex for contact position 1 and 2 (Fig. 4.16), the tip-molecule contact ruptures at a lower height for contact position 2 than for 1 by around 0.4 Å. This suggests that the unpaired O_{carb} is

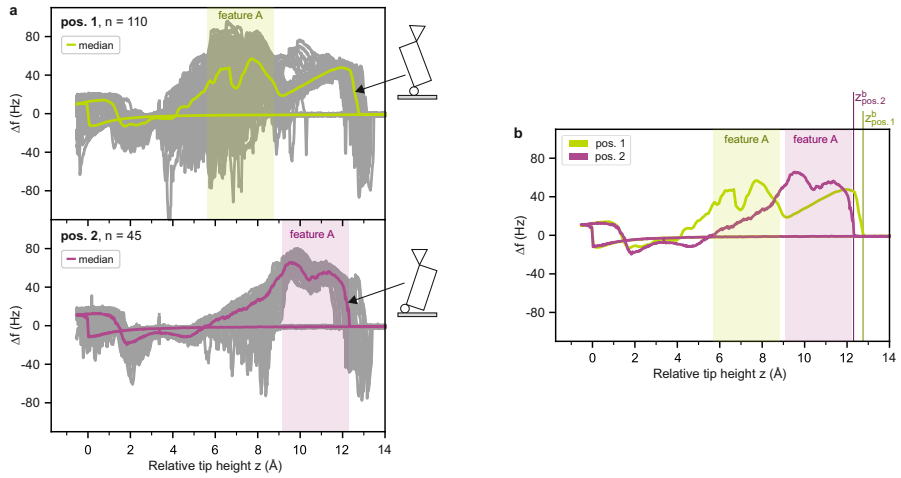

Figure 4.16: Comparison of VM of complex for contact position 1 and 2. **a**, Δf signals for both contact positions. The VM curves are coloured in grey and the corresponding median curves are coloured in green (position 1, diagonal opposite) and purple (position 2, opposite). The double peak feature (feature A) is indicated in the colour of the corresponding median curve. The sketches to the right of **a** indicate the expected junction configuration before tip-molecule contact breaking for both contact positions. The median curves were calculated by taking the median of all recorded Δf values at each z position of the corresponding VM curves. The number of VM curves used in calculating the corresponding median curves is indicated by n. $z = 0\,\text{Å}$ corresponds to the contact formation of the median curves. Any VM curves with loss of Δf tracking were removed. Only around half of the VM curves for position 1 are shown, because the first half was recorded with different manipulation settings to position 2, e.g. faster manipulation speed. **b**, Median curves from **a**. The tip-molecule contact breaking heights $z^b_{\text{pos. 1}}$ and $z^b_{\text{pos. 2}}$ for both contact positions are indicated by a vertical line. For more information see text.

being closer to the surface for contact position 2. Moreover, the double peak feature (feature A) is shifted to the end of the manipulation for position 2. Feature A is analysed in detailed in section 5.3. The right flanks of each peak of feature A are linked to the separation of one of the two unpaired O_{carb} atoms (O_{carb} *not* bound to the adatom or the tip-apex atom) of PTCDA. The first peak closer to the surface indicates separation of the unpaired O_{carb} from the tip and the second one separation from the surface. That the tip-molecule contact ruptures in the right flank of the second peak for contact position 2 strongly indicates that the bottom O_{carb} is still in contact with the surface at the end of the manipulation.

The prominence of $\Delta\alpha^{180}$ around 60° (Fig. 4.14b) could be explained by the junction model (Fig. 4.15) in the above analysis. However, the model additionally predicts a distinct rotation direction of the complex depending on its chirality. This is studied by analysing $\Delta\alpha$ in dependence of its rotation direction and the chirality of the complex.

The histograms in Fig. 4.17 show the distribution of $\Delta\alpha^{\pm 180}$ in dependence of the chirality of the complex. $\Delta\alpha^{\pm 180}$ is analysed in two ways: In Fig. 4.17a the chirality of the complex is assigned at the start of the VM experiment and in Fig. 4.17b after the experiment. If a

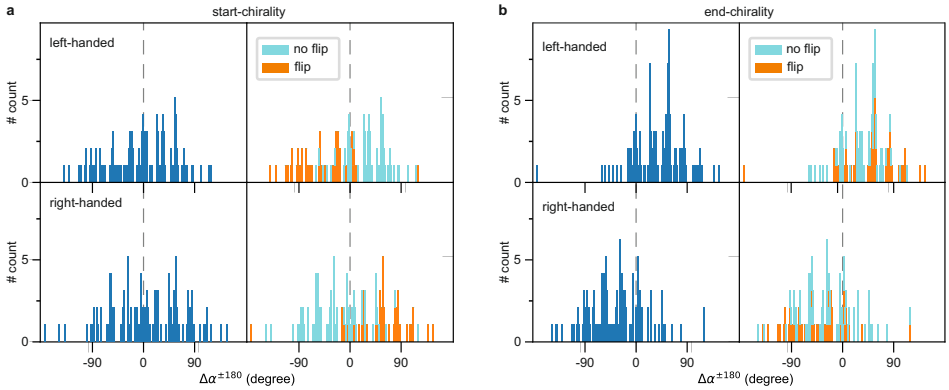

Figure 4.17: Histograms showing the rotation of the complex due to VM in dependants of the chirality. The chirality of the complex is assigned at two points in time: before (**a**) and after (**b**) the VM. On the left side of **a** and **b** the histograms show the total number of recorded $\Delta\alpha^{\pm 180}$. On the right, each bin from the left is subdivided into the number of experiments where the chirality of the complex remained the same before and after the VM (no flip, light blue) and where the chirality flipped (flip, orange). The bin width is 2°

complex is left-handed at the beginning and right-handed after the VM, then it would be labelled as left-handed in Fig. 4.17a and right-handed in Fig. 4.17b. In addition, the $\Delta\alpha^{\pm 180}$ data would be labelled as flipped in both figures.

Inspection of Fig. 4.17 reveals: First, the start-chirality does not allow prediction of the rotation direction of the molecule in the junction, as $\Delta\alpha^{\pm 180}$ shows an equal distribution for clockwise and anticlockwise rotations. This is puzzling at first, because the model predicts a clear preference for the rotation direction of a right- or left-handed complex. Interestingly, the rotation direction is as expected for most complexes that keep their chirality after VM. Mainly the complexes showing a chirality flip after VM rotate in the opposite direction. Second, evaluation of $\Delta\alpha^{\pm 180}$ in dependants of the end-chirality clearly shows the expected bias for left-handed (right-handed) complexes to rotate clockwise (anticlockwise).

There are two mechanisms that could change the chirality of the complex during VM in addition to falling forwards or backwards: First, the adatom is dragged across the surface during VM (Fig. 4.11c). This, combined with the surface corrugation, could lead to the adatom to jump to its neighbouring O_{carb}. Second, the Ag adatom could potentially jump to its neighbouring O_{carb} position due to a thermal annealing of the PTCDA molecule after the rupture of the tip-molecule bond. On the one hand, the energy gain due to the tip-molecule bond formation was 0.6 eV according to *ab initio* simulations [16]. This energy is stored in the deformation of the molecule and tip apex when rupture of the tip-molecule contact occurs. On the other hand, the kinetic energy of the molecule is increased by the energy gain on adsorption. The adsorption energy of PTCDA/Ag(111) is estimated to be between 2 eV - 3 eV [59].

The observations of Fig. 4.17 are in favour for the first mechanism, where the adatom

jumps to the neighbouring O_{carb} while being dragged across the surface during VM. The strong correlation of the rotation direction with the end-chirality reveals that the chirality just before tip-molecule contact rupture is identical to the chirality found after the VM experiment. Thus, a random change in chirality due to a thermal annealing affect can be ruled out (or is at least negligible).

Summarising, the following junction model could be derived: VM of a Ag+PTCDA complex leads to a nearly symmetric junction where the rotation axis of the molecule (axis connecting the adatom and tip apex) is slightly tilted forwards. The short axis of the molecule wants to align itself with the adatom and tip apex to minimise the distance between the unpaired O_{carb} at the bottom of PTCDA and the surface. This leads to a clockwise (anticlockwise) rotation for a left-handed (right-handed) complex. It is likely that the adatom ends up in the closest hollow site to the tip during VM. For contact position 1, this would lead to a rotation of 60° and is consistent with the data. For contact position 2, the picture is less clear. It appears that there are additional effects that are not captured by the junction model. It could be shown that the bottom unpaired O_{carb} is still in contact with the surface upon tip-molecule contact rupture. Therefore, the O_{carb} is subjected to the surface corrugation while the molecule rotates in the junction during VM, resulting in a reduction in $\Delta\alpha$ compared to contact position 1. With regards to the mobility of the Ag adatom, it is possible for it to jump between the two neighbouring O_{carb} during the lifting of the molecule from the surface. An adatom jump due to a thermal annealing effect after tip-molecule contact rupture could be excluded.

4.3.4 Summary and outlook

The tip-molecule contact plays an important role in the construction of supramolecular structures. By attaching molecules to artificial tip apexes on the surface this contact can be investigated by molecular manipulation. With the help of an artificial tip apex in the form of an Ag adatom, it was possible to construct a molecular junction with symmetric contacts (Ag adatom, PTCDA, tip apex atom) and reaching a nearly symmetric junction geometry during VM.

It was shown that the molecule can freely rotate in this junction around the axis defined by the two contacts. Further, it was demonstrated that the bottom unpaired O_{carb} is attracted to the surface which leads to the molecule rotating in clockwise or anticlockwise direction, depending on the chirality of the Ag+PTCDA complex, to minimize the distance between the O_{carb} and the surface.

The attraction of the unpaired O_{carb} to the surface makes it likely that in the case of s-PTCDA on the tip *both* O_{carb} from an Ag-O bond with the tip. This is also supported by a recent DFT calculation of the stabilisation potential for s-PTCDA on different tips [39].

For future experiments, it would be interesting to study s-PTCDA on larger artificial tip apexes than two adatoms as this should increase its stability. The DFT calculations [37, 39] indicate that the role of the adatoms is mainly to act as a spacer to weaken the destabilising vdW interaction between the molecule and the surface. The lager the spacer (or the higher the artificial tip apex) the more stable the s-PTCDA. One could for example provide two defined contacts on the surface in the form of a single adatom and a 4-adatom-cluster. For

the cluster, the three adatoms in the bottom layer could be assembled by LM and the adatom in the top layer could be deposited from the tip (by gently approaching the centre of the cluster at low V_{bias}). It would be interesting to confirm that the s-PTCDA would be more stable standing on these two unequal artificial tips than on two adatoms. Further, since STM tips are expected to be imperfect and don't have a perfectly symmetrical structure around the tip apex, this would improve our understanding of s-PTCDA on the STM tip.

CHAPTER 5

Application of hand-controlled three-dimensional manipulation

5.1 Overview

Manual two-contact manipulation in 3D is a laborious task and is clearly limited to small systems. For the construction of more complex nanoscale objects or patterning of larger molecular structures, as demonstrated in the subtractive manufacturing of "Jülich" by removing 48 molecules [21], an *autonomous* approach would be preferred.

However, in order to delegate a task to a robot, we first need to do it ourselves to gain an intuition of how it works and to understand the challenges involved. This approach is also used in macroscale robotics with industrial robots, where a human teacher manually guides the robot's manipulator along the desired path by hand.

Our intuition can be improved by accessing the molecular junction through direct *manual* control of the manipulator. This gives the experimenter immediate feedback on the junction's response to an action and allows experience to be accumulated.

This chapter presents a further development of HCM using the game engine Unity™ (see section 5.2) and utilizing HCM to increase the reproducibility between two-contact manipulation experiments (see section 5.3). As intuition improves (initially for specific manipulation goals), it will become easier to implement autonomous manipulation routines (see chapter 6).

5.2 Professionalisation of hand-controlled manipulation software

5.2.1 Introduction

With the successful demonstration of a prototypical application for HCM [21, 40] (see section 3.3), the focus shifts from fast development and execution of the method to transforming it into a tool that becomes a long-term asset. This requires the program code to be restructured in terms of: readability, maintainability, and extensibility. By rebuilding the application in a game engine (a framework for game development), not only is one supported to write modular code but also synergy effects from modern game development can be incorporated - namely a 3D editor and built-in support for many currently available VR goggles.

Sections 5.2.2 to 5.2.3 cover rebuilding the application in the Unity™ game engine, discussing the advantages and disadvantages of a game engine, and integrating new features. Chapter A presents a quick start guide that provides an overview of the application's graphical user interface (GUI) in Unity™ and covers all the necessary steps required to get started with HCM. Section 5.3 shows a successful demonstration of reproducible two-contact manipulation (see section 3.2) of a single Ag+PTCDA complex on Ag(111), supported by new features of the HCM Unity™ version.

5.2.2 Implementation in Unity

The VR interface of the HCM C++ version was written as a single code file, without a clean separation of the code responsible for the rendering and the program logic. Due to the development over time, the HCM application ended up being fragmented into different scripts (Fig. 3.5b).

Fig. 5.1 shows the data flow for the new HCM version 'HandCtrl' written in Unity™ (see section 2.3 for analogue connections). Now all the necessary functionality for a HCM experiment is integrated into a single application: receiving the position of the tracked object (MCS) and applying it to the SPM tip (RVS), recording of the experimental data (ADC), and rendering a 3D scene for visual augmentation including the tip position and the colour-coded trajectories. Also, the simulation is now an additional feature and not part of the direct communication between the MCS and HandCtrl.

Rewriting the application in the Unity™ game engine has many additional benefits beyond restructuring the source code: First, the game engine is free of charge for non-commercial applications. Second, the structure of Unity™ supports the developer to use object orientated programming. Everything that is part of the VR environment (the 'scene' in Unity™ terms) has to be either a so called 'GameObject' or it has to be attached to one. This enforces a separation between the visualisation and the program logic defined by scripts. Scripts that interact with a GameObject, such as the virtual SPM tip, are directly attached to that object. This also keeps the scripts organised and easy to find. The quick start guide, for the HCM Unity™ version in chapter A, shows an example for the GameObject 'Tip' (Fig. A.6) and the GameObject 'Oscilloscope' (Fig. A.7). Third, Unity™ supports many

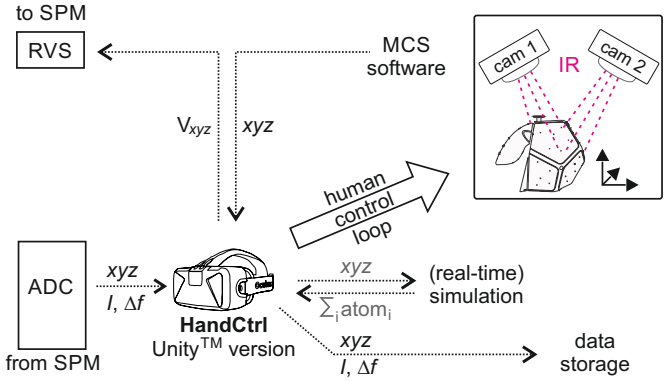

Figure 5.1: Schematic of HCM setup with HandCtrl (Unity™ version). Only the digital connections are shown. A Vicon™ motion capture system (MCS) and Oculus™ VR goggles are used for HCM.

VR systems. It provides native support for: Oculus™, OpenVR™, PlayStation VR™, Gear VR™.[1] No additional code is required to adapt the rendering of the scene to the specific VR goggles used. Therefore, by using a game engine, one can benefit from future developments of the VR gaming industry with little or no additional effort to integrate them. These could be: higher resolution VR goggles, VR controllers, improved spatial tracking of controllers and goggles. Fourth, building the scene and interface in a WYSIWYG (what you see is what you get) 3D editor is much easier than having to compile the application to see the changes (as with the previous version). Fifth, Unity™ allows the user to modify scene elements and (public) variables of the attached scripts during the execution (runtime) of the application. This greatly simplifies the implementation of a GUI. It also reduces the effort to extend the functionality of HandCtrl in the future.

There are also some noteworthy drawbacks to using a game engine. The developed application is strongly dependent on a third party program (Unity™). Another drawback is that C++ is not (directly) supported for writing scripts in Unity™. The closest supported language is C#. Therefore, none of the code from VR interface (C++), including the code responsible for communicating with the ADC device, can be reused and had to be rewritten. The MCS interface (C#) however can be reused, at least the RVS part. The MCS part was also rewritten. The MCS software Vicon Tracker™ runs a VRPN (virtual reality peripheral network) server that can be accessed from Unity™. VRPN was chosen because it allows the implementation of a cleaner interface. This interface could also be used by other devices (controllers) supporting VRPN.

Clearly, the advantages of using a game engine for HCM development outweigh the disadvantages. The main benefits are: support for state-of-the-art VR goggles, greatly reduced effort to create (and extend) a GUI and visual guides. The value of a GUI should not be

[1]Link: https://docs.unity3d.com/540/Documentation/Manual/VirtualReality.html (retrieved on 29th May 2023)

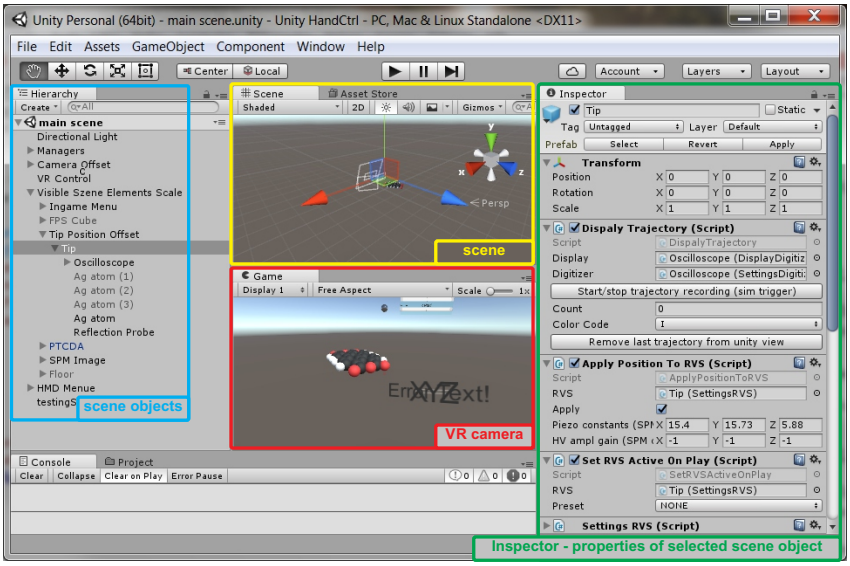

Figure 5.2: Screenshot of HandCtrl in Unity™ editor. The important windows for operating HandCtrl are highlighted by coloured rectangles: Hierarchy (blue), Scene (yellow), Game (red), Inspector (green).

underestimated. It enables the experimenter to get a quick overview of all the settings and their associated values, as well as to modify those values, e.g. the expected piezo constants or the selected RVS hardware. Without a GUI, these values would be hard-coded into the source code, and the experimenter would have to read the code to access them. The HandCtrl application thus becomes more accessible with the addition of a GUI. An additional benefit of HandCtrl is the integration of the Vicon Apex™ (Fig. A.1), which is part of the MCS. The Vicon Apex™ is a handheld device that allows for the tracking of hand movements and also permits user input via buttons. This eliminates the need for the experimenter to sit in front of a keyboard during HCM.

5.2.3 HandCtrl - Program features

Fig. 5.2 shows the perspective of the HandCtrl application as seen by the experimenter on the desktop. The most important elements are: 'Hierarchy' window (blue), 'Scene' window (yellow), 'Game' window (red), and 'Inspector' window (green). To run the application, the experimenter clicks on the 'Play' button (top centre).

As a game engine, Unity™ provides a 3D editor for placing so called 'GameObjects' in a 3D scene and attaching scripts containing the game logic to them. In the 'Inspector' window all public variables of such scripts can be modified and their changes will be saved. Additionally, Unity™ allows to playtest a scene within the editor by clicking the 'Play'

button. After focusing the 'Game' window (by clicking on it), the developer can control its movement in the VR scene as defined in the script 'Player Controller'. The scene in the 'Game' window is also transferred to the connected VR goggles and the viewport in the 'Game' window changes according to the orientation of the goggles. During 'play' mode, all public variables of the scripts can also be modified in the 'Inspector' window. Scene elements and the 'player' can still be freely arranged using the 'Scene' window. However, any changes will be discarded after exiting 'play' mode. This allows the realisation of a menu where the experimenter can simply select a specific functionality on the computer screen at runtime (when using the Unity™ editor to run the program). The menu also organises the provided features and serves as their documentation. Therefore, in the following, changes in the 'menu' will refer to changes of the settings in the 'Inspector' window. Note that the menu is only visible in the editor, not in the VR goggles.

SPM tip control

As in the C++ version, the movement of a special tracked object (e.g. Vicon Apex™) is converted to tip displacement.

The buttons on the Vicon Apex™ are now supported. By pressing the corresponding buttons the experimenter can now start (or stop) the recording of a trajectory, start (or pause) tracking of the xyz coordinates, and select either only the z coordinate or all xyz coordinates for tracking (see chapter A). Therefore, the experimenter is not longer tied to a keyboard anymore and can freely position himself in the area tracked by the Vicon™ system (MCS).

Augmentation

As with C++ version, the executed trajectories of the current HCM session are displayed and colour coded with either I or Δf. Their real-time signals are displayed on a panel next to the virtual tip. A PTCDA molecule acts as a ruler and a reference trajectory is also displayed.

The Unity™ version offers many new visual guides to the experimenter. These are listed below:

First, the displayed scene is 'nicer to the eye' due to, for example: a higher frame rate, a better designed real-time data panel, a less distracting virtual environment. In particular, shadows are now rendered, which improves 3D perception and therefore control of the position of the tip relative to the molecule in the virtual scene.

Second, a head up display (HUD) informs the experimenter if tracking is on (or off) and which coordinates (z or xyz) are currently being tracked (Fig. 5.3).

Third, the real-time data panel does not just display two coloured bars indicating the values for I and Δf. The bars are named and their scaling factor is displayed. The latter can be adjusted in the menu (Fig. A.7).

Fourth, the visual guides in the VR environment acting as rulers during HCM were improved and new features added. A recorded SPM image, e.g. of a PTCDA island, can be loaded and displayed in the VR environment, by selection the appropriate function from the

menu. All channels recorded by the SPM software are detected and available in the menu. This simplifies the alignment of the virtual PTCDA with the real molecule in the experiment. Its rotation can now also be adjusted directly in the menu. Loading of a reference trajectory is no longer limited to a single predefined trajectory. Any previously recorded trajectory can be loaded and used as a reference. Entire sessions can also be loaded for 3D viewing of the recorded data. Unity™ provides simple 3D shapes, which could also be used as visual guides during HCM. For example, a sphere-like shape was quickly created by using the functions of the Unity™ editor and served as a visual guide for reproducible manipulation of a Ag+PTCDA complex (see section 5.3).

Data storage

As with the C++ version, all recorded manipulation trajectories are automatically saved in separate files. Additionally, recorded trajectories beyond the current HCM session and recorded SPM images can be loaded from the data storage as described in the section above.

5.3 Controlling single-molecule junction conductance by a custom manipulation trajectory

5.3.1 Introduction

The characterisation of charge transport through a single molecule remains challenging, due to the lack of fully reproducible experimental results.

The measured transport is highly susceptible to the placement of the electrodes on the molecule and cannot be controlled in MCBJ [6]. Further, the atomic shape of the electrodes of a MCBJ cannot be controlled.

Using an SPM, the clean substrate surface provides one electrode, while the second electrode provides a defined tip-molecule contact made by approaching the molecule at a specific binding site with the SPM tip. After contacting the molecule and retracting the tip on a vertical trajectory from the surface, the molecule-surface contact unfortunately keeps changing its configuration as the molecule slides on the substrate and performs random jumps due to the surface corrugation.

One solution is to fixate the lower end of the molecule on the surface by surrounding it with other molecules. This prevents the molecule from sliding on the surface during manipulation and has been successfully demonstrated for repeated lifting of a molecule in a PTCDA/Ag(111) monolayer [40]. A drawback of this method is the complex junction structure.

In the method presented here, the complexity is reduced by anchoring PTCDA to a Ag adatom instead, thus using a Ag+PTCDA complex on a Ag(111) surface for transport characterisation. The Ag adatom of the complex has two functions: First, it acts as an anchor point for the molecule on the surface. Second, the substrate surface becomes (ideally) a single atom electrode due to the bond between the Ag adatom and PTCDA.

Reproducible charge transport during manipulation of the molecule is achieve, by choosing a (quarter) circle-like trajectory for hand-controlled manipulation (HCM), with the radius around the diagonal length of the complex (see Fig. 5.4). This reduces the likelihood of a random adatom jump during the manipulation.

The experimental procedure is as follows: Starting from the vertical molecule in a stretched (almost 'standing') configuration, the tip descends along a circular trajectory towards the surface and returns to the starting point. This procedure is repeated multiple times to generate statistics.

5.3.2 Experiment

The same sample as in section 4.3 was used for the experiment. After the deposition of PTCDA on Ag(111), Ag adatoms were deposited in situ by thermal evaporation into the SPM. The Ag+PTCDA complex was assembled as described in section 4.3.

The HCM method (see sections 3.3 and 5.2) was chosen for its versatility in performing custom manipulation trajectories. HCM was set up according to the quick start guide in chapter A. The conductance was measured using the lock-in technique, by modulating the

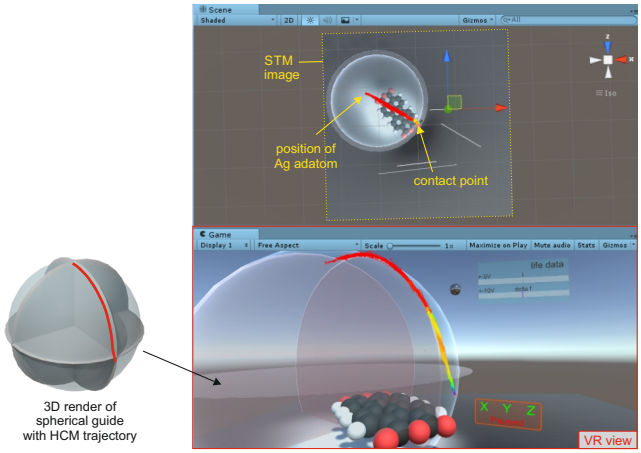

Figure 5.3: Screenshot of experiment using HCM Unity™ version. The bottom window, highlighted in red, shows the view seen by the experimenter while wearing VR goggles. The trajectories display the colour coded conductance signal, from red (low values) to purple (high values).

applied $V_{\mathrm{bias}} \approx 0\,\mathrm{mV}$ by $\pm 4\,\mathrm{mV}$. Two synchronised lock-in devices with different sensitivity settings (0.1 V and 1 V) were used to cover the entire conductance range with high precision.

The signals are sampled at 1 kHz during HCM. This results in large file sizes for trajectories and redundant data (e.g. if the operator pauses the hand movement during HCM). Therefore, the data of each trajectory is compressed by averaging over successive samples with the same xyz tip position, which reduces noise and simplifies the analysis of the recorded signals.

Before using HCM on the assembled Ag+PTCDA complex, the VR environment had to be modified to provide optimal visual guidance during the HCM experiment: First, a STM topography image of the complex was loaded into the VR environment. The image was positioned such that the 'target' $\mathrm{O_{carb}}$ intended for contact was aligned with the $\mathrm{O_{carb}}$ of the virtual PTCDA, with the latter at $xyz = (0, 0, 0)$. The virtual PTCDA was then rotated to match the orientation of the complex (Fig. 5.3). Second, additional to the HCM setup description in chapter A, a visual guide was placed with its centre over the Ag adatom of the Ag+PTCDA complex of the STM image, consisting of a sphere and three planes (Fig. 5.3). This visual guide will be referred to as 'spherical guide' in this section. The spherical guide was expanded, until the centre of the virtual target $\mathrm{O_{carb}}$ of the PTCDA is cut by the sphere (the contact point). The radius was then reduced by about 1 Å, to reduce the lateral forces on the Ag adatom during the manipulation experiment. Then, the spherical guide was rotated to align one of the two planes perpendicular to the sample surface with the diagonal of the molecule, along the Ag adatom and $\mathrm{O_{carb}}$. The intersection line of the plane with the sphere was used as a visual guide during HCM.

The SPM software was used to position the SPM tip over the $\mathrm{O_{carb}}$ diagonal opposite of

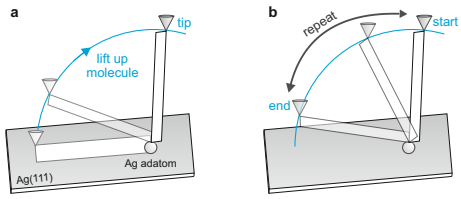

Figure 5.4: Schematic of Ag+PTCDA manipulation procedure. **a**, Contacting and lifting of Ag+PTCDA complex in stretched configuration. **b**, Repeated manipulation of complex on circle like trajectory. The start point is the last configuration in **a**, while the end point is close to the Ag(111) surface.

the Ag adatom attached to the PTCDA molecule. Then, SPM feedback was turned off and the experimenter switched to HCM. To contact the Ag+PTCDA complex, the experimenter made a descending hand movement until a sudden increase in the current was detected, indicating the formation of a Ag-O tip-molecule. To ensure the correct lateral position of the SPM tip during contact formation, only the direction of the hand movement perpendicular to the surface (z direction) was tracked.

After contact formation, all tracking directions were enabled and data recording was started. The experimenter moved the SPM tip away from the surface, following the line of intersection between the plane and the sphere, until the tip was above the Ag adatom of the Ag+PTCDA complex (Fig. 5.4a).

To calibrate the z position of the spherical guide, the SPM tip is further retracted from the surface (only z tracking active), until the tip-molecule bond ruptures and the molecule drops back towards the surface. The spherical guide was now placed 0.5 Å - 1.0 Å below the rupture point, to maximise the self-alignment of the junction while reducing the risk of an unintended bond rupture. Because the molecule drops back to the surface in an arbitrary configuration, the previous steps, including alignment of the virtual PTCDA molecule and the lateral positioning of the spherical guide on the Ag adatom, have to be repeated.

After contacting the complex once more, it was again manipulated along the intersection line on the spherical guide until the start configuration (Fig. 5.4b) for the manipulation experiment was reached - with the tip at the top of the spherical guide over the Ag adatom. Now, the complex was repeatedly manipulated along the previous lifting trajectory, probing the effect of the molecule-surface interaction on the conductance, including the overlap of the π-orbital of PTCDA with the metallic surface states (Fig. 5.3).

5.3.3 Results and discussion

Lifting of the complex along a circular trajectory

Fig. 5.5 shows the highly reproducible conductance and Δf signals of 45 HCM trajectories along a spherical guide for a Ag+PTCDA complex. The combination of the Ag adatom anchor and a circular trajectory seems to successfully suppress random jumps of the molecule

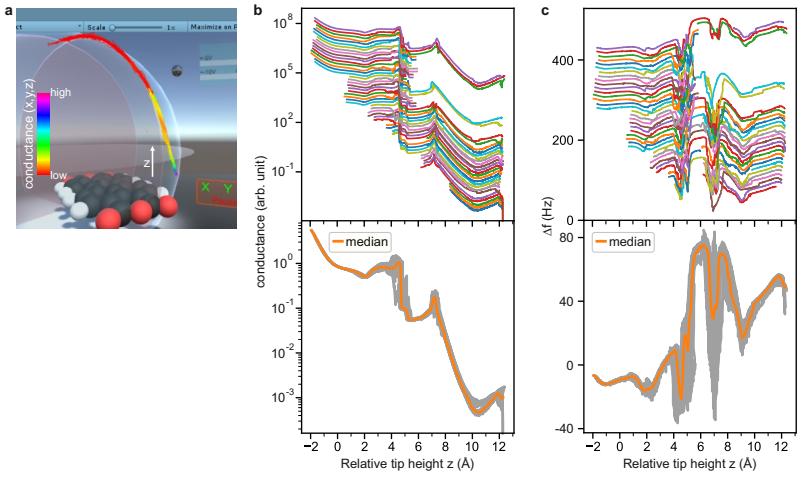

Figure 5.5: Recorded conductance and Δf signals during HCM of a Ag+PTCDA complex along a circular trajectory on Ag(111). **a**, Screenshot of experiment (Unity™ editor). The trajectories display the colour coded conductance(x, y, z), from red (low values) to purple (high values). The z direction is indicated as a white arrow. **b**, Conductance signal corresponding to **a**. **c**, Δf signal corresponding to **a**. In **b** and **c**, the upper panel shows a waterfall plot. In **b**, the curves are offset by scaling them according to $y_i = y_i \cdot 1.5^{i-1}$. In **c**, consecutive curves are offset by 10 Hz. The lower panel in **b** and **c** shows the recorded curves (grey) and the corresponding median curve (orange). The tip height $z = 0$ Å corresponds to the bond formation between the tip and the Ag+PTCDA complex.

due to the surface corrugation during manipulation.

Fig. 5.5a shows the colour-coded HCM manipulation trajectories. Fig. 5.5b,c show each a waterfall plot and the raw curves overlaid with a median curve for the conductance(z) and $\Delta f(z)$ signals respectively. The median curve was calculated by taking the median value at each z height.

The sharp drop in conductance around 12 Å indicates a rupture of the tip-complex bond. This is interesting because the upright, diagonally stretched complex remained standing in the junction (all curves were recorded in direct succession without the need to recontact a dropped complex). With the tip in its vicinity, the standing complex remains seemingly stable due to attractive long range tip-complex forces [37].

Note that some of the trajectories in Fig. 5.5 sample only a part of the z range in Fig. 5.5. Also, the Δf tracking was sometimes lost at sharp Δf jumps. These parts were removed from the Δf curves shown in Fig. 5.5c. The conductance curves are unmodified.

Compare reproducibility of HCM vs. VM of complex

This section analyses the improvement in reproducibility of the HCM along a circular trajectory compared to the VM of a complex.

The VM curves are taken from the recorded data from section 4.3, where the tip-complex

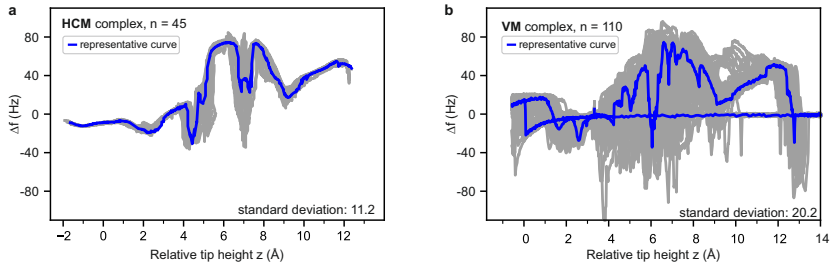

Figure 5.6: Frequency shift curves for HCM and VM of the complex. The representative curve is blue and all other curves are grey for the respective dataset. n corresponds to the number of trajectories in each dataset. **a**, HCM along a circular trajectory. **b**, VM. For more information see text.

bond was established diagonally opposite to the Ag adatom. After contact formation, the tip was retracted 24 Å from the surface. Because the bond to the adatom on the surface is stronger than the tip-molecule bond, the bond to the tip ruptures at a specific height and the complex had to be contacted again for the next manipulation.

A high level of control over the complex configuration during the manipulation results in reproducible conductance curves. Therefore, the reproducibility of the Δf curves will be analysed.

The DTW algorithm [60, 61] is used to find the manipulation curve that best represents the respective dataset for HCM and VM of the complex. DTW computes a distance measure between two curves. The distance is zero for identical curves. The advantage of DTW is the robustness of the distance measure against scaling of one of the two input curves along the x-axis, as well as a shift along x.

The manipulation curve with the lowest sum of the DTW distances to all other curves will be referred to as the representative curve for the respective dataset. For the HCM data, only trajectories with a z range greater than 9 Å and without loss of Δf tracking were compared. For the VM data, only the retracting part of the Δf curve up to $z = 14$ Å is used to calculate the DTW distance.

Fig. 5.6 shows the manipulation curves for HCM (Fig. 5.6a) and VM (Fig. 5.6b). The representative curve is coloured in blue. All other curves are coloured in grey.

The ”standard deviation” from the representative curve is chosen as measure for the reproducibility. It is defined similarly to the standard deviation around a mean value, except that the deviations are not calculated from a fixed mean value, but from the Δf value of the representative curve for each z height.

The standard deviation defined here is 11.2 for HCM and 20.2 for VM. This shows, that the circular trajectory substantially improves the reproducibility by reducing the influence of the surface corrugation. Note that only the retraction part up to $z = 14$ Å is taken into account when calculating the standard deviation for VM.

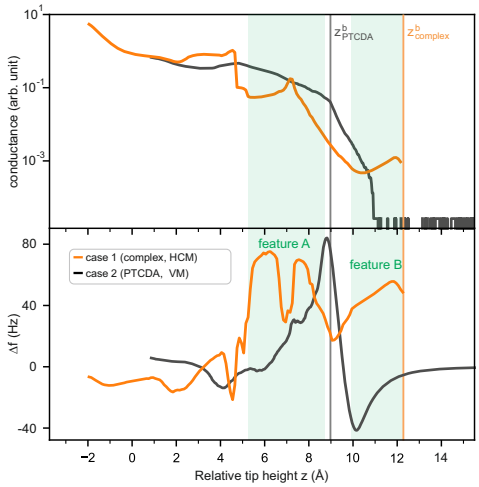

Figure 5.7: Median curves of recorded conductance and Δf signals for Ag+PTCDA (HCM) and PTCDA (VM). Two vertical lines (PTCDA: grey, complex: orange) indicate the height z^{b}, where the bond to either the tip or the surface breaks during the manipulation. The z area corresponding to feature A and B is highlighted in green. $z = 0$ Å corresponds to the height of (initial) contact formation. For more information see text.

Compare lifting of a complex with lifting of an isolated molecule

This section compares recorded curves for lifting the Ag+PTCDA complex and for lifting an isolated PTCDA molecule and determines their differences.

Fig. 5.7 shows the median curves, conductance and Δf, for the two manipulation cases. The median curves were calculated by taking the median value at every z position for the respective dataset.

The orange curves correspond to the manipulation of the Ag+PTCDA complex along a circular trajectory with HCM, introduced in this chapter. The tip-complex bond is formed once and the complex is manipulated repeatedly along the quarter circular trajectory. The first lifting of the complex from the adsorption configuration on the surface is removed from the dataset. The HCM data of the complex was chosen over the VM data due to the higher reproducibility of the HCM dataset.

The black curves serve as a reference to previously recorded data from manipulating an isolated PTCDA molecule along a vertical trajectory [62]. The molecule is only contacted once. Then, it is repeatedly lifted off the surface and brought back to the surface along a vertical trajectory. This is possible because the tip-molecule bond is stronger than the bond to the surface. The first lifting is removed from this dataset. All successive VM approach the surface for 1 Å less. Thus, the curves showing the VM of an isolated molecule do not reach the contact height (Fig. 5.7).

In the following discussion, lifting of the complex will be referred to as case 1 and lifting of the isolated molecule as case 2.

One of the first things to notice in Fig. 5.7 is, that case 1 stays longer in contact with both electrodes than case 2. For case 1, the tip-complex bond ruptures abruptly as the tip retracts from the surface. For case 2, the bond to the surface is cleaved smoothly, indicated by a peak-dip in the Δf signal.

To compare both cases, the height z^{b} where the bond to one of the electrodes breaks is chosen. The sharp drop in conductance at the end of the manipulation for case 1 indicates the separation from the SPM tip (Fig. 5.5). The knee in the conductance for case 2 indicates the separation of the O_{carb} from the surface. The two vertical lines (case 1: orange, case 2: grey) indicate z^{b} in Fig. 5.7.

The z^{b} difference between both cases is: $\Delta z = z^{\mathrm{b}}_{\mathrm{complex}} - z^{\mathrm{b}}_{\mathrm{PTCDA}} = 12.3\,\text{Å} - 9.0\,\text{Å} = 3.3\,\text{Å}$. The complex stands on a pedestal. The height of the Ag adatom can be approximated by a Ag(111) step height of 2.4 Å. Interestingly, the missing 0.9 Å have to come from a different junction configuration between case 1 and case 2. The complex is expected to be in a diagonal configuration before the rupture of the tip-complex bond (Fig. 5.8d). Thus, case 2 is **not** in a diagonal configuration on surface-molecule bond separation during lifting. This finding is supported by recent results suggesting two Ag-O bonds to the tip for case 2 [39]. A likely candidate is a straight orientation of the PTCDA molecule, since the difference between the diagonal and straight orientation is 1 Å.

The Δf signal is closely related to the molecule configuration in the junction. Its inspection reveals two new features for case 1, called feature A and B (Fig. 5.7). Feature A is a double peak around the z height of 5 Å - 9 Å. The additional conductance peak around $z = 7$ Å is associated with the rising flank of the second Δf peak. Feature B is a rising straight line around a tip height of 10 Å - 12 Å with a kink at the end, before the tip-complex bond starts to separate. Note that the kink (conductance and Δf) in the median curves is mainly an artefact due to the end of the data. The individual curves show a sharp drop in the corresponding signals.

Discussion of junction configuration during HCM along a circular trajectory

Fig. 5.8 shows a simple model of the junction geometry which will be used to link features A and B to the junction configuration during HCM along a circular trajectory. The model accounts only for the undisturbed complex. Any bending or stretching is neglected.

The Ag+PTCDA complex, the tip, and the tip trajectory are drawn to scale and they are all aligned in a plane vertical to the surface. This is the suggested alignment found by VM of the complex and the analysis of the molecule orientation before and after the manipulation in section 4.3.

The diagonal configuration, configuration 4, is the base configuration in this model. It is defined by the vertical alignment of: the Ag adatom, the contacted O_{carb} atoms and the apex atom of the tip. All other configurations are generated by rotating the complex around the centre of its adatom. See Fig. 5.8 for their definitions. The proposed configurations are linked to their expected features in the experimental Δf curve, indicated by vertical blue lines.

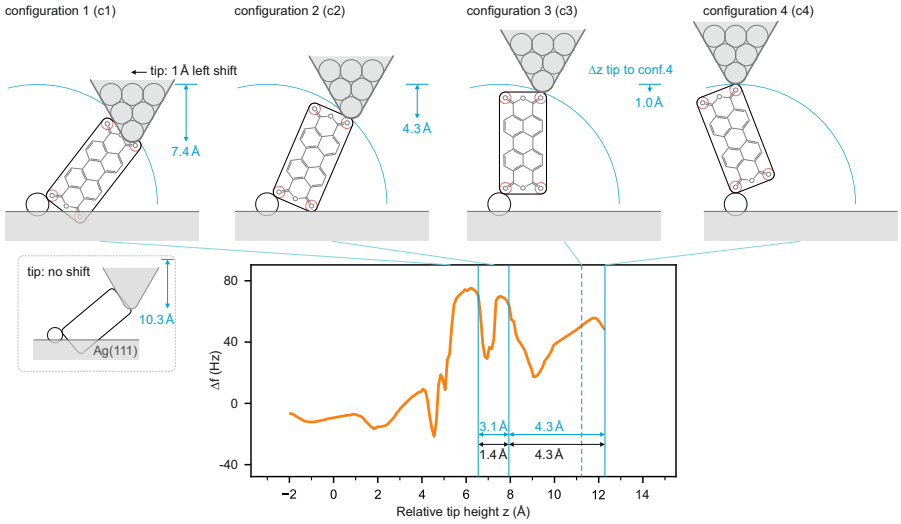

Figure 5.8: Simple model for the junction configuration during HCM considering only the geometry of Ag+PTCDA without distortions. Ag adatom, PTCDA and STM tip are drawn to scale. The blue quarter circle indicates the tip trajectory. The blue arrows (**c1** to **c3**) indicate the difference in tip height to **c4**. **c1**, Free "top" O_{carb} attaching to (or detaching from) tip. That the bottom corner is drawn below the surface is due to the simplicity of the model. This simply shows that the molecule must undergo a bending motion (and potentially a rotation out of the vertical plane) during the manipulation. **c2**, Free "bottom" O_{carb} attaching to (or detaching from) surface. **c3**, Straight configuration. **c4**, Diagonal configuration with the molecule fully stretched in the junction. The configurations are assigned to the Δf signal as indicated by the blue vertical lines. The line for **c3** is dashed, indicating the lack of a distinct Δf feature to assign to. The Δz values between the configurations in model (experiment) height are indicated in blue (black). For more information see text.

The junction configurations are further discussed below in ascending tip height. The configurations 1 to 4 in Fig. 5.8 will be referred to as c1 to c4. To simplify the reference to the two free O_{carb} of the complex during manipulation, they will be referred to in the following way: The "bottom" ("top") free O_{carb} refers to the free O_{carb} on the adatom (tip) side of the complex.

From lifting an isolated PTCDA molecule on a VM trajectory, it is known that a peak (or peak dip) in the Δf signal is the expected signature for a smooth separation of a bond between the molecule and one of the electrodes. It is also known that the O_{carb}-electrode separation occurs close to the peak (Fig. 5.7). The double peak of feature A, in the case of the complex, indicates two such events.

c1 and c2 would allow such a smooth bond separation. For c1, the top free O_{carb} is in contact with the tip edge and starts to separate from the tip on further tip retraction. c2 is defined in a similar way. Here, the bottom O_{carb} starts to separate from the surface on further tip retraction.

c1 and c2 are assigned to the experimental Δf curve similar to where $z^{\mathrm{b}}_{\mathrm{PTCDA}}$ is found. Therefore, they are assigned to higher z values slightly offset from the peak where the slope changes suddenly. The latter indicates a change in the junction configuration. c1 is assigned to the first peak of feature A and c2 is assigned to the second peak of feature A. Interestingly, the conductance curve shows a peak at the beginning of the second rising flank. Its origin is unclear.

The conductance peak could be a second Kondo peak. The first Kondo peak is at around 4 Å and a well understood feature for contacting and lifting an isolated molecule once from the surface [29]. In Fig. 5.7, the shape is however modified by the fact that cases 1 and 2 show successive manipulations of the same molecule without breaking of the dip-molecule contact. Thus, the junction configuration differs when the surface is approached with a previously lifted molecule, as opposed to when it is lifted for the first time. Given that the first Kondo peak is lower than feature A, this further indicates that both top O_{carb} atoms are in contact with the tip in that instance.

The conductance peak could also be a resonant tunnelling effect due to a nearly symmetric double barrier [63, 64, 65]. For c2, the angles of the short axis of the molecule to the surface and to the tip are similar. On the other hand, the surface has two Ag-O bonds to the molecule, while the tip has only one.

C1 requires further discussion: First, the proposed structure overlaps with the Ag(111) surface. This simply indicates that mechanical stress in form of bending of the bottom corner is required in a real configuration. However, this is not accounted for in the model. It is known from contacting experiments of a molecule in a single monolayer of PTCDA/Ag(111) that the corners of a PTCDA molecule allow significant bending (**??**). Second, the height prediction for c1 strongly depends on the exact configuration of the two Ag-O bonds with the tip. This is indicated by the upper and lower junction configurations proposed for c1 in Fig. 5.8. The lower configuration is generated by rotating c4 around the Ag adatom (the same as for c2 and c3). The upper configuration takes into account (in part) the 3D shape of the tip and allows the complex to be attached to the side of the tip. Here, the position of the tip is shifted 1 Å to the left compared to the bottom configuration. This simple change allows the top free O_{carb} to stay in contact with the tip about 3 Å higher.

C3 is assigned to feature B and positioned 1 Å lower than c4, as predicted by the model. The lack of a distinct Δf feature for the assignment is indicated by a dashed blue line in Fig. 5.8, in contrast to the solid lines for the other configurations.

The model predicts the start of feature B between c2 and c3. Both bottom and top O_{carb} are unbound and the molecule "climbs" on the adatom until it reaches the diagonal configuration c4. This is supported by the Δf curves from lifting of the complex with VM, which show that the influence of the surface corrugation is small in the height range of feature B, as the VM curves show little spread (Fig. 5.6b). In particular, the rising straight line of feature B should be closely related to the stiffness of the Ag+PTCDA complex, including the bonds to the adatom and tip.

Interestingly, the stiffness increases linearly with the distance. The reason for this is unclear. A simple explanation could be the difference in stiffness against lateral and vertical movement of the adatom on the surface. The superposition of these changes in favour of the

higher stiffness against vertical movement when approaching the diagonal configuration c4. A similar argument would apply to the Ag atom at the tip apex, as well as to the difference in stiffness for the Ag-O bonds against rotation and stretching.

The rise in conductance during feature B, until the drop related to the beginning of tip-complex bond separation, could be due to increasing mechanical stress [66]. However, note that the conductance decreases with increasing stress in the molecular wire in the reference. The increase in conductance could also be a consequence of the junction becoming more and more symmetric, as discussed above for feature A.

While the absolute heights from the model cannot be directly compared with the relative tip heights from the experiment, the Δz between configurations can. The $\Delta z^{1,2}$ between c1 and c2, as well as $\Delta z^{2,4}$ between c2 and c4, are indicated in Fig. 5.8 for the model (blue) and the experiment (black).

$\Delta z^{2,4}$ for the model and experiment fit surprisingly well, considering the simplicity of the model. This is a strong indication that c2, c3, and c4 are indeed the configurations of the complex during HCM. It also means that the complex is in a "wire" configuration over a long z range of 5 Å, which could be beneficial for certain conductance experiments.

$\Delta z^{1,2}$ diverge by a factor of 2 between model and experiment. Thus, distortions of the complex can no longer be neglected. This is also clear from c1 in Fig. 5.8, where the free bottom O_{carb} goes below the surface and has to bend in the experiment. Due to the large discrepancy between model and experiment, c1 can only be treated as a hint for the correct configuration.

5.3.4 Summary and outlook

Section 5.3 shows promising results towards fully reproducible conductance measurements with an SPM. The combination of an adatom anchor and a circular trajectory successfully reduces the influence of the surface corrugation during the manipulation of a Ag+PTCDA complex on Ag(111), compared to a vertical manipulation trajectory. This was shown for the Δf signal, because the control over the junction configuration determines the reproducibility of the conductance signal.

Of course, the reproducible preparation of the tip apex is still a challenge. This could potentially be overcome by scanning the tip over a CO molecule adsorbed on the substrate surface to categorise the tip shapes [67].

Analysis of $z^{b}_{complex}$ and z^{b}_{PTCDA} points, in case of lifting an isolated PTCDA molecule, to a straight configuration at surface-molecule bond separation with two O_{carb} bonds to the tip.

Two new features could be identified in the Δf signal for the case of the complex in comparison to the case of lifting an isolated molecule. Feature A shows a double peak in Δf and a conductance peak in the rising flank of the second peak. Feature B shows a rising straight line and a kind in Δf, while the conductance increases towards the kink.

There are strong indications that the second peak of feature A until the rupture of the tip-complex bond corresponds to the model configuration 2, 3, and 4. Namely, the bottom free O_{carb} starts to separate from the surface in configuration 2. The PTCDA molecule then "climbs" the adatom until a diagonal configuration is reached before bond rupture. Further

molecule mechanics simulations, supplemented by DFT calculations, are required to verify the proposed junction configuration and to determine the configuration for the first peak of feature A.

The complex is in a wire configuration when the bottom free O_{carb} detaches from the surface. Here, the contact between the electrodes and the PTCDA molecule is highly controlled and corresponds to two single atom contacts (the tip-apex atom and the adatom). Furthermore, the long z range of 4.3 Å of the wire configuration could benefit certain conductance experiments.

The origin of the conductance peak of feature A and the rise in conductance in feature B towards the tip-complex bond rupture are unclear. The conductance peak could be a second Kondo peak. Both increases in conductance could also be due to mechanical stress or resonant tunnelling through a double barrier. Here, further experiments are needed. For example, splitting of the Kondo peak in a magnetic field would allow a clear identification. Or in case of resonant tunnelling, the position of the resonance peaks should be V_{bias} dependent.

CHAPTER 6

Autonomous three-dimensional manipulation

Contributions

This chapter is based on the preprint in [68] and the journal article published in Science Advances [42]. The author contributions were as follows: C.W., K.T.S., K.-R.M., and F.S.T. conceived and designed this research during the IPAM long program "Understanding Many-Particle Systems with Machine Learning." M.E. and K.T.S. designed and implemented the RL agent. P.L. performed the experiments. C.W., P.L., and M.E. analysed the data. C.W., K.-R.M., and F.S.T. developed the conceptual framework. M.E., C.W., and F.S.T. wrote the paper, with input from all authors.

6.1 Introduction

Automated, bottom-up nanofabrication is a promising step towards molecular electronics, and would allow the routine construction and characterisation of functional metastable structures or assemblies. This can be translated into a robotic task with end-effectors capable of single-molecule manipulation being available, like: SPM tips, magnetic or optical tweezers [69].

However, robots usually interact in the macroscopic world, where their actions can be guided by human expertise or simulations. Likewise, it is also possible to monitor the robot's work area, including the effector and the workpiece, e.g. using cameras. At the nanoscale, we lack both, intuition for the mechanics and full observability of the manipulation process. Atomic simulations, which are precise enough to be useful for manipulating single molecules, are still computationally too expensive. In addition, it is not (yet) possible to observe the complete state space relevant to the manipulation, including the atomic coordinates of the end-effector (the SPM tip), the manipulation object (single atoms or molecules) and the surrounding surface. This poses an additional problem: The fabrication of atomically identical SPM tips is challenging. A slight variation in the atomic structure, especially around the tip apex, can significantly alter the properties of the tip. And due to our lack of observability, the atomic structure of the currently used tip is often unknown. A human operator can still achieve the nanofabrication goal by adapting the manipulation protocol to fit the current properties of the tip (see section 3.3). However, with the lack of intuition and the lack of observability, the operator can only adapt the manipulation protocol using a trial-and-error approach. Since adjustments may need be made for each tip, this is very time consuming and calls for *autonomous* robotic nanofabrication.

Autonomous robots are capable of planning and performing actions to accomplish tasks in an environment by themselves, without explicit human control. The advantage of autonomous single-molecule manipulation is that the robot can adapt the manipulation protocol to fit the current properties of the atomic structure of the SPM tip.

A promising candidate for the realisation of autonomous nanofabrication is Reinforcement Learning (RL) [70, 71, 72]. Here, a software 'agent' interacts with an environment to solve a specific task by maximising a reward signal. The agent can choose from a pool of actions to change the state s_t of the environment, one action a_t per time step t. A reward r_{t+1} is emitted by the environment for executing a_t and transitioning to s_{t+1}. Starting from the initial state s_0 the agent learns by trial-and-error, similar to human learning. The actions performed are initially random. Over time, the agent accumulates experience about the relationship between choosing a_t, observing the transition $s_t \rightarrow s_{t+1}$ and receiving r_{t+1}. From this experience the agent can derive a policy π for assigning action-selection probabilities to the actions at each state so as to maximise the sum over the received rewards $\sum_{t=1}^{T} r_t$. r_T denotes the received reward when reaching the terminal state s_T. The policy is learned by the agent, without any prior knowledge of the environment. RL can handle sparse rewards (necessary because of the lack of observability), such as: $r = -1$ for failure (reaching s_T^-) and $r = +1$ for success (reaching s_T^+). The advantages and limitations of autonomous molecule manipulation via RL are summarized in the following.

Advantages:

- No prior model or simulation required
- Same algorithm can be used to achieve different manipulation goals
- Autonomous refinement of learned trajectory to fit current SPM tip properties

Limitations:

- Repeatability of experiment and clear detection of start configuration required
- Clear detection of success and failure required
- Training time increases with the state space. In this study, a neural network is used as a function approximator over the state space. Therefore, training time only increases with the number of neurons.

This chapter presents the first application, to the author's knowledge, of RL to the task of automated manipulation of single molecules. The manipulation goal is the controlled removal of single molecules from a self-assembled PTCDA/Ag(111) monolayer using an SPM tip (see section 3.3 and Fig. 6.1). The agent has to learn to execute a complex 3D manipulation trajectory to overcome the intermolecular interactions in such a layer, which are dominated by hydrogen bonds (right panel in Fig. 6.1a). This is a challenging task that (until now) could only be performed by a human (see section 3.3). The combination of passive self-assembly and active (re-)arrangement of the building blocks, e.g. by removing single molecules from a self-assembled layer, has been identified as a key capability for realising functional molecular structures [73, 74].

6.2 Agent setup and discussion

PTCDA molecules can spontaneously bind to the SPM tip and be removed from a monolayer upon tip retraction on a suitable trajectory. A successful lifting trial begins with the initial tip-molecule bond formation, includes the refinement of the manipulation trajectory and ends with the removal of the molecule. Each manipulation trajectory is an episode, from tip-molecule bond formation until rupture (or removal of the molecule).

From previous experiments using HCM to create single-molecule vacancies inside a compact PTCDA/Ag(111) layer (see section 3.3) it is known that the lifting task fulfils the requirements to be solved as a RL task: First, PTCDA self-assembles into a perfect 2D lattice on a Ag(111) surface with the unit cell shown in Fig. 6.1a. Therefore, an identical molecule can be contacted at the beginning of a lifting trial. Likewise, after a tip-molecule bond rupture, the molecule self-assembles back into its vacancy. Thus, the molecule can be always contacted again at the same position during a lifting trial, without the need to rescan the area. Second, bond formation (rupture) is observed by a sharp increase (decrease) of I (left inset in Fig. 6.1a) or a kink in Δf. Therefore, any rupture of the tip-molecule bond can be clearly observed and a failure terminal state s_T^- is assigned. Third, with the length of the molecule being 11.5 Å, any tip position with $z > 14$ Å and the tip-molecule bond intact is a success s_T^+.

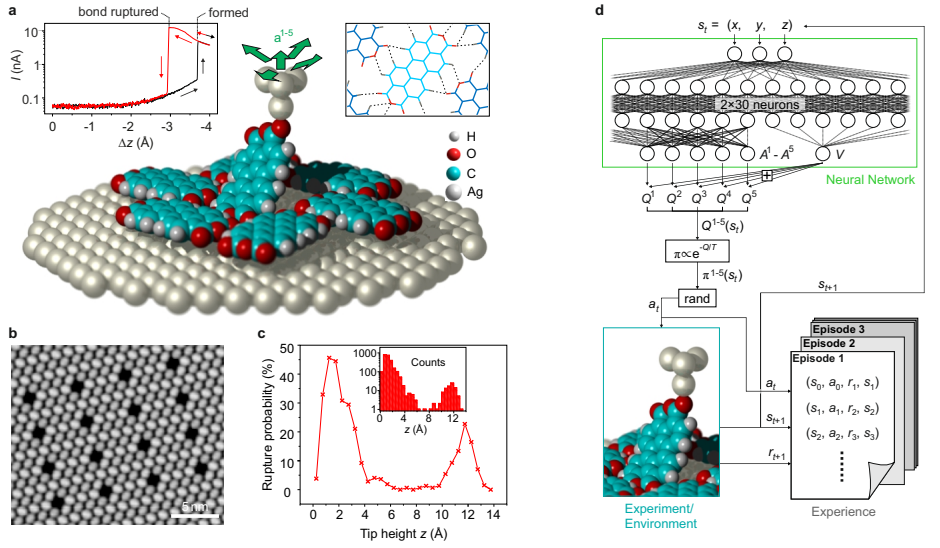

Figure 6.1: Removal of single molecules from PTCDA/Ag(111) by a RL agent. **a**, Rendered scene of a PTCDA molecule being partial lifted from the layer with a Ag-terminated tip. The five actions a^{1-5} for steering the SPM tip by the agent are indicated by green arrows. Bond formation (rupture) causes a sharp increase (decrease) in the tunnelling current (left inset). The removal task is difficult since PTCDA is retained in the layer by a network of H-bonds (dotted lines in right inset). **b**, STM image of a PTCDA layer with 16 vacancies created by the RL agent. **c**, Rupture probabilities as a function of z calculated in 0.5 Å intervals from all ruptures accumulated over RL-agent experiments (inset). **d**, The optimal $Q^\star$-function is approximated by a neural network with 30 neurons in the first, and 2×15 neurons in the second hidden layer. This duelling network architecture [75] features separate outputs A^{1-5} and V, with $Q^{1-5} = V + A^{1-5}$ for actions a^{1-5}. The policy π_t assigns action-selection probabilities to a_t^{1-5} for choosing a_t at random.

Robotic nanofabrication as a reinforcement learning challenge

A Markov Decision Process (MDP) [70] is often used to model RL tasks. A Markov process consists of states and the transitions between states are stochastic. Additionally to a Markov process, an agent can choose an action in each state to influence the transition into the next state in a MDP. Markov processes satisfy the Markov property and are thus stationary - the transition probability $P(\bar{s}_{t+1}, r_{t+1} \mid \bar{s}_t, a_t)$ from the present state $\bar{s}_t$ to a future state $\bar{s}_{t+1}$, *after* choosing a_t, depends only on $\bar{s}_t$ and *not* on the past: $\bar{s}_{t-1}, ..., \bar{s}_0$. Note that the reward r_{t+1} is also included in the definition of the transition probability.

In the context of robotic nanofabrication, the *complete* state description $\bar{s}$ includes the coordinates of all relevant atoms of the environment, where transitions between states are stochastic for high temperatures. In the case presented, however, the situation is different in two aspects: One, the transition between states is deterministic at low temperatures, as the SPM operates at 5 K). Two, monitoring $\bar{s}$ during nanofabrication is impossible with current technology. Therefore, an *approximate* state definition s has to be used.

Several elements could be included in the definition of the approximate state s: First, the xyz position of the tip is known. Second, some observable quantities are typically available for a nanomanipulator system which are functions of $\bar{s}$ (e.g. for the SPM in this study: I, Δf).

To solve the lifting task discussed here, a state description consisting only of the xyz coordinates of the SPM tip was chosen to keep the complexity as low as possible for this proof-of-concept study. The start configuration is defined as $s_0 = (0, 0, 0)$. In general, the tip displacements during lifting could be arbitrary and continuous. To further reduce the complexity, a set $\mathcal{A}$ of five discrete actions was chosen (green arrows in Fig. 6.1a), limiting the set of states $\mathcal{S}$ to a finite number of discrete states (in the space relevant to the manipulation). All five actions include a step $\Delta z = 0.1\,\text{Å}$ away from the surface and were defined as follows, with all values in Ångstroms: $(0, 0, 0.1)$, $(\pm 0.3, 0, 0.1)$, $(0, \pm 0.3, 0.1)$.

Strictly speaking, this approximate state definition does *not* have the Markov property, since the manipulated PTCDA molecule could assume different conformations at identical SPM tip locations for different tip trajectories leading to that location. Nevertheless, the removal task in this study was successfully solved using the Cartesian tip coordinates as states, validating the proposed approach.

An important consequence of this approximate state definition is that, for example, changes in the tip or a drift in the positioning system are *not* captured by s_t. These changes induce a state transition $\bar{s}_t \to \bar{s}'_t$, from the complete state $\bar{s}_t$ to some other complete state $\bar{s}'_t$ during time step t, thus changing $P(\bar{s}_{t+1}, r_{t+1} \mid \bar{s}_t, a_t)$ to $P(\bar{s}'_{t+1}, r'_{t+1} \mid \bar{s}'_t, a_t)$. But the approximate state s_t remains unaffected. However, the emitted reward r_{t+1} in the probability distribution of the approximate states $P(s_{t+1}, r_{t+1} \mid s_t, a_t)$ may *change* when the hidden state $\bar{s}_t$ changes.

Changes in the atomic structure of the tip apex can affect the strength of the tip-molecule bond. If the bond becomes weaker (stronger), less (more) deviation from the optimal lifting trajectory is allowed, increasing (decreasing) the difficulty of the lifting task. Removing the molecule from the surface may even become impossible at all (see 'tip fail' in Fig. 6.3a). Therefore, in this study, a lifting trial was aborted if the tip changed *during* the trial and removed from the statistics.

This non-stationarity is a key challenge for the lifting task discussed here, but also for nanofabrication in general when using an approximate state description. It could render the accumulated experience at least partially worthless, because the successful policy is not static but needs to be constantly evolved.

Further, the learning speed for a policy must be faster than the rate at which $P(s_{t+1}, r_{t+1} \mid s_t, a_t)$, more precisely the correlation between s_{t+1} and the emitted reward r_{t+1}, changes. This requires a substantial increase in the training efficiency of the standard RL algorithm, which is typically very low and requires a lot of training data. If a policy $\pi(s_t)$ can be learned in the lifetime of $P(s_{t+1}, r_{t+1} \mid s_t, a_t)$, the agent could adapt to occasional hidden changes in $\bar{s}$.

In this study, two modifications to the standard RL algorithm were applied to speed up learning sufficiently to solve the lifting task (see end of section 6.2).

Training the agent

First, an agent acts in an environment by choosing an action a_t and executing it. Then, the agent observes the transition from $s_t \rightarrow s_{t+1}$ on action a_t and receives a reward r_{t+1} emitted by the environment for choosing a_t. The observed transition and the received reward are stored in the agent's experience memory as an experience tuple $e_t = (s_t, a_t, r_{t+1}, s_{t+1})$ (Fig. 6.1d). They are used during training to calculate the loss function L (see below). The reward function for this study was defined as a combination of sparse reward (failure: $r = -1$, success: $r = +1$; see section 6.1) and slight reward shaping by using an additional default reward of $r = 0.01$ for all other (non-terminal) states. A small positive default reward for each action is physically motivated, since each action separates the molecule $\Delta z = 0.1$ Å from the surface, bringing the agent closer to its manipulation goal (Fig. 6.1a).

Unlike the reward function, which indicates what is good in the immediate sense, a value function indicates what is good long-term. Values are assigned to states and correspond (roughly) to the total reward an agent expects to accumulate in the future, starting from one state onwards and using its current policy. Choosing an action is based on the value function. For this study, the Q-function was used as the value function and was learned by the agent (Fig. 6.2c). It considers not only states but also state-action pairs for the evaluation.

Here, a Neural Network (NN) (Fig. 6.1d) is used to approximate the optimal Q-function $Q^\star(s_t, a_t) = \max_\pi \left[r_{t+1} + \gamma r_{t+2} + \gamma^2 r_{t+3} + ...\right]$, which is the maximum sum of the expected rewards, discounted by γ, by following a policy π after time step t. In a given state, the policy π assigns action-selection *probabilities* to each action, depending on their respective Q-values. π is computed using the (normalised) Boltzmann distribution

$$\pi(s_t, a_t) = \exp\left(-\frac{Q^\mathrm{B}(s_t, a_t)}{T}\right) \Big/ \sum_{a \in \mathcal{A}} \exp\left(-\frac{Q^\mathrm{B}(s_t, a)}{T}\right), \tag{6.1}$$

with $Q^\mathrm{B} \stackrel{!}{=} -Q$ to preserve the shape of the Boltzmann distribution. Note that a high Q-value corresponds to a high probability of choosing an action, in contrast to the energy/occupation relationship for which this distribution was derived (for positive T; the next section discusses a possible advantage of using negative T values during training to propagate failure states more efficiently). Because π assigns a probability to the choice of a_t in s_t, the Boltzmann distribution for the state-action pair (s_t, a_t) is normalised by the sum of the distributions $\sum_{a \in \mathcal{A}} \exp\left(-\frac{Q^\mathrm{B}(s_t, a)}{T}\right)$ for all (s_t, a) with $a \in \mathcal{A}$. The 'temperature' parameter T determines how greedy the agent chooses actions with higher Q-values. For a positive (negative) 'temperature' with $T \rightarrow +0$ ($T \rightarrow -0$) only the action with the highest (lowest) Q-value is selected. The agent chooses random actions for $T \rightarrow \pm\infty$.

To update the predicted Q-values during training, an off-policy variant (see next section) of the Expected SARSA [76] (State-Action-Reward-State-Action) algorithm is used. The loss L, the difference between the predicted and the actual (discounted) cumulative reward,

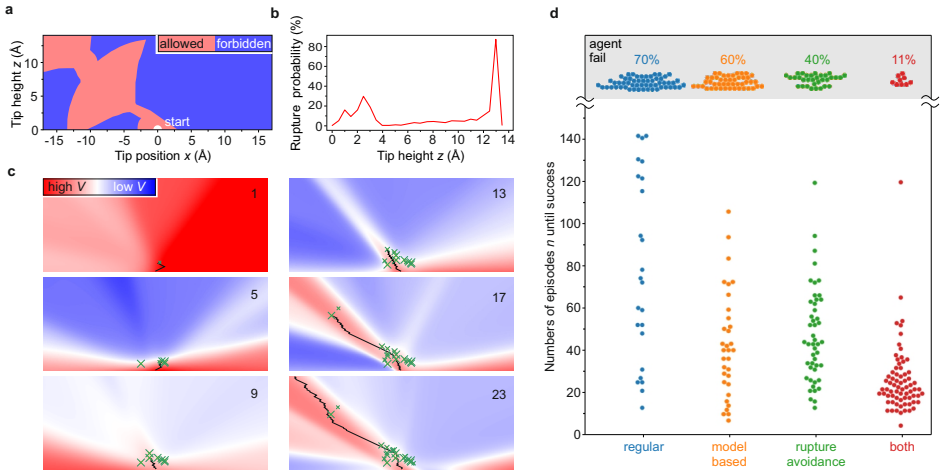

Figure 6.2: Training and performance of RL agents. **a**, Map (2D slice through 3D system; $y = 0$) of the synthetic bond rupture criteria of the simulated environment. **b**, Synthetic rupture probability as a function of z calculated in $\Delta z = 0.5$ Å intervals. **c**, Maps (2D slices; $y = 0$) of the Q-functions for different episodes of one successful lifting trial, showing the learning progress by the agent after the number of episodes indicated in the upper right corner. The executed trajectory by the agent (black curve; 2D projection) in each panel is based on the Q-function of the same panel. Green crosses indicate synthetic bond-ruptures triggered according to the criteria in **a**. **d**, Swarm plot showing the performance of different types of RL agents acting in the simulated environment in **a**. The number of episodes n needed to finish the removal task is plotted for 80 simulated experiments, or runs, for each agent. A run was considered a failure after 150 unsuccessful episodes (see text). The respective probability of agent-failure is indicated in the upper part of the plot.

is calculated as

$$L(s_t, a_t) = \left[Q(s_t, a_t) - \left(r_{t+1} + \gamma \sum_{a \in \mathcal{A}} \pi(s_{t+1}, a) Q(s_{t+1}, a) \right) \right]^2 \tag{6.2}$$

and used to optimise the NN weights via gradient descent with samples obtained by prioritised sampling [77] from the experience memory. Note that the discounted ($\gamma = 0.97$) future reward is given by the Q-function itself. This recursive formulation, called temporal-difference learning, allows Q-values to be learned and propagated through the state space very efficiently [70].

Simulation results and RL adjustments

Before connecting the agent to the SPM, it is benchmarked on a simulated system using synthetic rupture criteria (Fig. 6.2a) derived from previous lifting experiments with HCM (see section 3.3). The performance of an agent is measured by the number n of removal attempts (episodes) needed to successfully finish a lifting trial. The realistic, simulated environment allowed to test different training and exploration strategies to achieve the manipulation goal

(see below), as well as to optimise the hyperparameters of the NN to be as training-efficient as possible for the real experiment. Tuning the agent in a simulated environment saved a lot of valuable time on the SPM.

The rupture criteria in Fig. 6.2a are based on a successful HCM trajectory around which a corridor of variable diameter has been defined (red) beyond which the bond ruptures (blue). The diameter is chosen to approximate the experimental bond-rupture probabilities (Fig. 6.1c). They show two distinct heights with increased rupture probability, which are critical to overcome for successful lifting. Note that the rupture probability is well captured in the simulation (Fig. 6.2b) compared to the real experiment (Fig. 6.1c).

Although the simulation environment is fully observable and a stationary problem, a regular agent typically requires more than 150 episodes to find a successful policy π (Fig. 6.2)d). As discussed above, this low data efficiency would make it (almost) impossible to find π before $P(s_{t+1}, r_{t+1} \mid s_t, a_t)$ changes due to the non-stationarity of a real-world experiment.

Driven by the need to solve the task more efficiently, two modifications are made to the standard Expected SARSA algorithm. First, the purely Cartesian state description is exploited to perform model-based RL similar to the Dyna algorithm [78]. Dyna uses both actual experience from interacting with the environment, and experience obtained from a learned environment model to update the Q-values. Learning the environment model of this task is simple, because the state transitions from s_t to s_{t+1} are deterministic. The reward emitted by the environment model is implemented similarly to the reward function of the real environment. The default reward is $r = 0.01$ and in case the successor state is a known terminal state, the respective reward is emitted (failure: $r = -1$; success: $r = +1$). For training, model 'experience' tuples e^{model} are sampled around the states contained in the actual experience additional to sampling e_t directly from the experience memory.

Second, a rupture avoidance mechanism is implemented by setting a negative temperature $T_{\text{train}} < 0$ during training when eq. (6.1) is inserted into eq. (6.2). Using a negative temperature gives *lower* Q-values *more* importance in eq. (6.2). Information about visited failure states are propagated much further towards preceding states and the agent can use this information to avoid them. Of course, a positive temperature $T_{\text{act}} > 0$ is used for acting in the environment.

Fig. 6.2d shows the performance of agents using either of the modifications separately or both combined, compared to the performance of a regular agent. When the two modifications are combined, the substantial increase in the learning speed allows to deploy this modified agent to be used in the real-world experiment.

Discussion of rupture avoidance mechanism

While model-based RL increases the efficiency of training on real-world experience, the rupture avoidance mechanism increases meaningful exploration of the agent. If a tip-molecule bond rupture is detected at one position, it is very likely that a bond rupture will also occur in its vicinity. Therefore, a mechanism was implemented, where the agent avoids states that are known to be failures, in particular, also the states that lead up to them. Note that the mechanism implemented here is only an example. Any other mechanism which allows

efficient exploration could substitute the rupture avoidance mechanism implemented in this study.

A standard RL agent, like the regular agent in Fig. 6.2d trained with eq. (6.2), tends to 'ignore' future negative rewards, if there exists a strategy that narrowly avoids them. Future rewards are weighted by the policy π in eq. (6.2). For $T \to 0$ all Q-values except the highest one are ignored. Therefore, the information of a failure state s_T^- up ahead is already 'forgotten' two states below. Only if all future states s_{t+1} from s_t are terminal states s_T^- will the information propagate to s_{t-1}. Therefore, the regular agent will try to lift the molecule along a similar path leading to failures at nearly identical positions, and thus, inefficient exploration.

To reduce the risk of a tip change during a lifting trial, the agent needs to explore as efficiently as possible. By using a negative temperature $T_{train} < 0$ to evaluate eq. (6.2) during training the weighting of the Q-values is reversed. Now lower Q-values, indicating a danger of rupture, are weighted stronger and thus propagated further. Note that there is a trade-off. The more the agent tries to stay away from previous failures, the more likely it is to miss a small traversal path in the vicinity of failures.

Discussion of model-based planning

Standard RL is completely unbiased about its environment and the agent only finds the relationship between actions and state transitions by interacting with the environment. While this is good in general, for a robot acting in a real-world environment training efficiency is vital. Combining the agent with a model of the environment for model-based planning can significantly increase training efficiency. Here, a variant of the Dyna algorithm [78] was implemented to use the same RL method for updating π for samples drawn from the experience memory and samples acquired from the model (or model environment). Knowledge implemented in the model is automatically acquired by the agent when sampling from the model.

In this study, the agent acts in 3D space and the state s is defined as the Cartesian tip coordinates. Further, the available actions $a \in \mathcal{A}$ only modify the tip position, in discrete steps. Failures s_T^-, rupture of the tip-molecule bond, occur at random tip positions, but are (assumed to be) stationary during the whole lifting trial. Successes s_T^+ are treated similarly, but less important because the trial is finished when the molecule is removed from the layer.

This knowledge is used to construct a simple model environment which is updated or learned by the agent as it gains experience in the (real) environment. For the approximate state description, all possible states are known and $P(s_{t+1}, r_{t+1} \mid s_t, a_t)$ is deterministic. This means that a transition $s_t \to s_{t+1}$ to on action a_t is known a priory and s_{t+1} is guaranteed to be a new state. Therefore, the model can generate s_{t+1} for any given state-action pair (s_t, a_t). Besides generating s_{t+1}, the model also has to emit a reward for reaching s_{t+1}. Similar to the real environment, a default reward $r = +0.01$ is emitted. Initially, failure states s_T^- (and successes s_T^+) are unknown to the agent (and thus to the model as well). The list of terminal states is learned over time by gaining real experience. If (s_t, a_t) leads to a recorded terminal state, the respective reward $r = -1$ for s_T^- or $r = +1$ for s_T^+ is emitted.

For training, the model is used to extend the agent's knowledge around previously executed trajectories. Model environment tuples $e_t^{\text{model}} = (s_t, a_t, r_t, s_{t+1})$ are used similarly to real experience to update π. A tuple is generated by randomly selecting a state s_t in the vicinity of the states actually visited. Then a random action is selected. s_{t+1} is generated by the model from (s_t, a_t) and the respective reward is emitted.

Outlook - Integrating experimental signals into the model

A future strategy could involve including the experimental signals I and Δf to (partially) recover the Markov property. They are functions of the complete state $\bar{s}$ and therefore carry information about the atomic coordinates relevant during the manipulation, including the conformation of the molecule and the atomic shape of the tip apex. This could help the agent to make more informed decisions when choosing actions during a lifting trial.

There are two challenges, when extending model-based RL from a Cartesian state description $s(x, y, z)$ to $s(x, y, z, I, \Delta f)$. First, the model has to be modified to allow model-based planning. Second, to tune the hyperparameters of the NN a new simulated environment is needed. In principle, the NN from this study (Fig. 6.1d) could be used with only two additional neurons added in the input layer for I and Δf. As the NN is a function approximator, continuous inputs can be used. However, it is unclear how well this network will perform in the new task if approximating the Q-function for $s(x, y, z, I, \Delta f)$. Is the number of neurons in the hidden layers enough to cope with the additional two dimensions of the state space? Are more layers needed? What about the temperature parameter T, to evaluate the policy, and the learning rate?

The author suggests the following modifications to the model, to keep it as simple as possible: First, one could assume that I and Δf do not change (much) when sampling unvisited states around previously executed trajectories. Therefore, sampling s_t^{model} from the model would be performed similarly to before, using only xyz coordinates. Then I_t and Δf_t would be taken from the experience tuple e_t around which e_t^{model} is generated, for both s_t^{model} and s_{t+1}^{model}. Second, if the transition $s_t^{\text{model}} \rightarrow s_{t+1}^{\text{model}}$ leads to a terminal state, the model should emit the respective reward.

With continuous inputs included in the state definition, matching precisely a recorded terminal state $s_T(x_T, y_T, z_T, I_T, \Delta f_T)$ would be up to chance and therefore inefficient. Here, one could also use the xyz coordinates exclusively to determine the transition to a terminal state. This can be physically motivated, because the positions of s_T^- (and also success s_T^+) are stationary as long as there are no hidden changes in $\bar{s}$, e.g. the tip apex stays identical. However, this is only true if the agent chooses exactly the same tip trajectory that lead to the rupture. If the same position is reached coming from a different path, the molecule could be in a different configuration and no rupture may occur.

From the discussion above it is clear that the model can be extended to account for I and Δf, but constructing a simulation environment to tune the hyperparameters of the NN will be challenging. The simulation would have to generate I and Δf signals for all possible tip positions. To provide these values, two NN could be trained on experimental data, one for the I signal and one for the Δf signal. In both cases, the input layer would consist of three neurons for the tip coordinates. The output layer would consist of a single neuron

and its output value would be either the predicted I or Δf signal. To preserve the path dependence of the experimental signals, two Long Short-Term Memory (LSTM) networks could be trained instead. At time step t, such a network would have an additional input for the network weights at $t-1$. Thus, the output at time t depends on the input at $t-1$. Therefore, an LSTM can preserve information from previous time steps in an episode.

6.3 Experiment and discussion

The experiments were performed on PTCDA/Ag(111) (see section 2.3 for preparation) with an SPM operating at 5 K. During lifting, a bias voltage of 10 mV was applied and I was monitored by a custom script (see section 6.5.1), for automated detection of bond rupture and re-establishment of the tip-molecule bond. The molecule manipulation is controlled by the software program 'RL agent' (see section 6.5.1), which sends commands to (re-)position the SPM tip. After each tip positioning step (action), the configuration of the molecule is changed and the RL agent receives the respective reward: bond intact ($r = 0.01$), bond ruptured (s_T^- and $r = -1$), removal successful (s_T^+ and $r = +1$).

At the start a lifting trial, an STM image was recorded of a PTCDA molecule in a monolayer to identify the contact position. After tip-molecule bond formation, the RL agent autonomously manipulates the molecule and refines the executed tip trajectory over a series of episodes. One episode begins with the bond formation and ends with either a failure s_T^- or a success s_T^+. The final success of the manipulation is verified by the experimenter, who deposits the molecule from the tip elsewhere on the Ag(111) surface (see section 3.2.3) and images the vacancy that has been created in the PTCDA layer (Fig. 6.1b).

Fig. 6.1a shows a rendered scene of the experiment, where a PTCDA molecule is lifted from a closed PTCDA layer on Ag(111) by the agent, surrounded by its nearest neighbours. Removal was only attempted on every third molecule in a layer, to ensure, that a lifting trial was unaffected by the vacancies in its vicinity (Fig. 6.3b). The implementation of the agent is sketched in Fig. 6.1d.

Fig. 6.1c shows the probability of tip-molecule bond rupture during an episode, in dependence of the tip height z, calculated from all RL-agent experiments. Two heights with increased rupture probability can be identified and are referred to as first (lower height) and second height (upper height). Their z distance corresponds quit well to the length of the PTCDA molecule. They can therefore be assigned to the detachment of the carboxylic oxygen atoms O_{carb} from the surface at each end of a PTCDA molecule (along its long axis). This was known qualitatively before [21]. However, the high number of episodes available through automated manipulation allowed its quantification.

While the density of ruptures is sufficient to map the rupture positions around the first height, the density decreases for the second height. There are two reasons for this. On the one hand, many trajectories rupture on the first height and thus do not contribute to the mapping of the second height (inset Fig. 6.1c). On the other hand, the volume of allowed tip positions (Fig. 6.2a) increases for the second height, further reducing the density of ruptures even further. Note that the experimental rupture probability is better captured in the synthetic rupture criteria for the first height than for the second height (Fig. 6.2a,b).

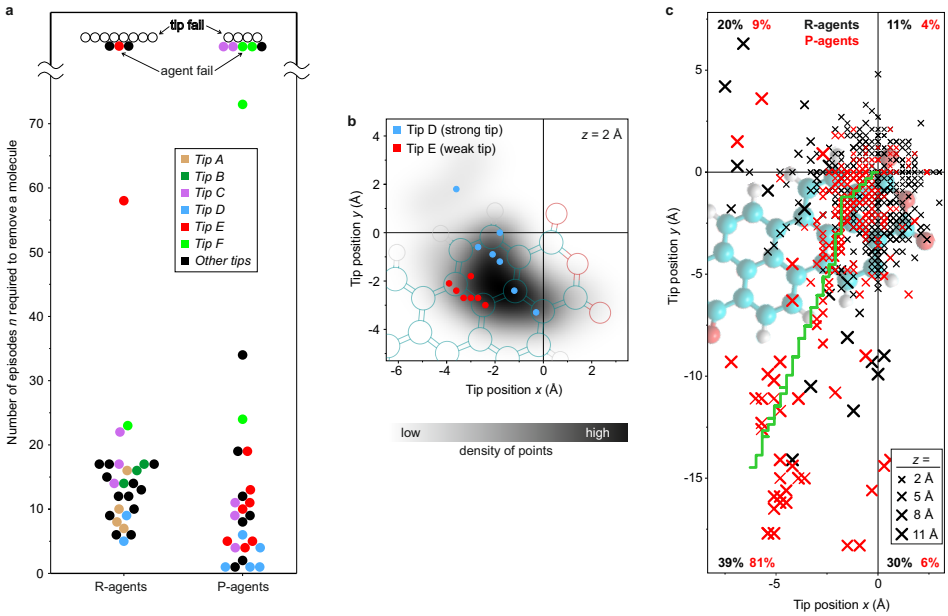

Figure 6.3: Performance of the RL agent in the experiment. **a**, Swarm plot of required episodes n to accomplish the removal task for R- and P-agents. Data points of lifting trials executed with the same tip are coloured identical (except black), if three or more data points were available for one tip. A data point is denoted as 'tip fail' ('agent fail'), if the tip (agent) is responsible for the failure of the lifting trial (see text). **b**, Density of xy positions based on all successful trajectories at $z = 2$ Å, where they safely pass the area of highest bond-rupture probability Fig. 6.1c). The positions of trajectories recorded with tip E and tip D are indicated by dots. **c**, xy projection of all bond ruptures within the first ten episodes for R-agents (black crosses) and P-agents (red crosses). Cross sizes indicate rupture heights z. The percentage of ruptures in each quadrant is indicated by the numbers in the respective corner. The green curve shoes the last trajectory (2D projection) executed by the P-agents during pre-training.

Lifting PTCDA and analysis of the learning process

A lifting trial was aborted and excluded from the analysis in Fig. 6.3 when the tip changed *during* the trial, because the difficulty of the removal task depends on the structure of the tip apex (as discussed in section 6.2).

A successful lifting trial, resulting in the removal of the contacted molecule, took typically 5 min - 10 min. The tip apex changed *during* 20 % of the lifting trials (not to be confused with episodes), which were therefore excluded from the analysis. Redeposition of the removed molecule onto the surface changed the apex with a probability of 15 %. Both effects combined explain why the number of data points in Fig. 6.3a for identical tips are rather low (coloured dots) and why there are many data points that do not belong to an explicit group (black dots).

To directly compare agents operating in the simulated and real environments, the performance of agents in the experiment is also measured by the number n of episodes required to complete the removal task. In principle, the primary criterion for measuring the performance should be the time required to complete the manipulation task, but n is closely related to it (episodes may take more or less time depending on the length of the trajectory). Moreover, using the wall-clock time is rather meaningless, since the removal process was slowed down intentionally in the experiment to observe each action of the agent, e.g. to immediately detect changes in the tip apex.

Fig. 6.3 shows the performance of RL agents in the real-world removal task. The intrinsic stochasticity of RL is separated from the variations of the SPM tip apex (non-stationarity) between lifting trials, by plotting data points from experiments executed with identical tips in the same colour (Fig. 6.3a). If a tip was capable of removal in one experiment but failed in another, the respective data point is marked as 'agent fail'. If a tip was never able to achieve the removal task, the respective data point is marked as 'tip fail'. Note that in principle this could also be a failure of the agent.

The data clearly shows that the difficulty of the removal task depends on the tip, as discussed in section 6.2. For example, with tip D removal is easy, resulting in small n on average, while tip E, with which removal is more difficult, results in larger n.

A small force threshold of the tip-molecule bond reduces the fraction of successful trajectories. For particularly weak tips (labelled 'tip failure' in Fig. 6.3a), the removal task cannot be solved at all. For weaker (stronger) tips, larger (smaller) n, one would expect that successful trajectories cluster (scatter) stronger in space. Fig. 6.3b, in which we compare the xy coordinates of successful trajectories at $z = 2\,\text{Å}$ for tip D and tip E, clearly reveals this effect. The distribution of the corresponding xy coordinates for all tips (plotted as a grey-scale background) is rather broad and indeed similar to the distribution for the strong tip D. For the weak tip E, however, the agent has to pass through a very specific region in the xy plane to avoid bond rupture. This naturally explains why tip E tends to require a larger number n of episodes to succeed.

Fig. 6.3a also compares randomly initialised (R) agents with pre-trained (P) agents. R-agents start with random weights in the neural network, while P-agents have already solved the removal task for one particular tip. More precisely, a single R-agent was selected as a P-agent after completing its removal task, and training was continued on a new lifting trial (with different tip properties). The last executed trajectory of this R-agent is shown in Fig. 6.3c. Thus, all P-agents are initially identical, because they have the same experience and NN weights. On average, P-agents perform better than R-agents. This is evident both for the whole dataset and for individual tips, see for instance tip E. It clearly demonstrates that at least some knowledge about the removal task is universal and can be transferred to new tip configurations.

Fig. 6.3c reveals the nature of this universal knowledge. The xy coordinates of the rupture points s_T^- are plotted for R-agents (black) and P-agents (red). The data is limited to the first ten episodes of each experiment, where the difference in training and experience between the two types of agent is most significant. The plot shows that the randomly initialised agents explore all xy directions rather uniformly, while the pre-trained agents have a strong bias

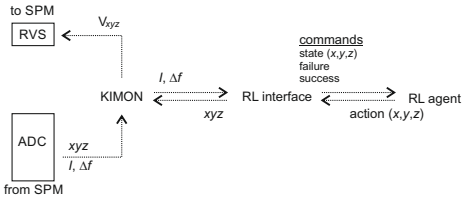

Figure 6.4: Sketch of the RL setup. Only the digital connections are shown.

towards the lower left quadrant ($x < 0$, $y < 0$) through which almost all successful trajectories pass (Fig. 6.3b). This bias is the essence of the universally valid policy which, once learned, gives P-agents a performance edge over R-agents.

6.4 Conclusion

The automated fabricating of complex metastable structures at the molecular level is a highly desirable goal. However, due to the limited observability and uncontrolled variability involved, this goal seemed out of reach until now. This proof-of-concept study shows, that autonomous robotic nanofabrication is indeed possible using RL without the need for human intervention. This was demonstrated on the prototypical task of removing a molecule from a H-bonded layer of PTCDA/Ag(111). Because the RL framework was used, it was not necessary to specify how the task was to be solved – only the goal had to be set, which is clearly easier. It was shown that an RL agent in full control of an SPM is not only capable of reaching a real manipulation goal within a moderate number of trials, but that it is moreover also robust enough to transfer a previously learned policy to new object systems. Furthermore, a strategy was discussed that would allow to (partially) recover the Markov property by integrating the experimental signals (I, Δf) into the state definition as well as into the RL model.

In conclusion, the dream of autonomous robotic nanofabrication is feasible. A natural next step would be to combine autonomous manipulation with image recognition, for additional automated detection of nanostructures for manipulation [79] and autonomous tip preparation [80, 81, 82].

6.5 Methods

6.5.1 Program scripts

The following scripts are used to control the SPM: RL agent (Python; written by: M. Esders, K. Schütt), RL interface (C#), and KIMON (C#; written by: T. Esat; modified by: author). Fig. 6.4 shows the digital data flow between the scripts. See section 2.3 for the analogue connections.

The agent is implemented in 'RL agent'. Fig. 6.1d shows a schematic of the neural network structure used and the processes for choosing an action. The agent sends the current action a_t to 'RL interface' for execution and receives a confirmation after the tip displacement has been performed. The agent then continues with the next action unless no additional control command is received, e.g. to notify the agent of a failure or success.

'RL interface' implements the logic for the automated execution of the experiment, communicates with the SPM hardware via KIMON, and provides a graphical user interface to control the lifting experiment. The experiment can be started or paused, and parameters can be set. These include the z distance for automated tip approach to (re-)establish a tip-molecule bond and the I threshold for switching from the initial amplifier gain of 5 to 8 during lifting. Gain switching was implemented to allow optimal detection of a tip-molecule bond rupture over a wide range of tip heights z in the I signal.

The primary mode of detection of a premature bond rupture is via the I signal, which drops off abruptly upon bond rupture (Fig. 6.1a). Beyond a z distance of 9 Å this detection starts becoming unreliable such that the Δf signal is additionally used. The experimenter verifies, by default, all automated failure (above 9 Å) and success (above 14 Å) signals by inspecting the behaviour of $\Delta f(z)$. This is to avoid passing any false information to the agent that would compromise the learning process. Specifically, observing the full peak-dip feature in the Δf signal indicates a success (see section 3.2.3).

6.5.2 Reinforcement learning and training details

The properties of the environment in which the RL agent must solve the manipulation task are summarized briefly: First, it is assumed that the task is stationary across a (small) number of episodes, e.g. the tip remains identical. If the tip changes during a lifting trial, the trial is aborted (and removed from the statistics). Second, the approximate state s corresponds to the Cartesian coordinates of the tip. Third, the tip is steered by five discrete actions (Fig. 6.1a), which also limits the state space to a finite number of states. Fourth, the reward is a combination of sparse reward ($r = -1$ on s_T^-, $r = +1$ on s_T^+) and slight reward shaping (default reward $r = +0.01$) to encourage higher lifting of the molecule before the termination of the episode. Fifth, future reward is discounted by $\gamma = 0.97$ to limit the agent's horizon.

The agent's goal is to maximise the expected return G_t, which is a function of the sequence of rewards $r_{t+1}, r_{t+2}, r_{t+3}, ...$ received after time step t. The simplest definition of the return would be a sum of the rewards $G_t = r_{t+1} + r_{t+2} + r_{t+3} + ... + r_T$. In this study, future rewards were discounted by γ and therefore the agent tried to maximise the expected *discounted* return:

$$\begin{aligned} G_t &= r_{t+1} + \gamma r_{t+2} + \gamma^2 r_{t+3} + ... \\ &= r_{t+1} + \gamma(r_{t+2} + \gamma r_{t+3} + ...) \\ &= r_{t+1} + \gamma G_{t+1} \end{aligned} \tag{6.3}$$

This recursive definition applies to all $t < T$. The expected return for a terminal state is defined as zero ($G_T = 0$), because no further states can be reached from there. Note that

G_t is fully defined by the information available at $t+1$.

The Q-function considers transitions from state-action pair (s_t, a_t) to state-action pair (s_{t+1}, a_{t+1}) and therefore evaluates G_t for state-action pairs. $Q(s_t, a_t)$ is the agent's estimate for the expected discounted return $G(s_t, a_t)$ for choosing action a_t in state s_t and following its policy π afterwards. The Q-function for a terminal state s_T is defined as zero ($Q(s_T, a_T) = 0$), similar to the definition of G_T.

A simple algorithm for updating the Q-values would be SARSA [70]. The loss function L (mean square prediction error) for training is computed as follows:

$$L^{\text{SARSA}} = [Q(s_t, a_t) - (r_{t+1} + \gamma Q(s_{t+1}, a_{t+1}))]^2$$

In this study, Expected SARSA [76] was used to train the agent. SARSA and Expected SARSA differ in the way they evaluate the successor state s_{t+1}. Expected SARSA considers the Q-values, $Q(s_{t+1}, a)$ and $a \in \mathcal{A}$, for all state-action pairs of the successor state s_{t+1}, while SARSA only evaluates $Q(s_{t+1}, a_{t+1})$ for a single action a_{t+1}. The loss is calculated as follows (as in eq. (6.2)):

$$L^{\text{Expected SARSA}} = \left[Q(s_t, a_t) - \left(r_{t+1} + \gamma \sum_{a \in \mathcal{A}} \pi(s_{t+1}, a) Q(s_{t+1}, a) \right) \right]^2$$

π is used to weight the contributions of $Q(s_{t+1}, a)$, with $a \in \mathcal{A}$ and $\sum_a \pi(s_{t+1}, a) \stackrel{!}{=} 1$ (see eq. (6.1)).

The agent in this study approximates the Q-function with a NN. The Double-Q-learning approach [83] was implemented to prevent overestimation of the Q-values [84] and instabilities during training [85], because of the use of a function approximator (here a NN). Double-Q-learning uses two networks: a 'live network' Q^{live} with network weights θ_i and a 'target network' Q^{target} with weights θ'_i. For one training step i a batch of 30 experience tuples $e_t = (s_t, a_t, r_t, s_{t+1})$ is drawn. The loss function L_i for the Q-value update of training step i is computed as follows:

$$L_i^{\text{Double-Q}}(s_t, a_t) = \left[Q_i^{\text{live}}(s_t, a_t) - \left(r_t + \gamma \sum_{a \in \mathcal{A}} \pi(s_{t+1}, a) Q_i^{\text{target}}(s_{t+1}, a) \right) \right]^2 . \tag{6.4}$$

During training, the Q-values predicted by the live network are adjusted by the target network, where the latter being updated only periodically (after every 200 training steps $\theta'_i \leftarrow \theta_i$). Note that, here, Expected SARSA is used instead of Q-learning.

The diagrams in Fig. 6.5 summarise the relationships relevant to a Q-value update or backup operation for the methods mentioned above: SARSA, Expected SARSA, and Q-learning.

To increase the training efficiency of the agent, two modifications were made to the standard RL algorithm: First, the Cartesian state definition was exploited for model-based RL during training (see section 6.2). Second, a rupture avoidance mechanism (see section 6.2) was introduced by using a negative temperature $T_{\text{train}} = -0.1$ during training to evaluate

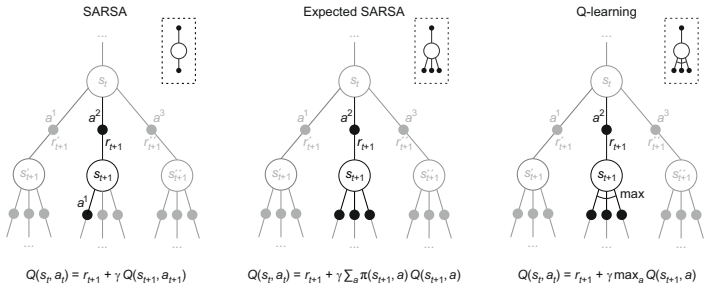

Figure 6.5: Backup diagrams for SARSA, Expected SARSA, and Q-learning. An example with three available actions per state is shown for each backup diagram (inset; reproduced from [70]) of each method. States are indicated by an open circle and state-action pairs by a solid circle. The experience tuple under evaluation is $e_t = (s_t, a^2, r_{t+1}, s_{t+1}, a^1)$ in all examples. The propagation of value information from $Q(s_{t+1}, a_{t+1})$ *back* to $Q(s_t, a_t)$ is defined according to the formula below each method. Note that Expected SARSA and Q-learning ignore the second action. They take all state-action pairs of the successor state into account, and either weight them by the policy π (Expected SARSA) or select the state-action pair with the highest Q-value (Q-learning). In this study, Expected SARSA was used to update the Q-values.

the policy π in L_i. During the experiment, the agent evaluated π with a positive temperature $T_{\text{act}} = +0.004$ to prefer actions with higher Q-values. Fig. 6.2d shows the increased performance due to the modifications for agents in a simulated environment (Fig. 6.2a). The experiments were conducted with agents combining both the model-based RL and the rupture avoidance mechanism.

The NN was only trained between episodes. This also allows simple comparison between a Q-value map of an episode and the corresponding manipulation trajectory (Fig. 6.2c), as all actions during the episode were chosen based on this map. The optimisation method was 'Adam' [86] with a constant learning rate of 10^{-3}. The number of training steps was increased over the first few episodes and then kept constant afterwards, starting from 200 steps to finally 2000 steps for the tenth episode and beyond. For one training step, a batch of 30 samples is drawn, where 10 % of the samples are drawn from the experience memory by prioritised experience replay [77] and 90 % are obtained from the environment model learned by the agent for model-based RL (see section 6.2).

6.5.3 Neural network architecture

The Q-function is approximated by a NN (Fig. 6.1d). The input layer of the Q-network consists of 3 neurons, receiving xyz tip coordinates. The second and third layers (hidden layers) consist of 30 neurons. The output layer consists of 6 neurons for A^{1-5} and V. V corresponds to the value of a state s_t and A^{1-5} is the advantage for choosing action a_t^{1-5}. The advantage for the action leading to s_{t+1} is higher (lower), if the Q-value for s_{t+1} is higher (lower) than for the other actions.

After the second layer, the network splits up into two separate streams, as inspired by the Dueling Network Architecture [75]. Therefore, each stream is assigned 15 neurons in the

third layer, which are either connected to A^{1-5} output neurons for the A-value stream or connected to a single V output neuron for the V-value stream.

The number of neurons in the hidden layers were reduced as much as possible, while maintaining optimal performance in the simulated environment.

CHAPTER 7

Scanning quantum dot microscopy as an application of controlled manipulation

7.1 Introduction

The controlled manipulation of molecules offers the possibility of creating functional devices. The simplest example of a functional single-molecule device created by controlled manipulation is the scanning quantum dot microscopy (SQDM) sensor. SQDM allows the quantitative characterisation of the electrostatic potential of adsorbates and assemblies on surfaces. It can provide essential benchmarks for identifying the correct functional for long-range forces in first principle calculations. This chapter gives an overview over the SQDM method (see section 7.2) and presents the results for the characterisation of the electrostatic potential over a closed PTCDA/Ag(111) monolayer (see section 7.3) and the paradoxical behaviour of molecular vacancies in such a layer (see sections 7.3 and 7.4). Two-contact manipulation allowed the construction of the SQDM sensor and the removal of molecules from the layer.

7.2 SQDM method

SQDM [38, 87, 88] allows to quantitative characterisation of lateral changes in the electric potential on a sample surface. More precisely, the potential is measured at a constant height z above the surface. The sensor is a QD and is attached to the SPM tip. By solving an inverse boundary problem in electrostatics, the measured potential in the *imaging plane* can be related back to the potential at the boundary - consisting of the substrate and tip surfaces which are connected at infinity [89, 90].

$$\Phi_{\mathrm{QD}}(\boldsymbol{r}) = -\frac{\epsilon_0}{e}\iint_{\mathrm{sample}}\left(\Phi_{\mathrm{S}}(\boldsymbol{r}') + V_{\mathrm{bias}}\right)\frac{\partial G(\boldsymbol{r},\boldsymbol{r}')}{\partial \boldsymbol{n}'}d^2\boldsymbol{r}' - \frac{\epsilon_0}{e}\iint_{\mathrm{tip}}\Phi_{\mathrm{S}}(\boldsymbol{r}+\boldsymbol{R})\frac{\partial G(\boldsymbol{r},\boldsymbol{r}+\boldsymbol{R})}{\partial \boldsymbol{n}'}d^2\boldsymbol{R} \tag{7.1}$$

is the equation for the potential Φ_{QD}, at the position r of a point-like QD, for a conducting sample and thus Dirichlet boundary conditions [89]. Φ_{S} is the potential at the surface of the boundary. $\boldsymbol{n}'$ is the surface normal at the boundary at $\boldsymbol{r}'$ (substrate) and $\boldsymbol{r}+\boldsymbol{R}$ (tip), and G is the Green's function with the condition $G(\boldsymbol{r},\boldsymbol{r}') = 0$ for $\boldsymbol{r}'$ on the boundary. Fig. 7.1a shows the spatial relationship of: $\boldsymbol{r}$, $\boldsymbol{r}'$, $\boldsymbol{n}'$, and $\boldsymbol{R}$.

The measurement principle of SQDM is to keep the potential $\Phi_{\mathrm{QD}} = \mathrm{const}$ during a scan by adjusting (and recording) V_{bias}, to compensate for local variations in Φ_{S} and changes in the sample topography. The goal is to calculate Φ_{S} by inverting eq. (7.1) for a chosen boundary shape. This process is also called deconvolution. Its accuracy depends on the representation of the boundary.

Before calculating Φ_{S}, some simplifications can be made: First, it is reasonable to approximate the last term in eq. (7.1) as a constant Φ_{T}, since the QD has a fixed position relative to the tip and both are far enough away from the sample [89]. Note that this also excludes any changes in the charge distribution on the tip surface during SQDM, e.g. moving charges (adsorbates) on the tip surface. Thus, Φ_{S} corresponds from now on directly to the desired potential on the sample surface. Second, the choice of a planar sample surface as the boundary already provides excellent results when the topography $t_{\mathrm{d}} \ll z$ [90]. Third, the tip is assumed to be axially symmetric.

With the above assumptions $\partial G/\partial \mathrm{n}'$ depends only on the relative distance $|\boldsymbol{r}_\parallel - \boldsymbol{r}'_\parallel|$ to the QD in the imaging plane at z (parallel to the sample surface). It becomes the Point Spread Function (PSF) $\gamma(|\boldsymbol{r}_\parallel - \boldsymbol{r}'_\parallel|, z) \equiv -\epsilon_0/e \cdot \partial G/\partial \mathrm{n}'$. The explicit reference to z will be dropped in the future.

$$\Phi_{\mathrm{QD}}(\boldsymbol{r}_\parallel) = \left(V^*(\boldsymbol{r}_\parallel) + V_{\mathrm{bias}}(\boldsymbol{r}_\parallel)\right)\alpha(\boldsymbol{r}_\parallel) + \Phi_{\mathrm{T}} \tag{7.2}$$

becomes the new eq. (7.1) using γ to define α and V^* as

$$\begin{aligned}\alpha(\boldsymbol{r}_\parallel) &= \iint_{\mathrm{sample}}\gamma(|\boldsymbol{r}_\parallel - \boldsymbol{r}'_\parallel|)d^2\boldsymbol{r}'_\parallel = \frac{\partial\Phi_{\mathrm{QD}}(\boldsymbol{r}_\parallel)}{\partial V_{\mathrm{bias}}(\boldsymbol{r}_\parallel)}\\ V^*(\boldsymbol{r}_\parallel) &= \iint_{\mathrm{sample}}\Phi_{\mathrm{S}}(\boldsymbol{r}'_\parallel)\gamma^*(|\boldsymbol{r}_\parallel - \boldsymbol{r}'_\parallel|)d^2\boldsymbol{r}'_\parallel\end{aligned} \tag{7.3}$$

where V^* quantifies the effect of the surface potential Φ_{S} on the QD, the gating efficiency α, the normalised PSF $\gamma^* = \gamma/\alpha$, and the contribution of charges at the tip Φ_{T}.

Primary and secondary measurands

Two conditions have to be met in order to use SQDM: First, the QD has to be small enough that the coulomb blockade allows only a single electron to transfer between the QD and the tip at a specific Φ_{QD}. Such a tunnelling event causes a sharp dip in the Kelvin parabola,

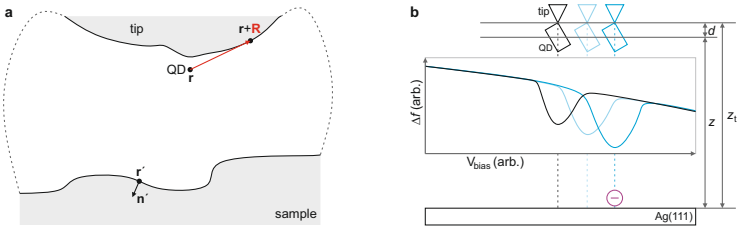

Figure 7.1: Spatial relationships and measurement principle of SQDM. **a**, Schematic of the spatial relationship between sample, QD, and tip. $\boldsymbol{r}'$ are points on the sample surface. $\boldsymbol{n}'$ is the surface normal at $\boldsymbol{r}'$. The QD is fixed to the tip and at position $\boldsymbol{r}$. The relative position between $\boldsymbol{r}$ and $\boldsymbol{r}+\boldsymbol{R}$, points on the tip surface, are thus fixed during scanning and fully described by $\boldsymbol{R}$ (red arrow). Dashed lines indicate electrical connection of tip and sample at infinity. **b**, Schematic of the measurement principle of SQDM at the example of Φ^+. An additional negative charge (purple) is placed on the sample surface. The closer the distance between QD and the charge on the surface, the more V_{bias} is needed to compensate for Φ_{S} to maintain Φ^+. QD positions and corresponding Δf spectra are indicated by colour.

which indicates correct compensation of V^* by V_{bias}. Fig. 7.1b shows a schematic of three colour-coded tunnelling events for Φ^+ at different lateral tip positions and $V_{\text{bias}} > 0$. Second, two charge state changes of the QD at $\Phi_{\text{QD}} = \Phi^{\pm}$ have to be detected by the setup.

Here, the organic molecule PTCDA is used as a QD. The tunnelling events occur at negative and positive V_{bias}, which will be referred to as $V_{\text{bias}} = V^{\pm}$. Experimentally, $V^{\pm}$ are defined as the minima of the tunnelling dips in the Δf signal.

$V^{\pm}$ are the primary measurands of SQDM. An SQDM image requires two images of the same area. One for the lateral variations of V^- and one for V^+. Then, V^* can be calculated relative to a reference point at r_0 as will be shown below. All variables measured at r_0 have a zero as their lower index. Note that for imaging $V^{\pm}$, a feedback controller was developed to maintain $\Phi^{\pm}$ during scanning. It tracks a fixed Δf on the inner flanks (those closer to $V_{\text{bias}} = 0$) of the tunnelling dips and adjusts V_{bias} accordingly [89].

With two versions of eq. (7.2) evaluated at r_0 and at any other position follows:

$$\begin{aligned} \Phi_0^{\pm} &= \left(V_0^* + V_0^{\pm}\right)\alpha_0 + \Phi_{\text{T}} \\ \Phi^{\pm}(\boldsymbol{r}_{\parallel}) &= \left(V^*(\boldsymbol{r}_{\parallel}) + V^{\pm}(\boldsymbol{r}_{\parallel})\right)\alpha(\boldsymbol{r}_{\parallel}) + \Phi_{\text{T}}. \end{aligned} \tag{7.4}$$

After defining $V_0^* = 0$ and some simple algebra (see chapter B), the secondary measurands α_{rel} and V^* are derived directly from the experimental observables $V_0^{\pm}$ and $V^{\pm}$:

$$\alpha_{rel}(\boldsymbol{r}_{\parallel}) = \frac{\alpha(\boldsymbol{r}_{\parallel})}{\alpha_0} = \frac{V_0^+ - V_0^-}{V^+(\boldsymbol{r}_{\parallel}) - V^-(\boldsymbol{r}_{\parallel})} \tag{7.5}$$

$$V^*(\boldsymbol{r}_{\parallel}) = \frac{V_0^-}{\alpha_{rel}(\boldsymbol{r}_{\parallel})} - V^-(\boldsymbol{r}_{\parallel}). \tag{7.6}$$

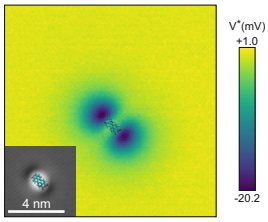

Figure 7.2: Measuring the electrical potential of an isolated PTCDA on Ag(111). The SQDM V^* (STC controller, $z_{tip} = 24.4\,\text{Å}$). The inset shows the STM topography of an isolated molecule (setpoint: 0.35 V, 0.2 nA). The orientation of the molecule is indicated in both the inset and the V^* image.

7.3 Experiment and results

To characterise the electrostatic potential of molecule vacancies, a PTCDA/Ag(111) sample was prepared (see section 2.3), single and double PTCDA vacancies were created by 3D manipulation (see section 3.3), and the removed molecules were deposited back onto the clean Ag(111) surface (see section 3.2.3). One of the deposited molecules was then attached to the SPM tip as SQDM sensor by vertical manipulation and tested by observing a tunnelling event (Fig. 7.1) over Ag(111).

Before characterising molecule vacancies in a PTCDA layer with SQDM, it is insightful to first characterise an isolated PTCDA and a closed layer at molecular resolution. It is known that SQDM is able to resolve a potential contrast between rows of type A and B molecules, but molecular resolution has not been achieved yet [89].

SQDM of isolated PTCDA on Ag(111)

Electrostatically, PTCDA on Ag(111) consists of an in-plane quadrupole overlaid with an out-of-plane dipole. The quadrupole consists of the four negatively charged O_{carb} and the positively charged H along the long edges of PTCDA. The dipole results from the charge transfer from the Ag(111) surface to the backbone of the molecule (see section 3.2.2).

Fig. 7.2 shows the SQDM V^* of an isolated PTCDA. Indeed, the quadrupole is clearly visible. The dipole is recovered by integrating the V^* image and results in a dipole moment of $-0.63\,\text{D}$. This is close to $-0.65\,\text{D}$ determined in [89] and is influenced by the measurement area (has to show full saturation of V^*) and the background correction (tilt, etc.). Here, a line-by-line background correction was applied. The area required for integration can be reduced by deconvolution of V^* (see section 7.2).

SQDM of closed PTCDA/Ag(111) monolayer

Achieving molecular resolution over the layer in V^* with SQDM is difficult. The onset of field emission is beyond Φ^+ for large z. However, at the distances required here, field emission starts when Φ^+ is reached. It is therefore necessary to make a compromise between resolution and the risk of electron radiation damage (e.g. top left in Fig. 7.3) of the layer. In order to

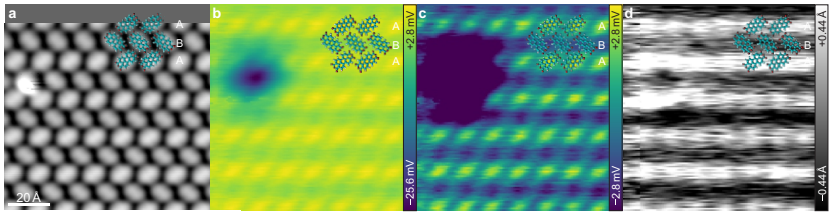

Figure 7.3: Measuring the electrostatic potential over a PTCDA on Ag(111) layer containing a defect (damaged molecule B by field emission). The overlay shows the molecular structure and molecule A and B are indicated. **a**, STM topography of PTCDA/Ag(111) monolayer (setpoint: 0.35 V, 0.2 nA). **b**, and **c**, SQDM V^* images (STC controller) with full contrast range emphasizing the defect in **b** and limited range emphasizing the intralayer contrast in **c**. **d**, Corresponding dielectric topography image of $t_\mathrm{d} = (\alpha_{rel} - 1)/g$ [89]. g was estimated from calibration measurements to be $g \approx 0.08\,\text{Å}^{-1}$.

achieve the molecular resolution demonstrated in Fig. 7.3, the distance between the tip and the sample was gradually reduced through an iterative process. The V_bias at which Φ^+ occurs at a specific z height depends on the shape of the tip apex and the bonding of s-PTCDA to it. A tip-molecule configuration which shows Φ^+ at a lower V_bias reduces the risk of filed emission (damage). Field emission is not observed for Φ^- due to the tunnelling direction of electrons from the blunt sample surface to the tip at negative V_bias.

The measured V^* above a monolayer of PTCDA on Ag(111) (Fig. 7.3) shows a weak contrast between rows consisting of molecules of type A and B. Type A molecules have a more positive potential than type B molecules. Note that the contrast range is only a few mV for Fig. 7.3c. The potential over a molecule backbone is more positive than over the O_carb, but the difference is much smaller compared to an isolated molecule (Fig. 7.3c). The quadrupole of an isolated molecule (Fig. 7.2) is (nearly) compensated by the formation of H-bonds, resulting in the herringbone structure of the monolayer. For more information on the alignment process of the STM topography and the SQDM images see chapter C.

The difference in contrast between the rows can be explained by a different charge transfer from the Ag(111) substrate to the molecules of type A and B, resulting in different dipoles perpendicular to the surface (including the image charge). Due to the interaction with the substrate, the LUMO of PTCDA in the gas phase is pulled below the Fermi energy of the Ag(111) substrate upon adsorption. The former LUMO of molecule B is about 160 mV lower than that of molecule A [35, 51]. Therefore less (more) charge is transferred to the molecule A (B), which is in line with the finding of a more (less) positive potential for A (B).

Fig. 7.3d shows the dielectric topography t_d of the effective metallic surface. The height difference is $\Delta z_{t_\mathrm{d}} \approx 0.63\,\text{Å}$ between rows of molecule A and B. Molecule A is further away from the surface, as expected, because t_d shows the same sign as STM topography ($\Delta z_{t_{STM}} \approx 0.10\,\text{Å}$). In a complimentary measurement to STM, by pushing with a CO-terminated tip into the PTCDA/Ag(111) layer and fitting the minima of the Δf approach spectra, a height difference of 0.05 Å was determined (see section 4.2, Fig. 4.6). The comparison reveals that t_d shows a more pronounced contrast between rows than the geometric topography. Interestingly, the SQDM signal is also dominated by t_d and should be investigated further.

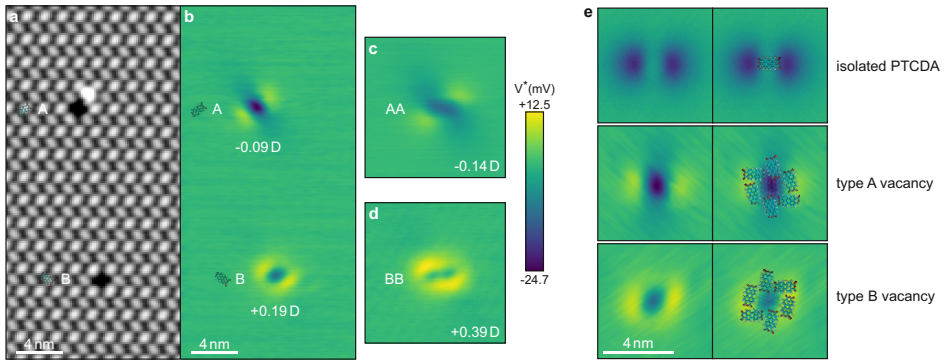

Figure 7.4: Measurement of the electrostatic potential over molecule vacancies in a PTCDA on Ag(111) monolayer and its comparison to the potential over an isolated PTCDA. The orientation of the molecules, the vacancy types and the corresponding measured dipole moments are indicated. **a**, STM topography of layer with type A and B vacancy (setpoint: 0.35 V, 0.2 nA). SQDM V^* images of molecule vacancies (STC controller): **b**, two single molecule vacancies of type A (top) and B (bottom, $z_{tip} = 25.5$ Å), **c**, double vacancy of type AA ($z_{tip} = 27.8$ Å), **d**, double vacancy of type BB ($z_{tip} = 27.2$ Å). Line-by-line correction was applied to all V^* images to remove the background from the PTCDA layer. All V^* images share the same contrast range indicated on the right. Note that **c**, **d** look fainter than **b** because **b** was recorded closer to the surface. Note also the field emission damage visible in **a**. It occurred during the recording of V^+ of **b** and could be corrected by filling the affected area with an average value of the layer background signal. V^- was unaffected because it was recorded before V^+. **e**, Comparison of V^* of isolated molecule (Fig. 7.2, ($z_{tip} = 24.4$ Å) with V^* of vacancies of type A, B. Each image is rotated such that the long axis of the centre (missing) PTCDA is orientated horizontally. On the right is the V^* image from the left superimposed with the molecular structure. The removed molecules are shown as transparent.

SQDM of single and double PTCDA vacancies

The electrical potential difference between a bare Ag(111) surface and Ag(111) covered with a closed layer of PTCDA molecules, known from experiments, is around 150 mV [89]. The expected average contribution per molecule is therefore −0.45 D [89]. The intricate interplay of intermolecular and dipole-dipole interactions in an island lead to the reduction from −0.65 D for an isolated molecule to −0.45 D. For a single missing molecule in a PTCDA layer, one would naively expect the opposite dipole of +0.45 D.

Fig. 7.4 shows the SQDM V^* for single and double vacancies of type: A and B (Fig. 7.4b), AA (Fig. 7.4c), BB (Fig. 7.4d). A single vacancy looks similar to the (inverted) V^* of an isolated PTCDA molecule on the surface (Fig. 7.4e). This is expected, because the quadrupole moment of a molecule in the layer is compensated by positively charged H and negatively charged O from its surroundings, which are exposed when the molecule is removed. The V^* contrast of a double vacancy looks similar to that of single vacancy. It appears to be just a repetition of the single vacancy contrast next to each other.

To evaluate the dipoles of the vacancies (Fig. 7.4), the measured V^* of type A, B, AA and BB vacancies were integrated over an area showing at least full saturation of the vacancy contrast. To remove the background, a line-by-line correction was applied. For each line,

the average value of the first and last four pixels was subtracted. The resulting dipoles are: $-0.09 \pm 0.01\,\mathrm{D}$ (A), $0.19 \pm 0.01\,\mathrm{D}$ (B), $-0.14 \pm 0.02\,\mathrm{D}$ (AA), $0.39 \pm 0.01\,\mathrm{D}$ (BB).

The measured dipoles are much smaller than naively expected. For type B, the value is more than halved compared to the (naively) expected $0.45\,\mathrm{D}$ for a single vacancy. Even more surprisingly, for type A the dipole points in the opposite direction. The unequal behaviour of type A and B vacancies can be clearly seen in Fig. 7.4b, as type A appears to be more negative than B.

A reduction can be explained by the rearrangement of charge due to the presence of the vacancy. The charge transfer from the surface to an isolated molecule (dipole of $-0.65\,\mathrm{D}$) is greater than for a molecule in the layer (dipole of $-0.45\,\mathrm{D}$). Thus, the presence of neighbouring PTCDA molecules reduces the charge transfer. Conversely, one may expect that the charge transfer to a molecule in the layer increases with the number of missing (next) neighbours. Under the simple assumption that removing all six nearest neighbours would negate the effects of the layer, this would result in an additional charge transfer of $-0.2\,\mathrm{D}$ to said molecule with $-0.2\,\mathrm{D} \cdot 1/6$ per vacancy. The expected additional contribution to the total dipole from the surrounding molecules in case of a single PTCDA vacancy is $-0.2\,\mathrm{D} \cdot 1/6 \cdot 6 = -0.2\,\mathrm{D}$, as each vacancy is surrounded by six molecules. This reduces the expected dipole for a PTCDA vacancy to $+0.25\,\mathrm{D}$ and is remarkably close to the finding for the type B vacancy.

The different behaviour of type A and B vacancies is unexpected, because the surrounding molecules are identical PTCDA which therefore have the same intrinsic quadrupole and similar charge transfer from the surface. However, a vacancy of type A (B) is always surrounded by four molecules of the opposite type B (A).

The difference in charge transfer from the surface to molecules A and B is not sufficient as an explanation. On the one hand, it points in the correct direction - the more negative (positive) vacancy A (B) is surrounded by additional negative (positive) potential from type B (A) molecules. On the other hand, the potential difference between type A and B is about $3\,\mathrm{mV}$ (Fig. 7.3c) and small compared to the potential difference of $150\,\mathrm{mV}$ between a PTCDA layer and the bare Ag(111) surface. Therefore some other effect has to be responsible for the strong reduction of the vacancy dipole.

Analysis: Separated PTCDA vs. single molecule vacancy

To further analyse the paradoxical behaviour of the (type A) PTCDA vacancies, the potential above the vacancies is directly compared with the potential above an isolated PTCDA molecule.

Fig. 7.5 shows line profiles through the V^* images of isolated PTCDA molecules and single molecule vacancies (Fig. 7.4b), measured at similar SPM tip heights. Both types of vacancies in the same SQDM image ensure the same properties for the combination of sensor molecule and SPM tip, when comparing type A and B vacancies of the same height. The profiles were extracted along the two high symmetry directions of the V^* signal. They are referred to as: direction 1 and 2. For isolated PTCDA, the profile lines correspond with the long and short axis of the molecule (Fig. 7.5a). Three lines, each 1 pixel apart, were averaged to form a profile. And each line was extracted using cubic interpolation.

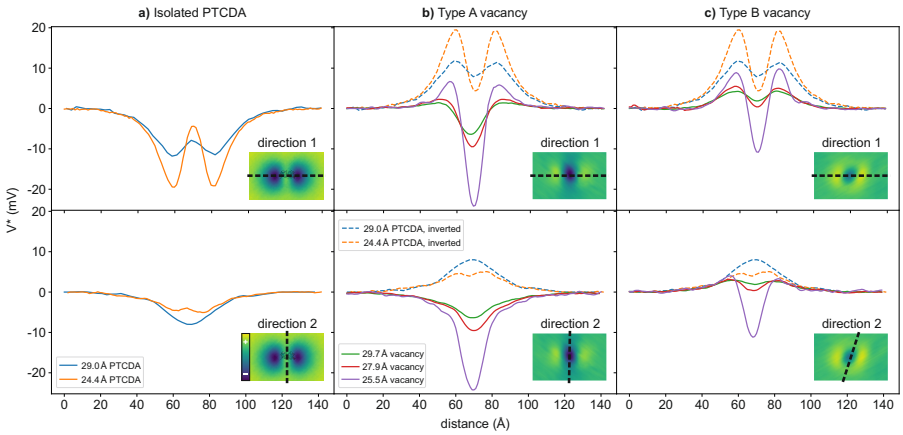

Figure 7.5: V^* line profiles of PTCDA/Ag(111) measured at different SPM tip heights. Profiles from left to right for: **a**, isolated PTCDA, **b**, type A vacancy, **c**, type B vacancy. The V^* profiles for type A and B vacancies at one height were extracted from the same SQDM image. The inverted PTCDA profiles (dashed lines) are plotted together with the vacancy profiles for direct comparison. The profile direction is indicated by the inset (taken from Figs. 7.2 and 7.4b).

Fig. 7.5a shows the profiles for an isolated PTCDA molecule. Direction 1 (long axis) shows an in-plain quadrupole overlaid with an out-of-plane dipole. The quadrupole results from the negatively charged O_{carb} atoms and positively charged H atoms. The effect of the quadrupole becomes more pronounced as the distance between the sensor and the surface decreases. This is expected, due to the faster decay of the quadrupole potential with distance compared to the dipole potential. However, the fact that the full quadrupole is pulled down to negative V^* values is the result of the charge transfer from the surface to the PTCDA backbone (see section 3.2.2) and its corresponding out-of-plane dipole. Direction 2 (short axis) shows mainly the dipole as the profile crosses the PTCDA backbone.

The V^* profiles of type A and B vacancies in Fig. 7.5b,c show the expected dipole and quadrupole shapes. In contrast to an isolated molecule, the quadrupole of the vacancy comes from the partial charges of the unpaired H and O_{carb} atoms of the surrounding molecules. A closer inspection, however, reveals significant deviations from the inverted V^* profiles of isolated PTCDA.

The profiles of type A vacancies (Fig. 7.5b) show two interesting deviations. First, direction 1 shows a quadrupole offset by a smaller dipole compared to isolated PTCDA. Second, direction 2 shows a stronger dipole. But surprisingly, both type A vacancy dipoles point in the *same* direction as the dipoles for isolated PTCDA! They are not inverted, as would be expected, compared to the case of isolated PTCDA. These deviations explain the paradoxical result of a negative dipole moment for the type A vacancies.

Type B vacancies (Fig. 7.5c) also deviate from the behaviour of isolated PTCDA. Here, both directions show a quadrupole offset by a dipole, and the dipole is in the expected

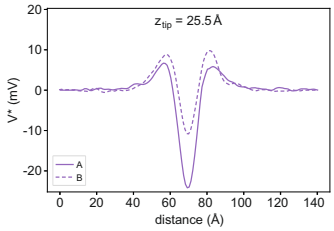

Figure 7.6: Direct comparison of profiles for type A and B vacancies along direction 1.

direction. While the vacancy and isolated PTCDA dipoles are comparable for direction 2, the type B vacancy dipole is very weak (to non-existent for the profile closest to the surface) in direction 1. The latter explains why the found dipole moment for type B vacancies is weaker than expected.

Fig. 7.6 compares the dipoles and quadrupoles of type A and B vacancies for the profiles measured closest to the surface in Fig. 7.5. One can clearly see that the quadrupole for type A is offset by a negative charge, while (almost) no offset is visible for type B. This is under the reasonable assumption that the quadrupoles are similar for type A and B vacancies.

7.4 Detailed analysis of the vacancy potential paradox

The paradoxical behaviour of PTCDA vacancies could be better understood by comparing the potential of type A and B vacancies with isolated PTCDA molecules, as shown above. However, the physical origin, hidden in the intermolecular interaction and molecule-surface interactions, is still unknown. This section gathers additional knowledge on PTCDA vacancies to aid (future) investigation.

Molecule orientation

The main asymmetry between the two types of single vacancies, that type A (B) is surrounded by four type B (A) molecules.

The unit cell of PTCDA/Ag(111) is nearly rectangular, sheared by only 1° (see section 3.2.2). Therefore, there is only a slight distortion between the orientations of molecules surrounding molecules A and B (and thus the vacancy). Also the difference in the electrical dipole between A and B molecules is small (see section 7.3).

What has not been taken into account so far is a (very likely) structural relaxation of the molecules surrounding a vacancy, compared to a closed layer. Here, the adsorption position of A and B molecules could play a role. Note that a change in the rotation of the molecules is not expected. This would be visible in the STM topography. However, other effects are possible, for example a change in the adsorption height (which would affect charge transfer from the surface). Note also that the O_{carb} bond itself is quite flexible (Fig. 4.8).

The O_{carb} of molecule A adsorbs on top of Ag atoms of the underlying Ag(111) substrate,

unlike the case of molecule B (see section 3.2.2). Thus, molecule A is likely to be more strongly bound to the surface than molecule B. This is also supported by DFT calculations [59]. Following this argument, type A molecules would be more structurally constrained to counteract the vacancy dipole by relaxation. Indeed, the measured dipole of a type A vacancy (−0.09 D) surrounded by four type B molecules is almost completely compensated, while it remains for a type B vacancy (+0.19 D) surrounded by four type A molecules. The observation that the angle between direction 1 and 2 of the V^* signal for a type A vacancy is around 90° and therefore more similar to an isolated PTCDA molecule than a type B vacancy (Fig. 7.5) also supports that the surrounding type A molecules are more structurally constrained than type B molecules. Still, an overcompensation of the dipole in the opposite direction remains puzzling.

The vacancy structure could be further investigated, for example, by scanning tunnelling hydrogen microscopy (STHM) [55] or high-resolution AFM [56] and supported by DFT calculations.

Activation of molecules around a vacancy

Recording the STM topography of type A and B vacancies at different V_{bias} gives insight into their spectroscopic properties and could help to identify unique states around the vacancy.

Nothing unusual is seen in the topography of a PTCDA monolayer containing type A and B vacancies, when recorded at a common V_{bias} of −0.35 V and 0.35 V. The topography shows the former LUMO at −0.35 V (Fig. 7.7a). At 0.35 V (Fig. 7.7b) the topography signal is more aligned with the structure of the molecule. The insets in Fig. 7.7b show a magnification of the vacancies. The areas of lower density of states, close to the O_{carb} pointing in the vacancy, are visible, similar to island edges and isolated PTCDA on the Ag(111) surface.

A change in the brightness of the molecules around the vacancies can be observed when recording at $V_{\text{bias}} = 0.7V$ (Fig. 7.7c). This V_{bias} is at the onset of the delocalised LUMO+1/+2 state of PTCDA the Ag(111) surface (see section 3.2.2). Four of the six molecules surrounding a vacancy appear brighter than the corresponding molecules in the closed PTCDA/Ag(111) layer.

The change in brightness corresponds to a higher integrated density of states. It is induced by the presence of a molecule vacancy or, in other words, activated by the removal of a molecule from the surface. Therefore, the four molecules with higher density of states (at around 0.7 V) surrounding a vacancy will be referred to as activated molecules.

The activated molecules from pairs of molecules A and B, which are separated by two 'normal' molecules A (B) for a type B (A) vacancy. No activation is seen for the two molecules with both O_{carb} pointing into the vacancy.

A comparison between Fig. 7.7c and the corresponding V^* (Fig. 7.7d) reveals a correlation between the position of activated molecules and the shape of the V^* contrast of vacancies. It appears that V^* is more positive at positions of activated molecules and more negative along the direction of the two non-activated molecules around a vacancy.

Fig. 7.8a-c show topography images of double vacancies, showing the activated molecules, and Fig. 7.8d,e show the corresponding V^* images. They confirm the correlation between

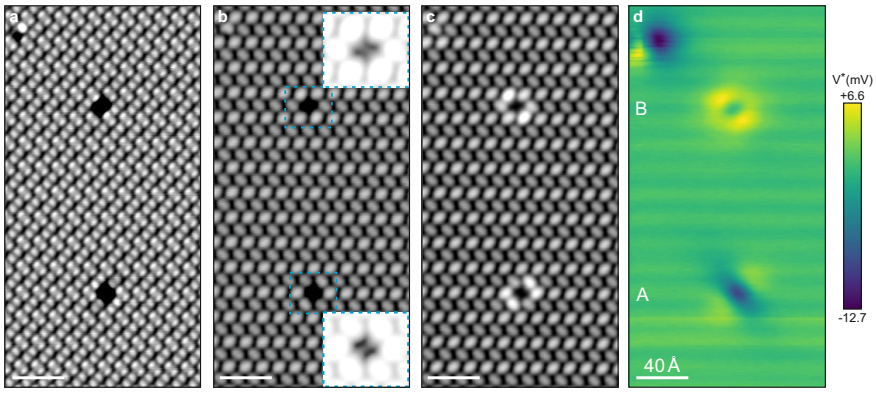

Figure 7.7: STM topography and electrical potential of type A and B vacancies for the same area. The topography images ($I = 0.2\,\mathrm{nA}$) were recorded after **d** and at: **a**, $-0.35\,\mathrm{V}$, **b**, $0.35\,\mathrm{V}$, **c**, $0.7\,\mathrm{V}$. The insets in **b** show a magnification of the indicated areas with enhanced contrast in the vacancy. **d**, V^* measured at $z^{tip} = 27.9\,\text{Å}$ with STC controller. Also a damaged molecule from field emission (top left) and the contrast between rows is visible. Rows of molecule A and B and the image scale are indicated. The surface area recorded in **d** is slightly shifted to the left compared to **a-c**.

STM topography and SQDM V^* and show the modification of activated molecules around a vacancy by a neighbouring vacancy.

As a side note, Fig. 7.7 also shows the topography and V^* of a molecule damaged by field emission during one recording of an SQDM image. This damage is clearly visible in V^*. It is also visible in the topography image showing the former LUMO, but only close inspection reveals the damage in the other images. The unambiguous, high sensitivity to defects is an advantage of the SQDM method.

The activation of molecules upon vacancy creation is an interesting concept and could be useful for the construction of a cellular automata as demonstrated by Kocić at al. in [74].

A basic cellular automata consists of cells with at least two states (e.g. a logical 0 and 1) arranged in a regular grid. It is also required that neighbouring cells can interact with each other for data processing.

Kocić et al. show a proof-of-principle demonstration of a molecular quantum cellular automata (QCA) in [74]. They use a molecule as a cell and self-assembly of the monolayer on the metal substrate ensures the regular grid. When a molecule is removed, the two neighbouring molecules along its long axis are activated. They therefore exhibit a characteristic STS signal. Further, neighbouring active cells can interact with each other and rich patterns are possible by a clever vacancy design.

The conditions for a QCA are very similar for PTCDA/Ag(111). PTCDA also receives charge transfer from the Ag(111) surface and molecule activation has been demonstrated above. The controlled creation of tailored vacancy patterns is also possible (see chapters 3 and 6). Moreover, with the unit cell consisting of two different molecules A and B, a higher variation of interaction patterns can be expected (compared to [74] with equal molecules).

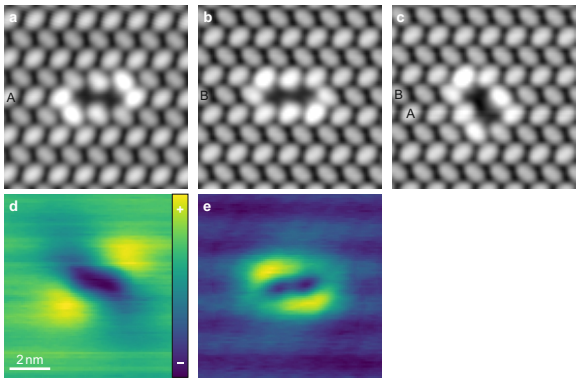

Figure 7.8: STM topography and electrical potential of double vacancies. STM topography of double vacancies: **a**, type AA vacancy, **b**, type BB vacancy, **c**, type AB vacancy. Molecule A and B are indicated. Corresponding SQDM V^* of double vacancies: **d**, type AA, **e**, type AB. The scale and V^* contrast are indicated in **d**. The contrast is maximized for each image separately. Note that the V^* of **d** and **e** are based on the same data as Fig. 7.4c,d without line-by-line background correction.

Spectroscopy of type A vacancy

This section analyses STS data of a type A vacancy recorded by A. Sabitova. The STS spectra were recorded in an 85x85 grid in an area of 110x110 $Å^2$ with feedback on between grids (setpoint: -0.35 V, 0.1 nA). The STS spectra will improve the insight into the paradoxical behaviour of type A vacancies as well as the activation of molecules around a vacancy.

Fig. 7.9a shows slices through the I signal of the grid in the range of -100 mV to 1100 mV. Only a portion of the grid around the vacancy is shown in the slices. The grid was rotated to match the orientation of the molecules in Fig. 7.7. The I in a recorded spectrum is proportional to the integrated DOS. Care must be taken when interpreting the contrast within a I slice as the relative integrated DOS between spectra due to the height adjustment of z_{tip} for each spectrum (feedback is on between spectra). z_{tip} should be similar over the molecules, but the tip is naturally much closer to the surface over the vacancy.

The vacancy shows slightly less integrated DOS than the molecule cores in the layer at -100 mV. No unique states are visible for the molecules surrounding the type A vacancy compared to the layer.

At positive bias, a vacancy state appears around 50 mV and dissolves around 1100 mV. After 450 mV the molecules surrounding the vacancies also start to show higher integrated DOS compared to the layer. The corresponding slices are shown in Fig. 7.9a.

Fig. 7.9b,c show spectra at the indicated positions (see insets). The four coloured spectra are around the type A vacancy, the other two spectra are reference spectra of molecules A (silver) and B (grey) in the layer. The molecules around a vacancy consist of three pairs with the same spectroscopic response due to rotational symmetry. The three unique molecules will be referred to by molecule type and colour of the spectrum: A-red, B-magenta, B-blue. The yellow spectrum was recorded above the vacancy centre. The spectra in Fig. 7.9b were

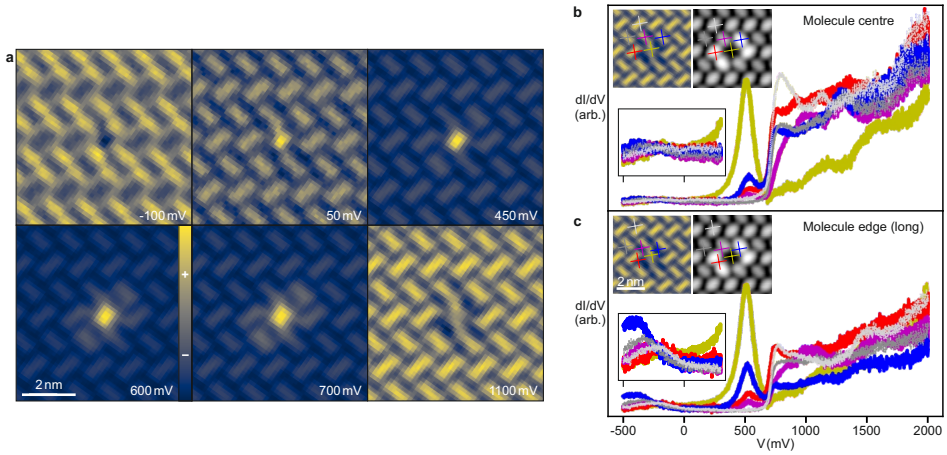

Figure 7.9: Slices and individual spectra of 85x85 spectra recorded in a grid around a type A vacancy. **a**, Slices through the I signal of the grid (left to right, first top then down): −100 mV, 50 mV, 450 mV, 600 mV, 700 mV, 1100 mV. Note that feedback is on between spectra, setpoint: −0.35 V, 0.1 nA. The tip is therefore closer towards the surface over the vacancy than over the layer. The scale and contrast are indicated. The contrast was optimized separately for each slice. **b**,**c**, dI/dV spectra of the indicated positions in the insets. The upper two insets (left to right): section of the 1100 mV slice (**a**), STM topography (setpoint: 0.7 V, 0.2 nA; section of Fig. 7.7c). The lower inset shows a magnification of the spectra in the range of −500 mV to 300 mV.

recorded above the centre of the molecules. The spectra in Fig. 7.9c were recorded above the long edge of the molecule, where the former LUMO is visible at negative bias voltage.

Close inspection of the former LUMO in Fig. 7.9c reveals that A-red and B-magenta behave similarly to the corresponding reference spectra of molecule A and B. However, B-blue shows an increased DOS as well as a shift of the LUMO state to lower V_{bias}. Both observations should lead to an increased charge transfer from the surface to the B-blue molecules. On close inspection, the shift of the LUMO to lower V_{bias} is even visible in Fig. 7.7a, as the B-blue molecules of the type A vacancy appear slightly darker than other B molecules in the layer at $V_{\mathrm{bias}} = -0.35$ V. No such change in contrast can be observed for the type B vacancy in the same image.

The vacancy state is clearly visible at around 500 mV in the dI/dV spectra in Fig. 7.9b,c (yellow spectrum). It behaves similarly to the spectra recorded over the centre of the molecules at negative V_{bias} (Fig. 7.9b). Also, the vacancy behaves spectroscopically similar to a PTCDA core in the layer in the range of −500 mV - 0 mV (Fig. 7.9b). It is likely that some molecule states extend into the vacancy, considering that the tip is much closer to the surface over the vacancy and thus the measured DOS is much weaker compared to the molecules.

Summarizing, the increased DOS for the LUMO of B-blue molecules and its shift to negative V_{bias}, and thus potentially higher charge transfer from the surface, could explain the

observation of an almost neutral but slightly negative dipole moment for a type A vacancy. This would also explain that the positive part of the V^* signal is weaker for a type A vacancy in comparison to type B (Fig. 7.4b, Fig. 7.7d). As the unpaired positively charged H atoms of B-blue pointing into the vacancy contribute to the positive signal, the additional charge transfer to B-blue could therefore explain the observed reduction in signal strength.

The spectra in Fig. 7.9b,c also explain the origin of the molecule activation around a vacancy. The vacancy state extends into all six of the surrounding molecules. Also the brightness in an STM topography image at 0.7 V of the activated molecules corresponds to the DOS of this state on the molecules (e.g. inset in Fig. 7.9b). B-blue is the brightest and has the highest DOS around 500 mV, followed by A-red. B-magenta has a similar brightness as other B molecules in the layer and shows only a small increase in DOS due to the vacancy state.

7.5 Summary and discussion

Two-contact manipulation was used to construct a sensor for characterising the local electrostatic potential on the sample surface. Namely, a single molecule was attached to the SPM tip in a specific configuration to serve as a quantum dot for SQDM.

The high sensitivity of SQDM allowed the characterisation of V^* of a PTCDA/Ag(111) monolayer, with molecular resolution and thus allowed mapping to the STM topography, as well as of single and double molecule vacancies in such a layer. Such measurements are valuable benchmarks for theoretical calculations. They are difficult to predict due to the importance of long-range forces.

It is interesting to note that the dipole moment per molecule in a PTCDA/Ag(111) monolayer is only slightly weaker than for an isolated molecule. However, the quadrupole of a molecule is almost completely compensated by the herringbone structure of the layer (see the weak intralayer contrast of only a few mV in Fig. 7.3c).

The results for single and double molecule vacancies were unexpected, especially the paradoxical behaviour of type A (also AA) vacancies:

First, the dipole moment per molecule in a PTCDA/Ag(111) layer is -0.45 D. The naive expectation of finding $+0.45$ D per missing molecule was falsified by the results: -0.09 D (A), 0.19 D (B), -0.14 D (AA), 0.39 D (BB).

Second, the surprisingly different behaviour of type A and B vacancies could be explained by a difference in their surroundings. An A (B) type vacancy is surrounded by four B (A) molecules. The O_{carb} of molecule B are less bound to the surface than those for A. Thus, the perturbation of the layer by the vacancy can be more efficiently reduced by relaxation around a type A vacancy.

Third, a reduction in the dipole moment (case type B, BB) could be understood by screening due to charge rearrangement in the surrounding molecules. However, for type A and AA vacancies, almost no dipole moment remains. And it is paradoxical that the sign is **inverted** to the expected direction! Its discussion in the previous sections is summarized below.

For type A and AA vacancies, a negative dipole moment was found, strongly indicating an

additional charge transfer compared to the layer. Both types show a similar dipole moment (per vacancy). Therefore, also a similar charge transfer from the surface to the vacancies (surrounding molecules) can be expected.

Three findings support a charged type A vacancy: First, a qualitative comparison of V^* for both vacancies revealed a stronger negative offset of the quadrupole by a dipole for A (Fig. 7.6). Thus, there is more charge transfer from the surface into the type A vacancy. Second, the vacancy shows a small resonance similar to a PTCDA core in the layer in the range of $-500\,\mathrm{mV}$ - $0\,\mathrm{mV}$ (Fig. 7.9b). Third, the LUMO of the two B-blue molecules in the surrounding of the vacancy is increased and shifted to negative V_{bias} compared to B molecules in the closed layer. Therefore, also a larger charge transfer from the surface is expected for B-blue molecules.

The behaviour of larger assemblies on surfaces is complex and can be counterintuitive. This is especially true when chemisorption plays a role, as the results presented here show. The charge distribution of molecules at the edge of a layer (this includes vacancies) is an important parameter in the formation of molecular layers. Understanding and reproduction of the findings in theoretical calculations would enhance our understanding of the growth mechanics of molecular layers.

The opposite behaviour of type A and B vacancies (as well as AA, BB and higher) could be directly used for local chemical gating or to tune the work function of a PTCDA/Ag(111) layer. Adjusting the work function of different components is important for the construction of molecular devices.

A further application would be as a memory cell or as a cellular automata (for the later see section 7.4). As the different vacancy types show a unique STS or V^* signal, the readout could be spectroscopically or electrostatically e.g. by triggering the gate of a transistor.

CHAPTER 8

Summary

This thesis paves the way for the assembly of supramolecular structures by autonomous robotic nanofabrication based on RL and their characterisation using the tools of nanoscience. In a proof of principle application the RL agent removed single molecules from a layer in which they were held together by strong molecule-surface and intermolecular interactions. The extension of the MoMaLab's capabilities to include autonomous manipulation was preceded by the understanding of the contact formation with the system (PTCDA on Ag(111)), the characterisation of the tip-molecule bond and the pioneering work of HCM.

Contact formation between the tip and PTCDA on Ag(111) was studied in section 4.2. Contact formation and the intermolecular interactions were systematically probed by performing 4096 vertical two-contact manipulations in a grid over an area covering two unit cells of the layer. By approaching one of the four O_{carb} at the corners of PTCDA with the tip a chemical bond can be formed. It was shown that there are two types of O_{carb} atoms per molecule, and four per unit cell, which differ significantly in their contact behaviour. The four different forces required for the O_{carb} atoms to switch their bonding from the surface to the tip could be extracted. Analysis of the height of the bond rupture, upon tip retraction after the initial bond formation, revealed a surprising flexibility of the four corners of PTCDA. It was shown that a lateral variation in the contact position along the C-O bond towards the centre of the molecule increases the bending of the corners and thus the height of bond rupture. These "corridors" suggest that a molecule could potentially be extracted from the layer by peeling. This peeling was indeed successfully employed by HCM and was also later rediscovered by the autonomous agent.

Next is the characterisation of the tip-molecule contact and in particular its evolution during the manipulation, presented in section 4.3. It is clear that initially there is only a single bond between the tip apex and one O_{carb} of PTCDA. PTCDA often remains in a vertical configuration on the tip after its separation from the surface, so called s-PTCDA. What is the tip-molecule contact of this configuration? To answer this question, molecules were attached to an artificial tip apex on the surface, in the form of an adatom, and their connection was probed by vertical two-contact manipulation. It has been shown that the unpaired O_{carb} next to the adatom is attracted to the surface. Therefore, the molecule orients itself during the manipulation so that the distance between the O_{carb} and the surface

is minimised. It could be concluded that in the case of s-PTCDA on the tip, a single tip-molecule bond would be unstable and that the formation of a second tip-molecule bond would be expected.

With the molecule attached to an adatom, the molecule can be manipulated into a junction with symmetrical contacts, leaving only the adatom as the surface contact and the apex atom as the tip contact. In chapter 5 it was shown that a quarter circle manipulation trajectory lead to a highly reproducible behaviour of the molecule during its manipulation into the symmetric junction. Further, the two separation events of the unpaired O_{carb} atoms from the surface and from the tip could be observed, indicating that a diagonal configuration was indeed achieved. These events were not observed when an isolated molecule (without adatom) was lifted from the surface. Taken together with the finding that contact rupture occurred closer to the surface in the case of an isolated molecule, it could be concluded that an isolated molecule does *not* reach a diagonal configuration during lifting. The molecule, attached to an adatom, was repeatedly manipulated up and down along the quarter circle with hand-controlled manipulation supported by virtual reality goggles for visual feedback. An upgraded version of HCM was used for the manipulation and was presented in section 5.2. The functionality of HCM was reimplemented in a game engine called Unity™, with focus on a modular codebase for easier maintainability and extensibility. Elements were added to provide visual feedback during the manipulation - including a sphere which severed as a visual guide during the experiment described above.

The accumulated experience gained from performing HCM and characterising the system, combined with the knowledge of the machine learning group at the TU Berlin, gave rise to autonomous robotic nanofabrication powered by RL and was presented in chapter 6. The robot learned by trial and error, much like a human, to find a peeling trajectory that would allow it to remove a molecule from the layer. The robot could only rely on its own experience to solve this task without any external support. Initially, the learning process was too slow to cope with the occasional change in the tip apex configuration, which could invalidate a previously learned peeling trajectory. The solution was to have the robot also learn a model of its environment as well. The removal task was performed with two types of robotic agents: randomly initialised (R) agents and pre-trained (P) agents. R-agents had no prior knowledge at the beginning of each removal task. An R-agent was selected as the base for all P-agents after it had found a successful peeling trajectory. Thus, P-agents started with the knowledge of having the task solved once for a particular tip. The higher performance of P-agents compared to R-agents demonstrated that some knowledge about the removal task was universal and could be transferred to new tip configurations.

In chapter 7 the capabilities of MoMaLab were used to construct a single molecule device for SQDM. SQDM was used to characterise the potential above a PTCDA/Ag(111) monolayer as well as single and double molecular vacancies. The unit cell of the layer contained two unequal PTCDA molecules, called A and B. Molecule A (B) was aligned (misaligned) with the underlying Ag lattice. The vacancies were similarly defined. An A (B) type vacancy was created by removing molecule A (B) from the layer. Vacancies of the same type (A and AA or B and BB) were shown to behave similarly. Because the molecules in the layer received a charge transfer from the surface, it was expected that the vacancies would become

positive relative to the layer. The type B vacancies fulfilled this expectation. However, it was shown that the charge transfer actually increased slightly for type A vacancies. This finding could be explained by spectroscopic analysis of the type A vacancies. The vacancy itself behaved like the backbone of a molecule, and two of the surrounding molecules showed additional charge transfer.

APPENDIX A

HandCtrl - A quick start guide

This section presents the necessary steps to quickly set up everything that is needed to start using the Unity™ version 'HandCtrl' of HCM.

The following is assumed for the HCM setup: First, the Vicon™ software (MCS) and the game engine Unity™ are running on two separate computers. Second, all the necessary software or drivers (for: RVS, ADC, VR system, game engine, MCS) are installed and everything is connected correctly. Third, the VR system is supported by the game engine.

HandCtrl is available from the GitLab server of the research centre. Version control of the source code allows all changes to HandCtrl to be tracked and all previous versions to be restored.

Setup of Vicon™ system

The first step is to start the Vicon™ software. The cameras have to be in the same LAN network as the computer running the MCS software, which should be *separated* from other networks. The cameras will be switched on automatically by the software on startup. If the cameras are not calibrated, the user finds the appropriate instructions in the manual. Now the user switches on the Vicon Apex™ (Fig. A.1) and makes sure it is sufficiently charged for the planned experiment. The Vicon Apex™ should appear as 'Apex' under 'tracked object' in the Vicon™ software. The Vicon™ software runs a VRPN server and allows third party programs to access the tracking data of the Vicon Apex™ via the name specified under tracked object, in this case 'Apex'. Note that the name given to the tracked object has to be the *same* as in the MCS script of HandCtrl (Fig. A.6b, setting 'Object Name').

The tracked space available for movement in the VR environment can be freely expanded by adding more cameras to the Vicon™ system. The area covered by modern commercial VR systems for gaming, and also their precision for tracking the experimenter's hand movement, is nowadays sufficient for HCM operation as well. When HCM was introduced in 2014 [21], only the VR goggles were available and no spatial tracking of controllers was supported. Integrating controllers from the Oculus Rift™ or the HTC Vive™, for example, would require little effort using the free SteamVR™ plugin[1] from the Unity Asset Store™.

[1]Link: https://assetstore.unity.com/packages/tools/integration/steamvr-plugin-32647 (retrieved on 29th

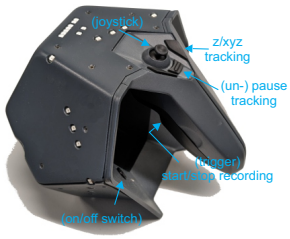

Figure A.1: Assignment of buttons on Vicon Apex™.

Setup HandCtrl

To open Unity™ on the HCM desktop computer, the user selects the HandCtrl project from the pop-up window (Fig. A.2). If it is not already listed, the user can search for the project on the hard disk using the 'OPEN' option.

Figure A.2: Screenshot - select project.

Fig. A.3 shows a screenshot of HandCtrl running in the Unity™ editor. The four windows marked by coloured rectangles are: the 'Hierarchy' window (blue), the 'Scene' window (yellow), the 'Game' window (red), and the 'Inspector' window (green).

In Unity™, everything that affects the scene (which is like a level of a game) must be a so-called 'GameObject' or part of one. The objects that belong to the 'main scene' are listed in the 'Hierarchy' window. The text colour is black (grey) for objects that are visible (hidden) in the scene. Note that the HandCtrl project also contains the scene 'testing scene' used for testing and debugging of new scripts. Make sure that the 'main scene' is loaded before starting the application for HCM experiments.

The 'Scene' window, highlighted in yellow, allows to freely observe the created 3D world (of the current scene). One can move around the world, zoom in and out, or select an object (e.g. the PTCDA molecule) and modify its position or rotation with the mouse. The object selected in 'Scene' is automatically selected in the 'Hierarchy' window (blue) and vice versa. Double-clicking on a scene object in the 'Hierarchy' window will zoom in on the selected object in the 'Scene' window.

The 'Game' window shows the view as seen by the experimenter using HCM and is highlighted in red. This is the view of the main camera placed in the scene. It can be found under [main scene] [Camera Offset] [Main Camera] in the 'Hierarchy' window. If the editor is set to 'play' a VR game, the main camera's movements will automatically match the tracked

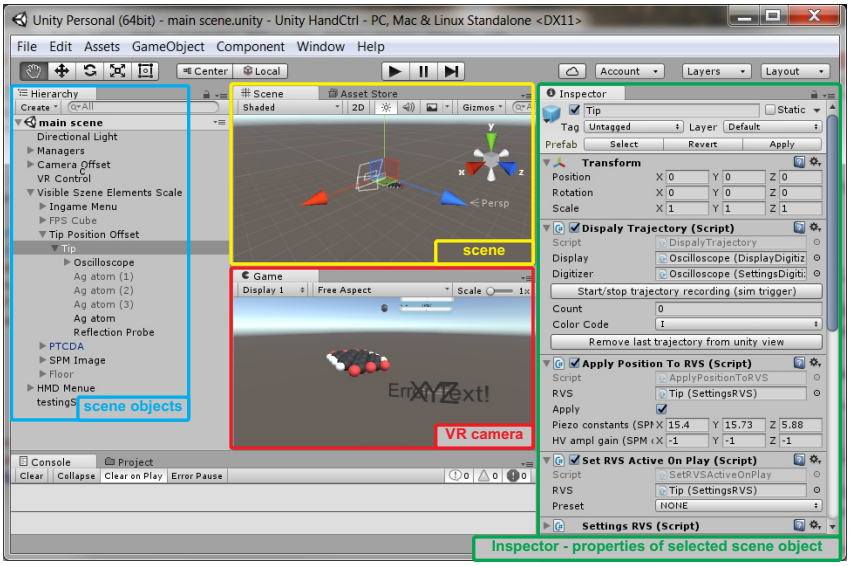

Figure A.3: Screenshot of HandCtrl in Unity™ editor. The important windows for operating HandCtrl are highlighted by coloured rectangles: Hierarchy (blue), Scene (yellow), Game (red), Inspector (green).

real-time movements of the VR goggles attached to the experimenter's head, provided by the VR setup (in our case: Oculus Rift DK2™, one camera, Oculus software). The self-written script 'Player Controller' allows the experimenter to move around in the VR world using a keyboard or controller, beyond pure head movement. It is attached to the object 'Camera Offset' ([main scene] [Camera Offset], 'Hierarchy' window).

The 'Inspector', highlighted in green, shows all attached components (custom scripts, materials, colliders, etc.) of a GameObject selected in the 'Hierarchy' window. More precisely, all public variables of a script are displayed (and can be modified) by default. A custom-optimised view can be defined in a separate script, which was done for most scripts.

For the HandCtrl application to work with VR goggles, the 'Virtual Reality Supported' option must be checked in the editor's build settings. The three steps required to set this setting are shown in Fig. A.4 and highlighted in blue.

Up to this point, all requirements for starting HandCtrl have been met. To start HandCtrl, the user presses the editor's play button (highlighted in blue in Fig. A.5). Now the 'game' (HandCtrl) is executed, and the view shown in the 'Game' window is also displayed in the VR goggles. An important feature of the Unity™ editor is that it allows also the free modification of all (public) properties of scene objects during game execution (runtime). This makes it possible to implement a graphical user interface without having to explicitly implement an 'ingame' user interface (visible in the VR environment). For example, after successfully lifting a PTCDA molecule from the PTCDA island on Ag(111), the mouse can

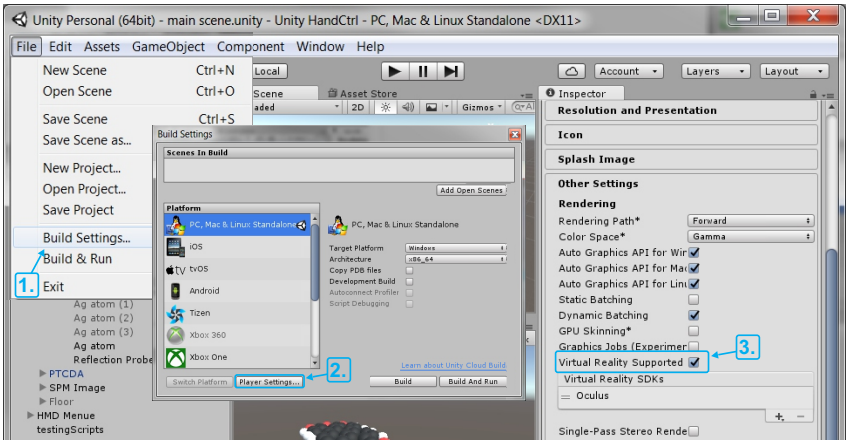

Figure A.4: Build settings for VR support (screenshot Unity™ editor).

be used to retract the SPM tip further away from the surface (also for approach, after placing the tip above a clean surface area) by clicking the appropriate buttons on the graphical user interface.

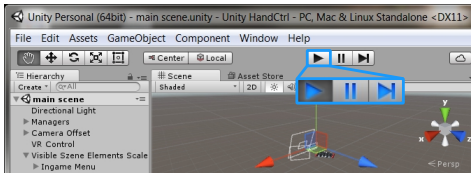

Figure A.5: Screenshot of 'Play' button (Unity™ editor). The inset shows the appearance of the player buttons during runtime.

In Fig. A.3, the most important object 'Tip' for HCM is already selected ([main scene] [Visible Scene Elements Scale] [Tip Position Offset] [Tip], 'Hierarchy' window). Fig. A.6 shows the attached scripts of 'Tip', which are sorted by: RVS (Fig. A.6a), MCS (Fig. A.6b) and other scripts (Fig. A.6c).

In the 'Settings RVS' script (Fig. A.6a), the user should specify the RVS used in the HCM setup and verify the status field to ensure a successful connection. This script is responsible for the communication with the RVS hardware and also allows to set the voltages of the RVS manually. If it is too much trouble to set the correct RVS on every 'Play' button press, the user can automate this process by specifying the used RVS in the 'Set RVS Active On Play' script above (has to be set *before* pressing 'Play'). The script 'Apply Position to RVS' converts the movement of the GameObject 'Tip' in the scene in voltages and sends them to the RVS via a (public) function of the script 'Settings RVS'. This is possible, because the

script 'Apply Position to RVS' has a reference to the specific instance of the script 'Settings RVS' that is attached to 'Tip' (indicated by the blue arrows).

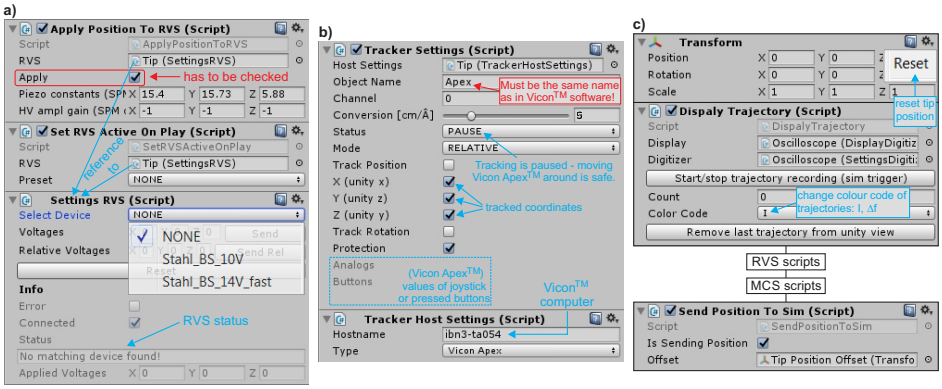

Figure A.6: Components of 'Tip' (Unity™ editor, Inspector). **a**, Scripts for remote voltage supply (RVS). In 'Settings RVS' the used RVS has to be specified. **b**, Scripts for motion capture system (MCS). **c**, Additional scripts attached to 'Tip' with their position in 'Inspector' indicated. They are useful during HCM operation.

The MCS related scripts in Fig. A.6b are: 'Tracker Host Settings' and 'Tracker Settings'. 'Tracker Host Settings' is responsible for the communication with the MCS (Vicon™) software. Note that the computer name in the property 'Hostname' corresponds to the name of the computer running the Vicon™ software on the *internal* research centre network. In this case, the Vicon™ computer has to be connected to both networks: camera network and research centre network. The HandCtrl computer must also be connected to the research centre network. The script 'Tracker Settings' is the graphical user interface for Vicon Apex™ tracking properties. On 'Play', the tracking is paused. This makes it safe to grab the Vicon Apex™ and move the arm into a comfortable position. Tracking of the xyz coordinates of the Vicon Apex™ can be enabled (disabled) separately. These settings can also be set by pressing the corresponding buttons on the Vicon Apex™ during HCM operation (Fig. A.1).

To test the connection between the Vicon™ software and HandCtrl, the connection can be verified by moving the joystick on the Vicon Apex™. Its xy-values should be displayed in the region indicated by the blue rectangle with dotted lines (Fig. A.6b). If no values appear, it should be checked that the name of the tracked object, indicated in red, matches the name of the object in the Vicon™ software. If this is already the case, it often helps to retype the name on both sides (Vicon™, HandCtrl) or to restart the Vicon™ software and (or) HandCtrl.

Fig. A.6c shows additional scripts attached to 'Tip'. They are useful during HCM operation. 'Transform' is automatically attached to every GameObject in Unity™ and controls its position, rotation and scaling. It can be used to reset the SPM tip, e.g. after removing a molecule from a vacancy. The reset removes the offset to the tip position applied by HandC-

trl and allows e.g. the lifted molecule to be placed above a clean surface area for deposition by the SPM software. The script 'Display Trajectory' allows to change the displaying of the recorded manipulation trajectories. The user can choose to display the trajectories with the colour coding for I or Δf and delete the last recorded trajectory. In case a dedicated simulation of the molecule manipulation is used, the script 'Send Position' is responsible for sending the tip position to the simulation.

Fig. A.7 shows all components of the GameObject'Oscilloscope' ([main scene] [Visible Scene Elements Scale] [Tip] [Oscilloscope], 'Hierarchy' window). It provides visual feedback of the junction during HCM in the VR environment. Namely, the real-time values of I and Δf are displayed as bar graphs in HandCtrl, as shown in the screenshot of Fig. A.7d. The 'Oscilloscope' consists of the subojects: a background, a title, two sliders for I and Δf, and their respective labels and voltage ranges (Fig. A.1a,d).

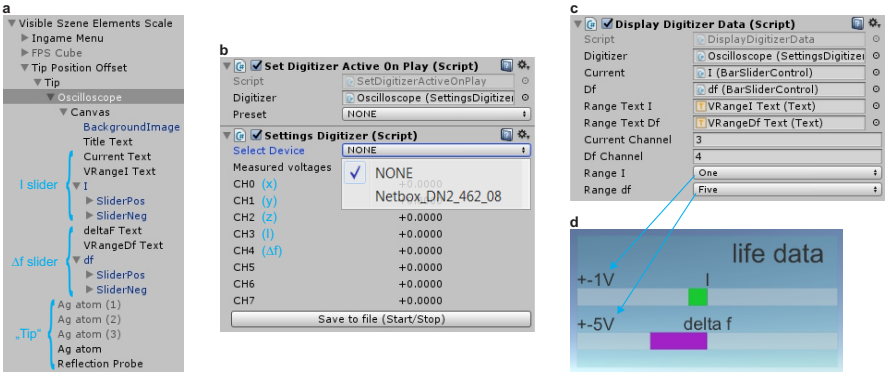

Figure A.7: Components and screenshot of real-time data panel 'Oscilloscope' (Unity™ editor). **a**, Scene objects belonging to 'Oscilloscope'. **b**, Scripts controlling the ADC unit. **c**, Script controlling which data is shown and its scaling in 'Oscilloscope'. **d**, Screenshot of 'Oscilloscope' in VR environment. Note: The name 'life data' was chosen, because the author thinks of the experimental signals as similar to the heartbeat of the molecule in the junction.

Three scripts are attached to 'Oscilloscope', namely: 'Set Digitizer Active On Play', 'Settings Digitizer', and 'Display Digitizer Data'. The first two scripts (Fig. A.1b) control the settings for digitalizing the experimental signals via the ADC. The last script (Fig. A.1c) controls how the experimental signals are displayed on the 'Oscilloscope'.

The ADC device used to record the experimental signals must be specified in 'Settings Digitizer' as indicated by the drop-down menu in Fig. A.7b. This process can be automated on 'Play', similar to the RVS setup (Fig. A.6a), by specifying the device used in the script 'Set Digitizer Active On Play' above. The script 'Settings Digitizer' is responsible for the communication with the ADC, which digitalises the analogue voltages applied to the xyz directions of the tip piezos by the RVS and the junction response (I and Δf signals). The corresponding channels of the ADC are shown in Fig. A.7b. If the connection to the ADC was successful, the correct values should appear next to the listed channels. Data recording

can be started (stopped) by pressing the button 'Save to file' at the bottom of the script. The second method is to use the trigger of the Vicon Apex™ (Fig. A.1).

The script 'Display Digitizer Data' in Fig. A.7c allows to change the displayed range for the I and Δf values during runtime on the real-time panel (Fig. A.7d). The ADC converts the analogue signals in a range from $\pm 10\,\mathrm{V}$. The selectable ranges for displaying are: $0.5\,\mathrm{V}$, $1\,\mathrm{V}$, $2\,\mathrm{V}$, $5\,\mathrm{V}$, $10\,\mathrm{V}$. The currently selected voltage range is also displayed in the VR environment, as shown in Fig. A.7d.

Now everything should be ready to start a HCM experiment. The user can perform a quick test to make sure that everything is working together correctly: The user picks up the Vicon Apex™, unpauses the tracking by pressing the corresponding button and starts to move it around while the feedback for the SPM tip is turned on. The voltages displayed on the RVS should change according to the tip movement in the VR environment. Does the feedback respond when the user moves the Vicon Apex™ up or down? Do the signals on the oscilloscope match the voltages displayed in the VR environment (real-time panel)? If everything works as expected, all necessary steps of the HCM setup have been completed successfully. Before starting with the HCM experiment, the user should pause tracking and reset the tip position, by selecting 'Tip' in the 'Hierarchy' window and clicking on 'RESET' in 'Transform' of the 'Inspector' window (Fig. A.6c). This will also automatically reset the voltages applied by the RVS.

Summary

The steps required to setup HCM are:

1. Starting MSC software
2. Opening HandCtrl in Unity™ editor
3. Verifying build settings for VR support
4. Pressing 'Play' to start application
5. Connecting to RVS
6. Verifying connection to MCS
7. Connecting to ADC
8. Validating setup by moving SPM tip via HCM (feedback enabled)
9. Resetting tip position
10. Starting HCM experiment

If the goal is to create a molecule vacancy in a PTCDA/Ag(111) layer, the steps to start HCM, after following the steps above, are as follows: The user uses the SPM software to position the tip over a O_{carb} of the target molecule. The user turns off the SPM feedback. The user reduces the bias voltage to a few mV and chooses a current amplification factor in the range of 10^5 to 10^7. The user takes the Vicon Apex™ and puts on the VR goggles. The user can use the movement keys (W, A, S, D) to position themselves in the VR environment. The user then stands up and finds a comfortable position in the room for the HCM operation. The user selects only the z direction for tracking, by pressing the corresponding buttons on the Vicon Apex™ (Fig. A.1). The selected coordinates are indicated in the head-up display of the VR environment (Fig. 5.3). The user unpauses tracking of the Vicon Apex™ by pressing

the joystick and making a descending arm movement until contact formation is observed on the real-time panel (see section 3.2.3 for characteristic signal). The user presses the trigger to start the recording of a trajectory and starts moving upwards until an Ag-O bond rupture is observed on the real-time panel. The user presses the trigger again to stop the recording of the trajectory. The user has now recorded their first HCM manipulation trajectory and created a visual anchor that will allow quick re-establishment of the Ag-O bond between the tip and the molecule. Finally, the user selects all xyz coordinates for tracking and continues the HCM experiment.

APPENDIX B

Derivation of secondary measurands of SQDM

This section derives the secondary measurands α and V^* in detail. First, eq. (7.4) is split up in the evaluation of eq. (7.2) at a reference point r_0 and any point on the sample surface. Additionally, the contribution of Φ_T is allowed to be different for $V^\pm$.

Equation (7.2) evaluated at r_0:

$$\Phi^+ = (V_0^* + V_0^+)\alpha_0 + \Phi_\mathrm{T}^+$$
$$\Phi^- = (V_0^* + V_0^-)\alpha_0 + \Phi_\mathrm{T}^-.$$

Equation (7.2) evaluated at any other point on the surface:

$$\Phi^+ = (V^* + V^+)\alpha + \Phi_\mathrm{T}^+$$
$$\Phi^- = (V^* + V^-)\alpha + \Phi_\mathrm{T}^-.$$

The relationship $\Phi^\pm(r_0) = \Phi^\pm(r)$ is valid for any point on the sample surface, because $\Phi^\pm(r) = const.$

$$(V_0^* + V_0^+)\alpha_0 + \cancel{\Phi_\mathrm{T}^+} = (V^* + V^+)\alpha + \cancel{\Phi_\mathrm{T}^+} \tag{B.1}$$
$$(V_0^* + V_0^-)\alpha_0 + \cancel{\Phi_\mathrm{T}^-} = (V^* + V^-)\alpha + \cancel{\Phi_\mathrm{T}^-} \tag{B.2}$$

Equation (7.6) results directly from solving eq. (B.2) (or eq. (B.1)) for V^* and defining $V_0^* \equiv 0$. Additionally, a relative alpha is defined as $\alpha_{rel} = \frac{\alpha}{\alpha_0}$.

$$V^* = \frac{V_0^\pm}{\alpha_{rel}} - V^\pm + \frac{V_0^*}{\alpha_{rel}} \tag{B.3}$$
$$= \frac{V_0^\pm}{\alpha_{rel}} - V^\pm \tag{B.4}$$

Equation (7.5) results by setting the equations of V^* for V^+ and V^- equal

$$\frac{V_0^+}{\alpha_{rel}} - V^+ + \cancel{\frac{V_0^*}{\alpha_{rel}}} = \frac{V_0^-}{\alpha_{rel}} - V^- + \cancel{\frac{V_0^*}{\alpha_{rel}}}$$

and then solving this equation for α_{rel}

$$\alpha_{rel} = \frac{V_0^+ - V_0^-}{V^+ - V^-}. \tag{B.5}$$

APPENDIX C

Alignment of STM topography with SQDM V*

Aligning the SQDM V^* of the PTCDA/Ag(111) monolayer with the corresponding STM topography is challenging despite the defect (PTCDA damaged by field emission) present in the recorded area (see Fig. 7.3).

Fig. C.1 shows the alignment process. The defect is not visible in the dielectric topography (Fig. 7.3d). Therefore, only the minimum in the SQDM V^* (Fig. C.1a) can be used for the alignment with the STM topography. Coloured circles mark the centre of molecule A (red) and B (yellow) in the topography (Fig. C.1b). Unfortunately, the defect does not allow an ambiguously alignment of V^* and the STM topography. Three possible cases are shown in Fig. C.1c.

A symmetric defect for alignment is preferred to the case discussed above. Fig. C.2 shows the alignment process for a double vacancy of type BB. The minimum in the dielectric topography (Fig. C.2a) marks the centre of the double vacancy and serves as reference point in the SQDM V^* (Fig. C.2b). The molecule centres are marked by coloured circles in the corresponding STM topography image (Fig. C.2b): red (A) and yellow (B). The centre of the vacancy is marked by the intersection of the two white lines along the molecule centres of A and B molecules. Fig. C.2c shows an overlay of the SQDM V^* and the positions of the molecule centres of the SQDM topography in Fig. C.2b.

From Fig. C.2c it is clear, that molecule A is on top of a positive spot and molecule B is between negative spots in the SQDM V^* (along row direction). This is in line with case three above (Fig. C.1c), where the minimum of V^* is aligned with the dark area of the damaged molecule in the STM topography recorded at $V_{\mathrm{bias}} = -0.35\,\mathrm{V}$. The alignment position is thus between the damaged B molecule and its right neighbour. Moreover, case three is self consistent in the sense that between neighbouring B molecules are minimum spots in the V^* of the PTCDA/Ag(111) monolayer. The V^* is expected to be more negative in the vicinity of $\mathrm{O_{carb}}$ atoms.

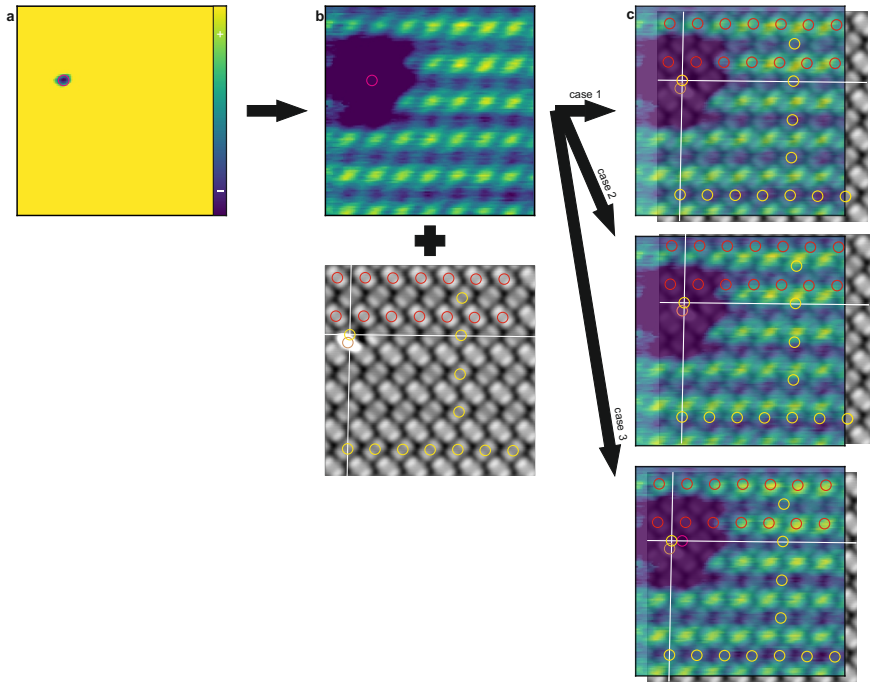

Figure C.1: Aligning STM topography and SQDM V^* on damaged molecule. The order of alignment steps is indicated by arrows. **a**, SQDM V^* (STC controller). The minimum is marked by a purple circle. **b**, SQDM V^* (same contrast range as in Fig. 7.3c) and corresponding STM topography (setpoint: $-0.35\,\mathrm{V}$, $0.2\,\mathrm{nA}$). The coloured circle in the topography mark: molecule A (red), molecule B (yellow), maximum of damaged molecule (brown). **c**, Overlay of the images in **b** showing three possible cases for the alignment. Case 1, minimum V^* over the centre of damaged molecule. Case 2, minimum V^* over maximum of damaged molecule in the topography. Case 3, minimum V^* over dark area of damaged molecule.

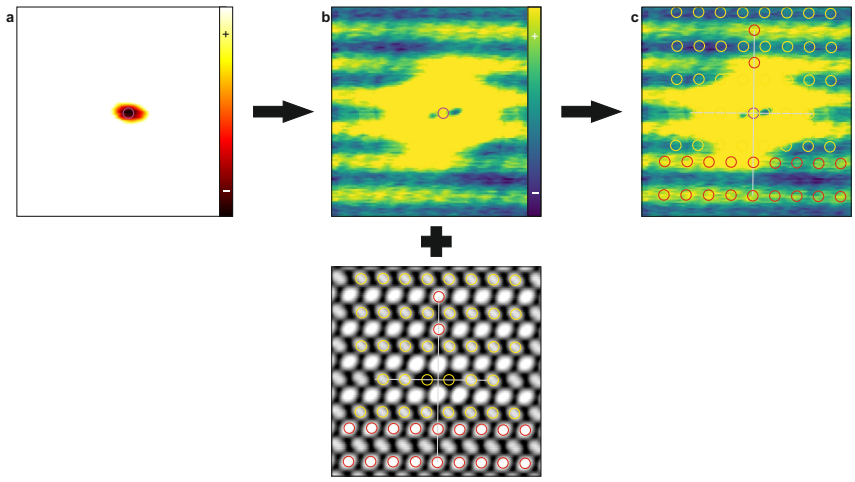

Figure C.2: Aligning STM topography and SQDM V^* on double vacancy of type BB. The order of alignment steps is indicated by arrows. **a**, Dielectric topography. The minimum is marked by a purple circle. **b**, SQDM V^* (STC controller, $z_{tip} = 27.2\,\text{Å}$) and corresponding STM topography (setpoint: 0.35 V, 0.2 nA). In the STM topography molecule positions are marked by coloured circles: red (A), yellow (B). **c**, Overlay of SQDM V^* and molecule positions of **b**. For more information see text.

List of publications

- R. Bolat, J. M. Guevara, **P. Leinen**, M. Knol, H. H. Arefi, M. Maiworm, R. Findeisen, R. Temirov, O. T. Hofmann, R. J. Maurer, F. S. Tautz, C. Wagner, "Electrostatic potentials of atomic nanostructures at metal surfaces quantified by scanning quantum dot microscopy", *Nature Communications* **15** no. 2259, (2024)
- **P. Leinen**, M. Esders, K. T. Schütt, C. Wagner, K.-R. Müller, and F. S. Tautz, "Autonomous robotic nanofabrication with reinforcement learning", *Science Advances* **6** no. 36, (2020), arXiv:2002.11952.
- C. Wagner, M. F. B. Green, M. Maiworm, **P. Leinen**, T. Esat, N. Ferri, N. Friedrich, R. Findeisen, A. Tkatchenko, R. Temirov, and F. S. Tautz, "Quantitative imaging of electric surface potentials with single-atom sensitivity", *Nature Materials* **18** no. 8, (2019) 853–859.
- R. Temirov, M. F. B. Green, N. Friedrich, **P. Leinen**, T. Esat, P. Chmielniak, S. Sarwar, J. Rawson, P. Kögerler, C. Wagner, M. Rohlfing, and F. S. Tautz, "Molecular model of a quantum dot beyond the constant interaction approximation", *Physical Review Letters* **120** no. 20, (2018) 206801.
- M. F. B. Green, C. Wagner, **P. Leinen**, T. Deilmann, P. Krüger, M. Rohlfing, F. S. Tautz, and R. Temirov, "Scanning quantum dot microscopy: A quantitative method to measure local electrostatic potential near surfaces", *Japanese Journal of Applied Physics* **55** no. 8S1, (2016) 08NA04.
- **P. Leinen**, M. F. B. Green, T. Esat, C. Wagner, F. S. Tautz, and R. Temirov, "Hand controlled manipulation of single molecules via a scanning probe microscope with a 3D virtual reality interface", *Journal of Visualized Experiments* no. 116, (2016).
- C. Wagner, M. F. B. Green, **P. Leinen**, T. Deilmann, P. Krüger, M. Rohlfing, R. Temirov, and F. S. Tautz, "Scanning quantum dot microscopy", *Physical Review Letters* **115** no. 2, (2015) 026101.
- **P. Leinen**, M. F. B. Green, T. Esat, C. Wagner, F. S. Tautz, and R. Temirov, "Virtual reality visual feedback for hand-controlled scanning probe microscopy manipulation of single molecules", *Beilstein Journal of Nanotechnology* **6** no. 1, (2015) 2148–2153.
- M. F. B. Green, T. Esat, C. Wagner, **P. Leinen**, A. Grötsch, F. S. Tautz, and R. Temirov, "Patterning a hydrogen-bonded molecular monolayer with a hand-controlled scanning probe microscope", *Beilstein Journal of Nanotechnology* **5** no. 1, (2014) 1926–1932.

Bibliography

[1] G. E. Moore, "Cramming more components onto integrated circuits," *Electronics* **38** no. 8, (1965) 114–117.

[2] C. A. Mack, "Fifty years of Moore's law," *IEEE Transactions on Semiconductor Manufacturing* **24** no. 2, (2011) 202–207.

[3] A. Aviram and M. Ratner, "Molecular rectifiers," *Chemical Physics Letters* **29** no. 2, (1974) 277.

[4] C. Joachim, J. K. Gimzewski, R. R. Schlittler, and C. Chavy, "Electronic transparence of a single C60 molecule," *Physical Review Letters* **74** no. 11, (1995) 2102–2105.

[5] N. Xin, J. Guan, C. Zhou, X. Chen, C. Gu, Y. Li, M. A. Ratner, A. Nitzan, J. F. Stoddart, and X. Guo, "Concepts in the design and engineering of single-molecule electronic devices," *Nature Reviews Physics* **1** no. 3, (2019) 211–230.

[6] M. A. Reed, "Conductance of a molecular junction," *Science* **278** no. 5336, (1997) 252–254.

[7] P. T. Mathew and F. Fang, "Advances in molecular electronics: A brief review," *Engineering* **4** no. 6, (2018) 760–771.

[8] B. Chen and K. Xu, "Single molecule-based electronic devices: A review," *Nano* **14** no. 11, (2019) 19.

[9] R. S. Bohacek, C. McMartin, and W. C. Guida, "The art and practice of structure-based drug design: A molecular modeling perspective," *Medicinal Research Reviews* **16** no. 1, (1996) 3–50.

[10] J. Welker, A. J. Weymouth, and F. J. Giessibl, "The influence of chemical bonding configuration on atomic identification by force spectroscopy," *ACS Nano* **7** no. 8, (2013) 7377–7382.

[11] N. Fournier, C. Wagner, C. Weiss, R. Temirov, and F. S. Tautz, "Force-controlled lifting of molecular wires," *Physical Review B* **84** no. 3, (2011) 035435.

[12] C. Wagner, N. Fournier, F. S. Tautz, and R. Temirov, "Measurement of the binding energies of the organic-metal perylene-teracarboxylic-dianhydride/Au(111) bonds by molecular manipulation using an atomic force microscope," *Physical Review Letters* **109** no. 7, (2012) 076102.

[13] C. Wagner, N. Fournier, V. G. Ruiz, C. Li, K. Müllen, M. Rohlfing, A. Tkatchenko, R. Temirov, and F. S. Tautz, "Non-additivity of molecule-surface van der Waals potentials from force measurements," *Nature Communications* **5** no. November, (2014) 5568.

[14] G. Langewisch, J. Falter, H. Fuchs, and A. Schirmeisen, "Forces during the controlled displacement of organic molecules," *Physical Review Letters* **110** no. 3, (2013) 036101.

[15] A. Sweetman, M. A. Rashid, S. P. Jarvis, J. L. Dunn, P. Rahe, and P. Moriarty, "Visualizing the orientational dependence of an intermolecular potential," *Nature Communications* **7** (2016) 10621.

[16] C. Toher, R. Temirov, A. Greuling, F. Pump, M. Kaczmarski, G. Cuniberti, M. Rohlfing, and F. S. Tautz, "Electrical transport through a mechanically gated molecular wire," *Physical Review B* **83** no. 15, (2011) 155402.

[17] G. Binning, H. Rohrer, C. Gerber, and E. Weibel, "Tunneling through a controllable vacuum gap," *Applied Physics Letters* **40** no. 2, (1982) 178–180.

[18] G. Binning, H. Rohrer, C. Gerber, and E. Weibel, "Surface studies by scanning tunneling microscopy," *Physical review letters* **49** no. 1, (1982) 57–61.

[19] D. M. Eigler and E. K. Schweizer, "Positioning single atoms with a scanning tunnelling microscope," *Nature* **344** no. 6266, (1990) 524–526.

[20] C. Lutz and L. Gross, "30 years of moving individual atoms," *Europhysics News* **51** no. 2, (2020) 26–28.

[21] M. F. B. Green, T. Esat, C. Wagner, P. Leinen, A. Grötsch, F. S. Tautz, and R. Temirov, "Patterning a hydrogen-bonded molecular monolayer with a hand-controlled scanning probe microscope," *Beilstein Journal of Nanotechnology* **5** no. 1, (2014) 1926–1932.

[22] B. Voigtländer, *Scanning probe microscopy. Atomic froce microscopy and scanning tunneling microscopy.* Springer-Verlag, Berlin, Heidelberg, 2015.

[23] J. Bardeen, "Tunnelling from a many-particle point of view," *Physical Review Letters* **6** no. 2, (1961) 57–59.

[24] J. Tersoff and D. R. Hamann, "Theory of the scanning tunneling microscope," *Physical Review B* **31** no. 2, (1985) 805–813.

[25] G. Binnig and C. F. Quate, "Atomic Force Microscope," *Physical Review Letters* **56** no. 9, (1986) 930–933.

[26] T. R. Albrecht, P. Grütter, D. Horne, and D. Rugar, "Frequency modulation detection using high-Q cantilevers for enhanced force microscope sensitivity," *Journal of Applied Physics* **69** no. 2, (1991) 668–673.

[27] F. J. Giessibl, "The qPlus sensor, a powerful core for the atomic force microscope," *Review of Scientific Instruments* **90** no. 1, (2019) 011101.

[28] C. Wagner, R. Temirov, and F. S. Tautz, "Perspectives of molecular manipulation and fabrication," in *Molecular Architectonics*, T. Ogawa, ed., pp. 253–319. Springer Nature, 1 ed., 2017.

[29] R. Temirov, A. Lassise, F. B. Anders, and F. S. Tautz, "Kondo effect by controlled cleavage of a single-molecule contact," *Nanotechnology* **19** no. 6, (2008) 065401.

[30] F. Tautz, "Structure and bonding of large aromatic molecules on noble metal surfaces: The example of PTCDA," *Progress in Surface Science* **82** no. 9-12, (2007) 479–520.

[31] L. Kilian, E. Umbach, and M. Sokolowski, "Molecular beam epitaxy of organic films investigated by high resolution low energy electron diffraction (SPA-LEED): 3,4,9,10-perylenetetracarboxylicacid-dianhydride (PTCDA) on Ag(111)," *Surface Science* **573** no. 3, (2004) 359–378.

[32] Y. Zou, L. Kilian, A. Schöll, T. Schmidt, R. Fink, and E. Umbach, "Chemical bonding of PTCDA on Ag surfaces and the formation of interface states," *Surface Science* **600** no. 6, (2006) 1240–1251.

[33] A. Hauschild, K. Karki, B. C. C. Cowie, M. Rohlfing, F. S. Tautz, and M. Sokolowski, "Molecular distortions and chemical bonding of a large π-conjugated molecule on a metal surface," *Physical Review Letters* **94** no. 3, (2005) 036106.

[34] L. Kilian, A. Hauschild, R. Temirov, S. Soubatch, A. Schöll, A. Bendounan, F. Reinert, T.-L. Lee, F. S. Tautz, M. Sokolowski, and E. Umbach, "Role of intermolecular interactions on the electronic and geometric structure of a large π-conjugated molecule adsorbed on a metal surface," *Physical Review Letters* **100** no. 13, (2008) 136103.

[35] A. Kraft, R. Temirov, S. K. M. Henze, S. Soubatch, M. Rohlfing, and F. S. Tautz, "Lateral adsorption geometry and site-specific electronic structure of a large organic chemisorbate on a metal surface," *Physical Review B* **74** no. 4, (2006) 041402.

[36] T. Esat, N. Friedrich, F. S. Tautz, and R. Temirov, "A standing molecule as a single-electron field emitter," *Nature* **558** no. 7711, (2018) 573–576.

[37] M. Knol, H. H. Arefi, D. Corken, J. Gardner, F. S. Tautz, R. J. Maurer, and C. Wagner, "The stabilization potential of a standing molecule," *Science Advances* **7** no. 46, (2021) 1–8.

[38] C. Wagner, M. F. B. Green, P. Leinen, T. Deilmann, P. Krüger, M. Rohlfing, R. Temirov, and F. S. Tautz, "Scanning quantum dot microscopy," *Physical Review Letters* **115** no. 2, (2015) 026101.

[39] H. H. Arefi, D. Corken, F. S. Tautz, R. J. Maurer, and C. Wagner, "Design principles for metastable standing molecules," *The Journal of Physical Chemistry C* **126** no. 15, (2022) 6880–6891.

[40] P. Leinen, M. F. B. Green, T. Esat, C. Wagner, F. S. Tautz, and R. Temirov, "Virtual reality visual feedback for hand-controlled scanning probe microscopy manipulation of single molecules," *Beilstein Journal of Nanotechnology* **6** no. 1, (2015) 2148–2153.

[41] P. Leinen, M. F. B. Green, T. Esat, C. Wagner, F. S. Tautz, and R. Temirov, "Hand controlled manipulation of single molecules via a scanning probe microscope with a 3D virtual reality interface," *Journal of Visualized Experiments* no. 116, (2016) .

[42] P. Leinen, M. Esders, K. T. Schütt, C. Wagner, K.-R. Müller, and F. S. Tautz, "Autonomous robotic nanofabrication with reinforcement learning," *Science Advances* **6** no. 36, (2020) , `arXiv:2002.11952`.

[43] O. Bauer, G. Mercurio, M. Willenbockel, W. Reckien, C. Heinrich Schmitz, B. Fiedler, S. Soubatch, T. Bredow, F. S. Tautz, and M. Sokolowski, "Role of functional groups in surface bonding of planar π-conjugated molecules," *Physical Review B* **86** no. 23, (2012) 235431.

[44] L. Kilian, E. Umbach, and M. Sokolowski, "A refined structural analysis of the PTCDA monolayer on the reconstructed Au(111) surface—"Rigid or distorted carpet?"," *Surface Science* **600** no. 13, (2006) 2633–2643.

[45] B. Stadtmüller, D. Lüftner, M. Willenbockel, E. M. Reinisch, T. Sueyoshi, G. Koller, S. Soubatch, M. G. Ramsey, P. Puschnig, F. S. Tautz, and C. Kumpf, "Unexpected interplay of bonding height and energy level alignment at heteromolecular hybrid interfaces," *Nature Communications* **5** (2014) 3685.

[46] W. Liu, F. Maaß, M. Willenbockel, C. Bronner, M. Schulze, S. Soubatch, F. S. Tautz, P. Tegeder, and A. Tkatchenko, "Quantitative prediction of molecular adsorption: Structure and binding of benzene on coinage metals," *Physical Review Letters* **115** no. 3, (2015) 036104.

[47] A. Hauschild, R. Temirov, S. Soubatch, O. Bauer, A. Schöll, B. C. C. Cowie, T.-L. Lee, F. S. Tautz, and M. Sokolowski, "Normal-incidence x-ray standing-wave determination of the adsorption geometry of PTCDA on Ag(111): Comparison of the ordered room-temperature and disordered low-temperature phases," *Physical Review B* **81** no. 12, (2010) 125432.

[48] F. Mohn, J. Repp, L. Gross, G. Meyer, M. S. Dyer, and M. Persson, "Reversible bond formation in a gold-atom-organic-molecule complex as a molecular switch.," *Physical review letters* **105** no. 26, (2010) 266102.

[49] T. Esat, T. Deilmann, B. Lechtenberg, C. Wagner, P. Krüger, R. Temirov, F. B. Anders, M. Rohlfing, and F. S. Tautz, "Transfering spin into an extended π orbital of a large molecule," *Physical Review B* **91** no. 14, (2015) 144415.

[50] B. Schuler, W. Liu, A. Tkatchenko, N. Moll, G. Meyer, A. Mistry, D. Fox, and L. Gross, "Adsorption geometry determination of single molecules by atomic force microscopy," *Physical Review Letters* **111** no. 10, (2013) 106103.

[51] M. Rohlfing, R. Temirov, and F. S. Tautz, "Adsorption structure and scanning tunneling data of a prototype organic-inorganic interface: PTCDA on Ag(111)," *Physical Review B* **76** no. 11, (2007) 115421.

[52] C. Weiss, C. Wagner, R. Temirov, and F. S. Tautz, "Direct Imaging of Intermolecular Bonds in Scanning Tunneling Microscopy," *Journal of the American Chemical Society* **132** no. 34, (2010) 11864–11865.

[53] H. Mönig, S. Amirjalayer, A. Timmer, Z. Hu, L. Liu, O. Díaz Arado, M. Cnudde, C. A. Strassert, W. Ji, M. Rohlfing, and H. Fuchs, "Quantitative assessment of intermolecular interactions by atomic force microscopy imaging using copper oxide tips," *Nature Nanotechnology* **13** no. 5, (2018) 371–375.

[54] V. G. Ruiz, C. Wagner, F. Maaß, H. H. Arefi, S. Stremlau, P. Tegeder, F. S. Tautz, and A. Tkatchenko, "Accurate quantification of the stability of the perylene-tetracarboxylic dianhydride on Au(111) molecule–surface interface," *Communications Chemistry* **6** no. 1, (2023) 136.

[55] R. Temirov, S. Soubatch, O. Neucheva, a. C. Lassise, and F. S. Tautz, "A novel method achieving ultra-high geometrical resolution in scanning tunnelling microscopy," *New Journal of Physics* **10** (2008) .

[56] L. Gross, F. Mohn, N. Moll, P. Liljeroth, and G. Meyer, "The chemical structure of a molecule resolved by atomic force microscopy," *Science* **325** no. 5944, (2009) 1110–1114.

[57] G. Kichin, C. Weiss, C. Wagner, F. S. Tautz, and R. Temirov, "Single molecule and single atom sensors for atomic resolution imaging of chemically complex surfaces," *Journal of the American Chemical Society* **133** no. 42, (2011) 16847–16851.

[58] F. Mohn, B. Schuler, L. Gross, and G. Meyer, "Different tips for high-resolution atomic force microscopy and scanning tunneling microscopy of single molecules," *Applied Physics Letters* **102** no. 7, (2013) 073109.

[59] L. Hörmann, A. Jeindl, and O. T. Hofmann, "Reproducibility of potential energy surfaces of organic/metal interfaces on the example of PTCDA on Ag(111)," *The Journal of Chemical Physics* **153** no. 10, (2020) 104701.

[60] H. Sakoe and S. Chiba, "Dynamic programming algorithm optimization for spoken word recognition," *IEEE Transactions on Acoustics, Speech, and Signal Processing* **26** no. 1, (1978) 43–49.

[61] J. Faouzi, "Time series classification: A review of algorithms and implementations," in *To appear in: Machine Learning (Emerging Trends and Applications)*. 2022.

[62] N. Fournier, *STM-based quantum transport through molecular wires*. PhD Thesis, Forschungszentrum Jülich GmbH, Zentralbibliothek, 2015.

[63] L. L. Chang, L. Esaki, and R. Tsu, "Resonant tunneling in semiconductor double barriers," *Applied Physics Letters* **24** no. 12, (1974) 593–595.

[64] B. Ricco and M. Y. Azbel, "Physics of resonant tunneling. The one-dimensional double-barrier case," *Physical Review B* **29** no. 4, (1984) 1970–1981.

[65] D. Cimbri, J. Wang, A. Al-Khalidi, and E. Wasige, "Resonant tunneling diodes high-speed terahertz wireless communications - A review," *IEEE Transactions on Terahertz Science and Technology* **12** no. 3, (2022) 226–244.

[66] G. Reecht, H. Bulou, F. Scheurer, V. Speisser, F. Mathevet, C. González, Y. J. Dappe, and G. Schull, "Pulling and stretching a molecular wire to tune its conductance," *The Journal of Physical Chemistry Letters* **6** no. 15, (2015) 2987–2992, `arXiv:1506.05653`.

[67] J. Welker, A. J. Weymouth, and F. J. Giessibl, "The influence of chemical bonding configuration on atomic identification by force spectroscopy," *ACS Nano* **7** no. 8, (2013) 7377–7382.

[68] P. Leinen, M. Esders, K. T. Schütt, C. Wagner, K.-R. Müller, and F. S. Tautz, "Autonomous robotic nanofabrication with reinforcement learning," `arXiv:2002.11952`.

[69] K. C. Neuman and A. Nagy, "Single-molecule force spectroscopy: optical tweezers, magnetic tweezers and atomic force microscopy," *Nature Methods* **5** no. 6, (2008) 491–505.

[70] R. S. Sutton and A. G. Barto, *Reinforcement learning: An introduction*. MIT press, 2nd ed., 2018.

[71] V. Mnih, K. Kavukcuoglu, D. Silver, A. A. Rusu, J. Veness, M. G. Bellemare, A. Graves, M. Riedmiller, A. K. Fidjeland, G. Ostrovski, S. Petersen, C. Beattie, A. Sadik, I. Antonoglou, H. King, D. Kumaran, D. Wierstra, S. Legg, and D. Hassabis, "Human-level control through deep reinforcement learning," *Nature* **518** no. 7540, (2015) 529–533.

[72] G. Carleo and M. Troyer, "Solving the quantum many-body problem with artificial neural networks," *Science* **355** no. 6325, (2017) 602–606.

[73] K. Seufert, W. Auwärter, F. J. García De Abajo, D. Ecija, S. Vijayaraghavan, S. Joshi, and J. V. Barth, "Controlled interaction of surface quantum-well electronic states," *Nano Letters* **13** no. 12, (2013) 6130–6135.

[74] N. Kocić, D. Blank, P. Abufager, N. Lorente, S. Decurtins, S.-X. Liu, and J. Repp, "Implementing functionality in molecular self-assembled monolayers," *Nano Letters* **19** no. 5, (2019) 2750–2757.

[75] Z. Wang, T. Schaul, M. Hessel, H. van Hasselt, M. Lanctot, and N. de Freitas, "Dueling network architectures for deep reinforcement learning," in *Proceedings of The 33rd International Conference on Machine Learning (ICML)*, pp. 1995–2003. 2016. arXiv:1511.06581.

[76] H. van Seijen, H. van Hasselt, S. Whiteson, and M. Wiering, "A theoretical and empirical analysis of Expected Sarsa," in *IEEE Symposium on Adaptive Dynamic Programming and Reinforcement Learning (ADPRL)*, pp. 177–184. IEEE, 2009.

[77] T. Schaul, J. Quan, I. Antonoglou, and D. Silver, "Prioritized experience replay," in *4th International Conference on Learning Representations (ICML)*. 2016. arXiv:1511.05952.

[78] R. S. Sutton, "Dyna, an integrated architecture for learning, planning, and reacting," *ACM SIGART Bulletin* **2** no. 4, (1991) 160–163.

[79] F. E. Kalff, M. P. Rebergen, E. Fahrenfort, J. Girovsky, R. Toskovic, J. L. Lado, J. Fernández-Rossier, and A. F. Otte, "A kilobyte rewritable atomic memory," *Nature Nanotechnology* **11** no. 11, (2016) 926–929, arXiv:1604.02265.

[80] M. Rashidi and R. A. Wolkow, "Autonomous scanning probe microscopy in situ tip conditioning through machine learning," *ACS Nano* **12** no. 6, (2018) 5185–5189, arXiv:1803.07059.

[81] O. Gordon, P. D'Hondt, L. Knijff, S. E. Freeney, F. Junqueira, P. Moriarty, and I. Swart, "Scanning tunneling state recognition with multi-class neural network ensembles," *Review of Scientific Instruments* **90** no. 10, (2019) 103704.

[82] A. Krull, P. Hirsch, C. Rother, A. Schiffrin, and C. Krull, "Artificial-intelligence-driven scanning probe microscopy," *Communications Physics* **3** no. 1, (2020) 54.

[83] H. van Hasselt, "Double Q-learning," in *Advances in Neural Information Processing Systems 23*, pp. 2613—-2621. Curran Associates, Inc., 2010.

[84] S. Thrun and A. Schwartz, "Issues in using function approximation for reinforcement learning," in *Proceedings of the 4th Connectionist Models Summer School*. Erlbaum Associates, 1993.

[85] H. van Hasselt, A. Guez, and D. Silver, "Deep reinforcement learning with double Q-learning," in *Proceedings of the Thirtieth AAAI Conference on Artificial Intelligence*, pp. 2094–2100. AAAI Press, 2016.

[86] D. P. Kingma and J. Ba, "Adam: A method for stochastic optimization," in *3rd International Conference on Learning Representations (ICLR)*. 2015. arXiv:1412.6980.

[87] M. F. B. Green, C. Wagner, P. Leinen, T. Deilmann, P. Krüger, M. Rohlfing, F. S. Tautz, and R. Temirov, "Scanning quantum dot microscopy: A quantitative method to measure local electrostatic potential near surfaces," *Japanese Journal of Applied Physics* **55** no. 8S1, (2016) 08NA04.

[88] R. Temirov, M. F. B. Green, N. Friedrich, P. Leinen, T. Esat, P. Chmielniak, S. Sarwar, J. Rawson, P. Kögerler, C. Wagner, M. Rohlfing, and F. S. Tautz, "Molecular model of a quantum dot beyond the constant interaction approximation," *Physical Review Letters* **120** no. 20, (2018) 206801.

[89] C. Wagner, M. F. B. Green, M. Maiworm, P. Leinen, T. Esat, N. Ferri, N. Friedrich, R. Findeisen, A. Tkatchenko, R. Temirov, and F. S. Tautz, "Quantitative imaging of electric surface potentials with single-atom sensitivity," *Nature Materials* **18** no. 8, (2019) 853–859.

[90] C. Wagner and F. S. Tautz, "The theory of scanning quantum dot microscopy," *Journal of Physics: Condensed Matter* **31** no. 47, (2019) 475901, `arXiv:1905.06153`.

Band / Volume 110
Mechanics of deep neural networks beyond the Gaussian limit
K. Fischer (2025), xvi, 138 pp
ISBN: 978-3-95806-815-5

Band / Volume 111
Characteristics of plastically deformed *fcc* and *bcc* High-Entropy Alloys
T. Meenen (2025), x, 115 pp
ISBN: 978-3-95806-820-9

Band / Volume 112
Software-Configurable Analog-To-Digital Converters for Configurable Pulse Detection
L. Krystofiak (2025), xvii, 113 pp, xxix
ISBN: 978-3-95806-826-1

Band / Volume 113
Development of Superparamagnetic Based Biological Sensor for the Detection of Brucella DNA Using Frequency Mixing Magnetic Detection
A. Abuawad (2025), X, 129 pp
ISBN: 978-3-95806-836-0

Band / Volume 114
A System for the Cryogenic Power Management of Quantum Computing Electronics: Development, Integration, and Test
A. R. Cabrera Galicia (2025), xxv, 110, lviii pp
ISBN: 978-3-95806-844-5

Band / Volume 115
Investigation of 2D Materials using Low Energy Electron Microscopy (LEEM)
H. Yin (2025) viii, 137 pp
ISBN: 978-3-95806-848-3

Band / Volume 116
Topotactic phase transition in $La_{0.6}Sr_{0.4}CoO_{3-\delta}$ thin films: oxygen content, dynamics and reversibility
S. He (2025) ix, 137 pp
ISBN: 978-3-95806-868-1

Band / Volume 117
Electrical anisotropy and shear-resistant topology in the quasi one-dimensional van-der-Waals material α-Bi_4Br_4
J.K. Hofmann (2025) xv, 129 pp
ISBN: 978-3-95806-869-8

Band / Volume 118
Spin-orbital mixing in the topological ladder of the two-dimensional metal $PtTe_2$
M. Qahosh (2025), ix, 170 pp
ISBN: 978-3-95806-872-8

Band / Volume 119
Functions of SNNs constrained by biology
A. Korcsak-Gorzo (2025), xvi, 145 pp
ISBN: 978-3-95806-876-6

Band / Volume 120
On Scalable Integrated Charge State Tuning for Semiconductor Quantum Dot Devices
F. A. Hader (2026), xx, 145 pp
ISBN: 978-3-95806-884-1

Band / Volume 121
Efficient Massively Space-Time-Parallel Simulations with Adaptive Spectral Deferred Correction
T. Saupe (2026), v, 149 pp
ISBN: 978-3-95806-886-5

Band / Volume 122
Controlled single-molecule manipulation
P. Kopp (2026), viii, 136 pp
ISBN: 978-3-95806-887-2

Information
Band / Volume 122
ISBN 978-3-95806-887-2

Mitglied der Helmholtz-Gemeinschaft

JÜLICH
Forschungszentrum